TECHNISCHE
UNIVERSITÄT
MÜNCHEN

WALTHER-
MEIßNER-
INSTITUT

BAYERISCHE
AKADEMIE DER
WISSENSCHAFTEN

Microwave Quantum Teleportation Over a Thermal Channel

Master's Thesis

Wun Kwan Yam

Supervisor: Prof. Dr. Rudolf Gross
Advisor: Dr. Kirill G. Fedorov

Garching – 12 October 2022

Contents

Chapter 1

Introduction

Over the last century, quantum mechanics has led to various developments in fundamental physical theory and generated numerous technological advances. In particular, the field of quantum information has grown rapidly in the last decades. This includes developments in various topics such as quantum computing [1], quantum communication [2, 3], quantum sensing [4, 5], and quantum simulation [6]. In the field of quantum information, fundamental quantum properties such as superposition and entanglement are exploited to achieve quantum advantages over classical systems. Quantum information science can then lead to improvements in the efficiency, security, precision, and computing power of various technologies.

Many physical platforms are used to realize concepts in quantum information science. Among these platforms, superconducting circuits is especially promising due to its strong interaction strengths and tunability [7–9]. A central component of superconducting circuits is the Josephson junction, which functions as a nonlinear, tunable, and lossless inductance. This component allows superconducting circuits to be built into artificial atoms in the gigahertz regime and be used to implement qubits. One of the most exciting present developments in quantum information is the construction of quantum computers based on superconducting circuits [10]. In order to scale up these quantum computers, multiple quantum processors should be connected in a quantum network. This requires efficient communication between superconducting circuits and thus motivates the study of quantum communication in the microwave frequency regime.

Quantum communication exploits non-classical correlations to achieve efficient and unconditionally secure exchange of information. It can be implemented with continuous-variable (CV) systems, which are described by a continuous spectrum of eigenvalues [11, 12]. In the microwave regime, one promising approach to quantum communication is by using propagating quantum microwaves, which are described by the quadratures of their propagating electromagnetic field [12]. This is because the frequency of propagating quantum signals can easily match that of superconducting processors, without large conversion inefficiencies [13]. Furthermore, most modern communication and computation tasks operate in the microwave regime, so propagating quantum microwaves can interface well with current infrastructure,

Quantum teleportation, which uses quantum entanglement and classical communication, is an outstanding quantum communication protocol that allows for secure transfer of unknown quantum states without directly sending them. Analog quantum teleportation with propagating quantum microwaves has already been experimentally demonstrated in a laboratory setting at the Walther-Meißner-Institute [14]. We extend this experimental result by implementing microwave quantum teleportation between two spatially-separated dilution refrigerators. The two dilution refrigerators are connected by a custom-made cryogenic link that can maintain superconducting temperatures. This setup imitates a realistic scenario of quantum communication between two spatially separated quantum computers. Implementing spatially-separated microwave quantum teleportation can also have applications for interfaces between various quantum devices. In our experiments, we extensively use the Josephson parametric amplifier (JPA), which is a superconducting circuit that functions as a nonlinear, tunable resonator [15–17]. JPAs can be used to generate squeezed states, where noise in one quadrature is reduced below the vacuum level and the noise in the orthogonal quadrature is amplified proportionally. Orthogonally squeezed states can be superimposed to generate a two-mode squeezed (TMS) state that carries entanglement [11]. We employ TMS states as the entangled resource to accomplish our CV quantum teleportation protocol in the microwave regime. In order to characterize the performance of our quantum teleportation procedure, we calculate the fidelity, which measures the overlap between the initial state and the teleported state. The fidelity allows us to determine whether we obtain a quantum advantage and whether the communication is unconditionally secure [12].

In our work, we study microwave quantum teleportation from a practical point of view, where we investigate how realistic imperfections affect the performance of the protocol. Such imperfections include the availability of a finite experimental codebook of teleported states as well as the effect of realistic losses and noise. The 1 dB compression point of a JPA limits the maximum input power that the JPA can amplify [18], which constrains the state displacements that can be teleported. We then analyze the influence of a finite codebook on the communication security of quantum teleportation. Due to the low photon energy of microwave photons in the gigahertz regime, microwave quantum teleportation requires cryogenic temperatures of tens of millikelvin to avoid excessive ambient thermal noise. However, in realistic application scenarios, the classical signal can be susceptible to significant losses and environmental noise. Thus, we systematically investigate the performance of microwave quantum teleportation under realistic conditions and especially focus on the resilience towards induced thermal noise.

First, we introduce the truncated Gaussian codebook as a realistic set of input states and derive the corresponding no-cloning limit for the teleportation fidelity. In the next step, we consider the scenario of microwave quantum teleportation over a thermal noise channel. In particular, we investigate the effect of environmental thermal noise photons, coupled to the analog feedforward, as well as to the entanglement distribution channel.

We perform a simulation of analog microwave quantum teleportation which takes all realistic loss and noise contributions into account and analyze under which conditions we reach fidelities beyond the no-cloning threshold. Furthermore, we analyze the temperature dependence of the maximally achievable communication bit rate. We thereby show that the performance of the protocol is asymptotically robust against feedforward losses and noise and find that the relevant experimental constraint is given by the finite coupling of the feedforward signal to the receiving communication party. Our study reveals that by making this coupling sufficiently small, we can achieve unconditionally secure quantum microwave teleportation for the case where the feedforward is transmitted as an analog microwave signal at room temperature. We thereby demonstrate that analog Gaussian quantum teleportation realizes an error-correction scheme for losses and noise in the feedforward channel.

The thesis is structured as follows. In Chapter 2, we present the theory for propagating quantum microwaves and introduce relevant Gaussian states. We also describe the Josephson parametric amplifier and the mechanism for generating squeezing. In Chapter 3, we present the theory for analog continuous-variable quantum teleportation. We also analyze the effects of a finite-energy codebook and thermal channels on the performance of quantum teleportation. In Chapter 4, we describe the experimental setup and measurement techniques used in our experiment. In Chapter 5, we describe our microwave quantum cryogenic link and its assembly procedure. We also present measurement results for entanglement distribution over the cryogenic link. In Chapter 6, we present measurement results for microwave quantum teleportation over the cryogenic link. We also discuss implementations for microwave quantum teleportation over a room temperature feedforward channel. In Chapter 7, we give a summary of the thesis and provide an outlook.

Chapter 2

Theory

In this chapter, we introduce the theoretical concepts relevant to our work. In Section 2.1, we discuss propagating quantum microwaves and continuous-variable quantum information. We describe the quantum mechanical representation of quantum microwaves and present important classes of Gaussian states. In Section 2.2, we discuss the Josephson effects and introduce the Josephson parametric amplifier. We describe the theory of Josephson junctions and present the direct current superconducting quantum interference device (DC-SQUID).

2.1 Propagating quantum microwaves

For our work, we use propagating quantum microwaves that are Gaussian quantum states [11]. In this section, we introduce the theory to understand and utilize propagating quantum microwaves. We give a theoretical description of quantum microwaves and explain different Gaussian states. We introduce the concept of continuous-variable quantum information, in particular with respect to quantum communication.

2.1.1 Representation of quantum microwaves

In this work, we investigate electromagnetic fields with frequency 5-6 GHz that propagate along coaxial cables or coplanar waveguides. These signals $A(r,t)$ can be classically described by their in-phase quadrature component $I(t)$ and out-of-phase quadrature component $Q(t)$, according to

$$A(r,t) = I(t)\cos(\omega t - kr) + Q(t)\sin(\omega t - kr), \tag{2.1}$$

where $f = \omega/2\pi$ is the frequency, k is the wave vector, r is the position, and t is the time. Given the frequency f and wave vector k, the quadrature components allow us to fully describe the propagating signal. Propagating electromagnetic fields can be decomposed into orthogonal modes, which describe the field patterns corresponding to different eigenfunctions of the electromagnetic field equation at a given frequency. In

the next step, we quantize the electromagnetic field in the framework of the second quantization. The amplitude operator for the quantized single-mode electric field is written as [19]

$$\hat{A}(r,t) = C\left[\hat{a}e^{i(\omega t-kr)} + \hat{a}^{\dagger}e^{-i(\omega t-kr)}\right] = 2C\left[\hat{q}\cos(\omega t - kr) + \hat{p}\sin(\omega t - kr)\right], \tag{2.2}$$

where C is a normalization constant, chosen such that the annihilation and creation operators of the field, $\hat{a}$ and $\hat{a}^{\dagger}$, obey the bosonic commutation relation $[\hat{a}, \hat{a}^{\dagger}] = 1$ and define the photon number operator $\langle\hat{n}\rangle \equiv \hat{a}^{\dagger}\hat{a}$. These operators are related to the quadrature operators by

$$\hat{q} = \frac{\hat{a} + \hat{a}^{\dagger}}{2}, \quad \hat{p} = \frac{\hat{a} - \hat{a}^{\dagger}}{2i}. \tag{2.3}$$

The quadrature operators obey the commutation relation $[\hat{q}, \hat{p}] = i/2$ and their eigenvalues correspond to the classical quadratures $I(t)$ and $Q(t)$. Since the quadrature operators do not commute, they satisfy the Heisenberg uncertainty relation [20]

$$\Delta q \Delta p \geq \frac{1}{4}, \tag{2.4}$$

where standard deviation ΔO of the observable $\hat{O}$ is defined as $(\Delta O)^2 \equiv \langle O^2\rangle - \langle O\rangle^2$. Eq. 2.4 implies that $\hat{q}$ and $\hat{p}$ cannot be simultaneously measured with absolute accuracy, which means that the quantum state can only be described in a probabilistic manner. Thus, we introduce quantum mechanical representations for propagating quantum microwaves.

Density matrix

One general method to describe quantum systems is by using the density matrix formalism. The density matrix can be expressed as

$$\hat{\rho} = \sum_{i}^{N} p_{i=1} \left|\psi_i\right\rangle \left\langle\psi_i\right|, \tag{2.5}$$

where p_i is the classical probability to find the system in eigenstate $|\psi_i\rangle$ and N is the Hilbert-space dimension. Pure states satisfy $\mathrm{tr}(\hat{\rho}^2) = 1$, while mixed states satisfy $\mathrm{tr}(\hat{\rho}^2) < 1$. The expectation value of an observable $\hat{O}$ is found by $\langle\hat{O}\rangle = \mathrm{tr}(\hat{O}\hat{\rho})$. Furthermore, $\hat{\rho}$ is normalization as $\mathrm{tr}(\hat{\rho}) = 1$. We can determine the closeness of two quantum states $\hat{\rho}_1$ and $\hat{\rho}_2$ using the fidelity

$$F(\hat{\rho}_1, \hat{\rho}_2) = \left(\mathrm{tr}\sqrt{\sqrt{\hat{\rho}_1}\hat{\rho}_2\sqrt{\hat{\rho}_1}}\right)^2. \tag{2.6}$$

The states coincide if $F(\hat{\rho}_1, \hat{\rho}_2) = 1$ and the states are orthogonal if $F(\hat{\rho}_1, \hat{\rho}_2) = 0$.

The density operator contains all information about a quantum state and are practical for the description of finite-dimensional quantum systems. However, in the case of propagating

quantum microwaves, which are described by a continuous spectrum of eigenvalues, the exact treatment in terms of density operators becomes tedious since the Hilbert-space dimension is infinity. A more practical description of such a continuous-variable system is possible in terms of phase-space quasiprobability distributions such as the Wigner function, which we introduce in the next section.

Wigner function

Wigner functions was proposed by Eugene Wigner [21] to relate density matrices to phase space functions. In a classical description, a probability distribution can be assigned to each quadrature in phase space. Since the Heisenberg uncertainty prohibits simultaneous knowledge about both quadratures, a quasiprobability distribution is needed to describe the measurement outcomes of a quantum system in an ensemble. One conventionally used quasiprobability distribution for continuous variable states is the Wigner function [21, 22]

$$W(q,p) = \frac{1}{\pi\hbar}\int \langle q-y|\hat{\rho}|q+y\rangle\, e^{2ipy/\hbar}dy, \tag{2.7}$$

which corresponds to a density matrix $\hat{\rho}$. The Wigner function satisfies the normalization condition $\iint W(q,p)dqdp = 1$. The observable probability distribution of a certain quadrature is computed by integrating the Wigner function over the other quadratures, which gives the marginal distribution

$$w(q) = \int_{-\infty}^{\infty} W(q,p)dp = \langle q|\hat{\rho}|q\rangle\,, \tag{2.8}$$

$$w(p) = \int_{-\infty}^{\infty} W(q,p)dq = \langle p|\hat{\rho}|p\rangle\,. \tag{2.9}$$

This marginal distribution corresponds to the projective phase-space measurement of the selected quadrature. Gaussian states have Wigner functions that are normalized Gaussian distributions, which allows a practical representation of Gaussian states while preserving its quantum properties. The Wigner function for single-mode Gaussian states can be expressed as

$$\begin{aligned} W(q,p) = &\frac{1}{\pi\sqrt{(\nu+1/2)^2-|\mu|^2}} \\ &\times \exp\left[-\frac{(\nu+1/2)|\zeta-\langle\hat{a}\rangle|^2-(\mu^*/2)(\zeta-\langle\hat{a}\rangle)^2-(\mu/2)(\zeta^*-\langle\hat{a}^\dagger\rangle)^2}{(\nu+1/2)^2-|\mu|^2}\right], \end{aligned} \tag{2.10}$$

where $\zeta = q+ip$, $\mu = \langle\hat{a}^2\rangle - \langle\hat{a}\rangle^2$, and $\nu = \langle\hat{a}^\dagger\hat{a}\rangle - |\langle\hat{a}\rangle|^2$.

Statistical moments

Another representation of propagating quantum microwaves is through the statistical moments of quadratures. Statistical moments $\langle(\hat{a}^\dagger)^m \hat{a}^n\rangle$ with $m, n \in \mathbb{N}_0$ contain the same information as density matrices and fully define a quantum state [23]. Since statistical moments can be directly detected, this representation is used extensively in this work to calculate the properties of our states. We consider a N-mode Gaussian state. The first-order statistical moment is the mean

$$\hat{\mathbf{r}} = \langle \mathbf{r} \rangle \,, \tag{2.11}$$

where $\mathbf{r} = (q_1, p_1, \ldots, q_N, p_N)$ is a vector containing all quadratures of the N modes. The second-order statistical moment defines the $2N \times 2N$ covariance matrix $\mathbf{V}$ with elements

$$V_{ij} = \frac{\langle \hat{r}_i \hat{r}_j + \hat{r}_j \hat{r}_i \rangle}{2} - \langle \hat{r}_i \rangle \langle \hat{r}_j \rangle \,. \tag{2.12}$$

Gaussian states are fully defined by statistical moments up to the second order $m + n \leq 2$ [24, 25], and thus by $\bar{\mathbf{r}}$ and $\mathbf{V}$. In general, the Wigner function for a N-mode Gaussian state is written as [12]

$$W(\mathbf{r}) = \frac{\exp\left[-\frac{1}{2}(\mathbf{r} - \bar{\mathbf{r}})\mathbf{V}^{-1}(\mathbf{r} - \bar{\mathbf{r}})^T\right]}{(2\pi)^N \sqrt{\det \mathbf{V}}}. \tag{2.13}$$

Furthermore, the purity of a Gaussian state is given by [26, 27]

$$\mu = \frac{1}{4^N \sqrt{\det \mathbf{V}}}. \tag{2.14}$$

Hence, a Gaussian state is pure when the covariance matrix satisfies $\det \mathbf{V} = (1/4)^{2N}$ and therefore saturates the Heisenberg uncertainty relation.

For two-mode Gaussian states, the covariance matrix can be written as

$$\mathbf{V} = \begin{pmatrix} \mathbf{A} & \mathbf{C} \\ \mathbf{C}^T & \mathbf{B} \end{pmatrix}, \tag{2.15}$$

where $\mathbf{A}$, $\mathbf{B}$, and $\mathbf{C}$ are 2×2 matrices that describe the local state A in the first mode, the local state B in the second mode, and the correlations between the modes, respectively. We can define the symplectic invariants of the covariance matrix [26]

$$I_1 = \det \mathbf{A}, \quad I_2 = \det \mathbf{B}, \quad I_3 = \det \mathbf{C}, \quad I_4 = \det \mathbf{V}, \tag{2.16}$$

which are invariant under local unitary Gaussian transformations. We can then define the

two symplectic eigenvalues of the bipartite Gaussian state

$$\nu_{\pm} = \sqrt{\frac{\Delta \pm \sqrt{\Delta^2 - 4I_4}}{2}}, \tag{2.17}$$

where $\Delta = I_1 + I_2 + 2I_3$. The symplectic eigenvalues are used in this work to calculate various measures of the bipartite state. For instance, the Heisenberg uncertainty can be written as [28]

$$\nu_{-} \geq \frac{1}{4}, \tag{2.18}$$

which allows us to check if an experimentally reconstructed Gaussian state is physical.

2.1.2 Relevant Gaussian states

Gaussian states are of high relevance since many fundamental quantum states fall into this category. In this section, we present the fundamental Gaussian states and their properties. In particular, we introduce the thermal state, the coherent (or displaced) state, and the squeezed state. Any Gaussian state can be constructed as a combination of these fundamental states. We also introduce the two-mode squeezed state, which we use as an entangled resource state in our quantum communication experiments.

Vacuum and thermal state

Even at the lowest possible energy state, fluctuations in the electromagnetic field exist due to the bosonic commutation relation. This lowest energy state is called the vacuum state $|0\rangle$ and emergs from the Heisenberg uncertainty relation in both quadratures $(\Delta q)^2 = (\Delta p)^2 = 1/4$. Since the vacuum state is the lowest possible energy state, it is assigned a temperature $T = 0$. While it is impossible to realize $T = 0$ in experiment, we can approximate low energy states as vacuum states if $k_{\mathrm{B}}T \ll hf$ is fulfilled. This approximation is valid for our experimental frequencies of 5-6 GHz and temperatures around 50 mK.

For a finite temperature $T > 0$, the mean photon number at a frequency mode f follows the Bose-Einstein statistics [29]

$$n_{\mathrm{th}} \equiv \mathrm{tr}(\hat{a}^{\dagger}\hat{a}\hat{\rho}_{\mathrm{th}}) = \frac{1}{\exp\left(\frac{hf}{k_{\mathrm{B}}T}\right) - 1}, \tag{2.19}$$

where k_{B} is the Boltzmann constant and h is the Planck constant. The density matrix of a thermal state is given by [20]

$$\hat{\rho}_{\mathrm{th}} = \sum_n \frac{\langle \hat{n} \rangle^n}{(1 + \langle \hat{n} \rangle)^{n+1}} |n\rangle \langle n| , \tag{2.20}$$

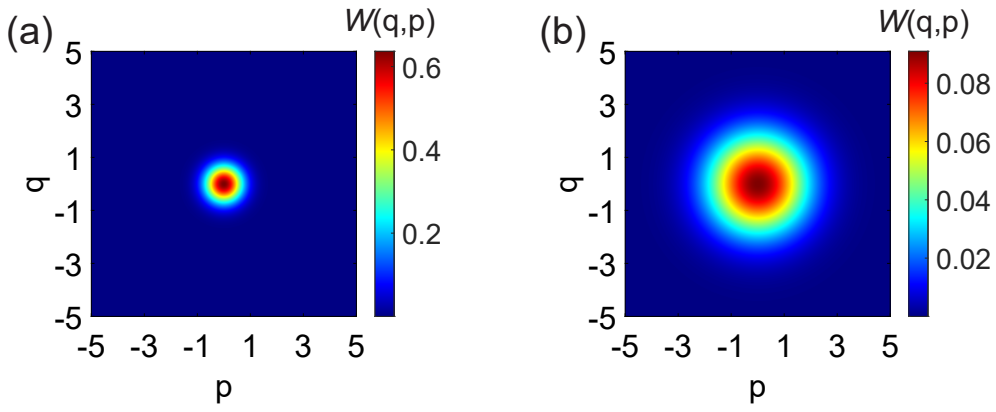

Figure 2.1: (a) Wigner function of a vacuum state. (b) Wigner function of a thermal state with $n_{\mathrm{th}} = 3$.

where $\langle \hat{n} \rangle = \langle \hat{a}^\dagger \hat{a} \rangle = n_{\mathrm{th}}$ is the mean photon number. The mean and covariance matrix of a single-mode thermal state is given by

$$\bar{\mathbf{r}}_{\mathrm{th}} = \mathbf{0} \tag{2.21}$$

$$\mathbf{V}_{\mathrm{th}} = (1 + 2n_{\mathrm{th}})\frac{\mathbb{I}_2}{4}, \tag{2.22}$$

where $\mathbb{I}_2$ is the 2×2 identity matrix. Fig. 2.1 shows the Wigner functions of the vacuum state where $n_{\mathrm{th}} = 0$ and a thermal state with $n_{\mathrm{th}} = 3$.

Coherent state

Coherent states $|\alpha\rangle$, also called displaced states, are defined as eigenstates of the annihilation operator $\hat{a}\,|\alpha\rangle = \alpha\,|\alpha\rangle$. They can be formally described by displacing the vacuum state in phase space $|\alpha\rangle = \hat{D}(\alpha)\,|0\rangle$ using the displacement operator

$$\hat{D}(\alpha) = \exp\left(\alpha\hat{a}^\dagger - \alpha^*\hat{a}\right), \tag{2.23}$$

where $\alpha = |\alpha|e^{i(\pi/2-\theta)} = Q + iP$ is the complex displacement amplitude. The displacement angle θ is defined as the angle between the displacement direction and the p-axis. Fig. 2.2 shows the Wigner function of a coherent state. The mean and covariance matrix of a single-mode coherent state is given by

$$\bar{\mathbf{r}}_{\mathrm{coh}} = (Q, P) = (\mathrm{Re}(\alpha), \mathrm{Im}(\alpha)) \tag{2.24}$$

$$\mathbf{V}_{\mathrm{coh}} = \frac{\mathbb{I}_2}{4}. \tag{2.25}$$

We see that the displacement operator shifts the maximum of the Wigner function to (Q, P) and that coherent states also saturate the Heisenberg uncertainty relation.

We implement the displacement operator in our experiments using a directional coupler,

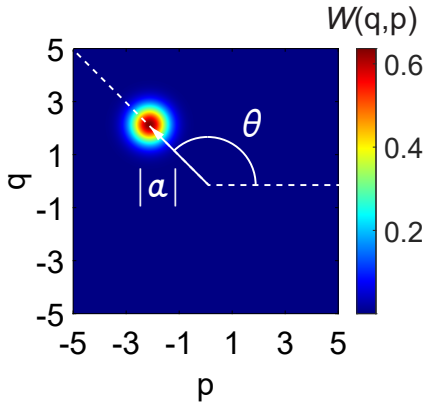

Figure 2.2: Wigner function of a coherent state with $|\alpha| = 3$ and $\theta = 3\pi/4$.

which functions as a highly asymmetric beam splitter [30]. An input state $\hat{a}_{\text{in}}$ is sent to the port with high transmissivity τ and a strong coherent signal $\hat{a}_{\text{coh}}$ is sent to the weakly coupled port. Then, the output signal $\hat{a}_{\text{out}}$ becomes [31]

$$\hat{a}_{\text{out}} = \sqrt{\tau}\hat{a}_{\text{in}} + \sqrt{1-\tau}\hat{a}_{\text{coh}}. \tag{2.26}$$

In the limit of $\tau \to 1$ and $|\alpha_{\text{coh}}| \gg 1$, such that $\sqrt{1-\tau}\alpha_{\text{coh}} = \alpha$, we have the form

$$\hat{a}_{\text{out}} \approx \hat{a}_{\text{in}} + \sqrt{1-\tau}\alpha_{\text{coh}}\hat{I} = \hat{a}_{\text{in}} + \alpha\hat{I}, \tag{2.27}$$

where $\hat{I}$ is the identity operator. This implements a displacement by $\hat{D}(\alpha)$.

Squeezed state

Squeezed states $|\xi\rangle$ are described by squeezing the vacuum state $|\xi\rangle = \hat{S}(\xi)\,|0\rangle$ using the squeezing operator

$$\hat{S}(\xi) = \exp\left(\frac{1}{2}\xi^*\hat{a}^2 - \frac{1}{2}\xi(\hat{a}^\dagger)^2\right), \tag{2.28}$$

where $\xi = re^{i\varphi}$ is the complex squeezing amplitude, r is the squeezing factor, and φ is the squeezing angle. We define $\gamma \equiv -\varphi/2$ as the angle between the antisqueezed quadrature direction and the p-axis. Fig. 2.3 shows the Wigner function of a squeezed state. The mean and covariance matrix of a single-mode squeezed state is given by

$$\bar{\mathbf{r}}_{\text{sq}} = \mathbf{0} \tag{2.29}$$

$$\mathbf{V}_{\text{sq}} = \frac{1}{4}\begin{pmatrix} e^{-2r}\cos^2\frac{\varphi}{2} + e^{2r}\sin^2\frac{\varphi}{2} & -\sinh 2r\sin\varphi \\ -\sinh 2r\sin\varphi & e^{2r}\cos^2\frac{\varphi}{2} + e^{-2r}\sin^2\frac{\varphi}{2} \end{pmatrix}. \tag{2.30}$$

The squeezing factor r determines the amount of squeezing, which is characterized by the squeezed variance $\sigma_{\text{s}}^2 = e^{-2r}/4$ and the antisqueezed variance $\sigma_{\text{a}}^2 = e^{2r}/4$. Conventionally,

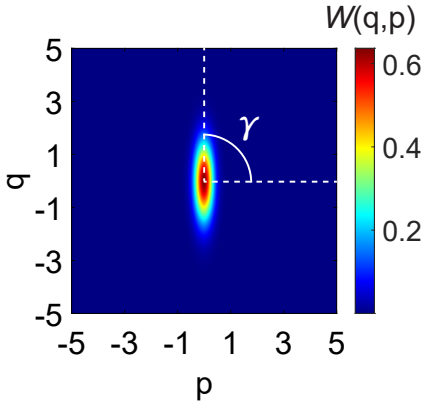

Figure 2.3: Wigner function of a squeezed state with $\gamma = \pi/2$ and $r = 0.7$, corresponding to a squeezing level of $S = 6.1$ dB.

we quantify the squeezing level S and antisqueezing level A in decibels as

$$S = -10 \log_{10} \left(\frac{\sigma_{\mathrm{s}}^2}{0.25} \right), \tag{2.31}$$

$$A = -10 \log_{10} \left(\frac{\sigma_{\mathrm{a}}^2}{0.25} \right), \tag{2.32}$$

where 0.25 is the quadrature variance of the vacuum. After applying the squeezing operator, we see that the fluctuations in the squeezed quadrature are suppressed below the vacuum limit. The orthogonal quadrature is simultaneously amplified in accordance with the Heisenberg uncertainty relation. Positive levels of S imply squeezing below the vacuum level, and we get $S = 20r \log_{10}(e)$ for a pure squeezed state. In our experiment, we generate squeezed states with Josephson parametric amplifiers, which is further explained in Section 2.2.4.

Two-mode squeezed state

Two-mode squeezed (TMS) states form an entangled quantum resource. TMS states are described by the two-mode squeezing operator [19]

$$\hat{S}_{1,2}(\xi) = \exp\left(\xi^* \hat{a}_1 \hat{a}_2 - \xi \hat{a}_1^\dagger \hat{a}_2^\dagger \right), \tag{2.33}$$

where $\hat{a}_i$ is the annihilation operator of the i-th mode and $\xi = re^{i\varphi}$ is the complex squeezing amplitude. The parameter r determines the amount of two-mode squeezing and the phase φ determines the correlated quadratures. The mean and covariance matrix of a

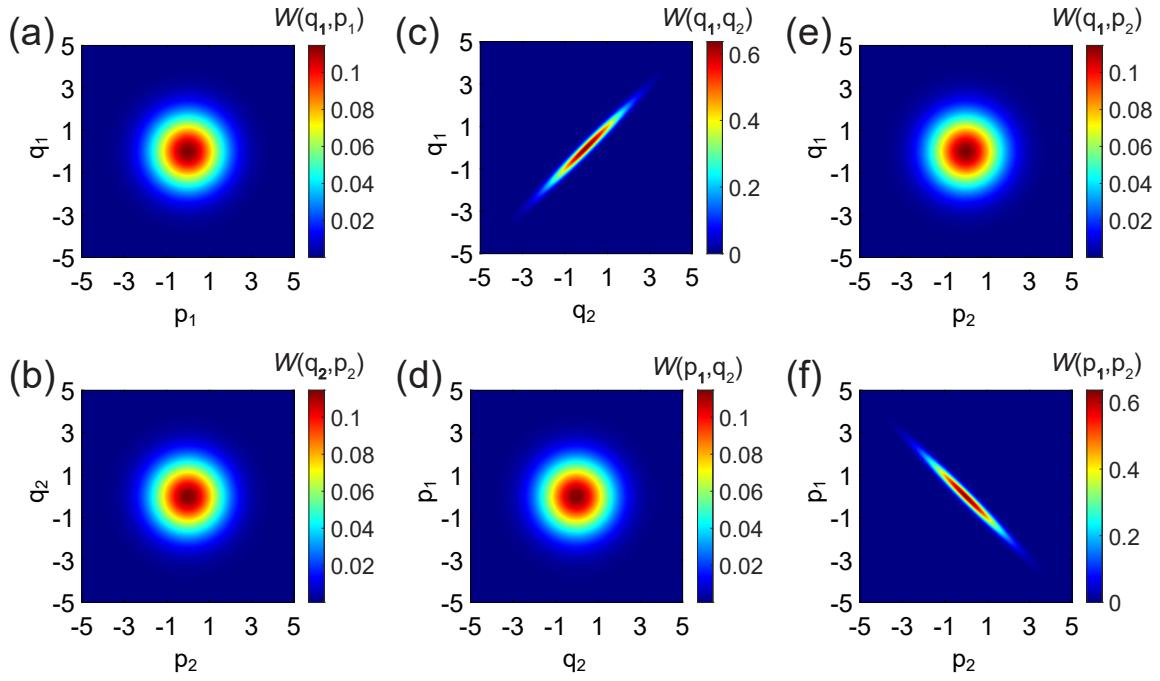

Figure 2.4: Marginal distributions of the Wigner function of a TMS state with $r = 1.2$ and $\varphi = 0$. Panels (a) and (b) are the local marginal distributions, which look like thermal states. Panels (c-f) are the marginal distributions of the nonlocal phase spaces, which give correlations in the quadrature pairs (q_1, q_2), (q_1, p_2), (p_1, q_2), and (p_1, p_2).

two-mode squeezed state with $\varphi = 0$ is given by [12]

$$\bar{\mathbf{r}}_{\mathrm{tms}} = \mathbf{0} \tag{2.34}$$

$$\mathbf{V}_{\mathrm{tms}} = \frac{1}{4}\begin{pmatrix} \cosh 2r & 0 & \sinh 2r & 0 \\ 0 & \cosh 2r & 0 & -\sinh 2r \\ \sinh 2r & 0 & \cosh 2r & 0 \\ 0 & -\sinh 2r & 0 & \cosh 2r \end{pmatrix}. \tag{2.35}$$

We see that the modes locally look like thermal states with a mean photon number $n_{\mathrm{th}} = \sinh^2 r$, such that there is no local squeezing in an ideal TMS state. Fig. 2.4 shows the Wigner functions of a TMS state. The correlation between modes are encoded in the off-diagonal block matrices in $\mathbf{V}_{\mathrm{tms}}$, which can also be seen from the Wigner function [12]

$$W(\mathbf{r}_{\mathrm{tms}}) = \frac{4}{\pi}\exp\left[-\frac{(q_1+q_2)^2+(p_1-p_2)^2}{e^{2r}} - \frac{(q_1-q_2)^2+(p_1+p_2)^2}{e^{-2r}}\right], \tag{2.36}$$

where $\mathbf{r}_{\mathrm{tms}} = (q_1, p_1, q_2, p_2)$. For ideal two-mode squeezing with $r \to \infty$, we have $W(\mathbf{r}_{\mathrm{tms}}) \to \delta(q_1 - q_2)\delta(p_1 + p_2)$. This means that the pair (q_1, q_2) is perfectly correlated and the pair (p_1, p_2) is perfectly anticorrelated. In our experiment, we generate TMS

states by mixing two orthogonally squeezed states via a symmetric hybrid ring, which is further explained in Section 4.1.2.

2.1.3 Continuous-variable quantum information

Continuous-variable quantum information employs physical observables with a continuous spectrum. CV quantum information has various applications in quantum communication [32], quantum computing [11, 12], and quantum sensing [33, 34]. In this section, we discuss quantum entanglement in Gaussian states and their application in quantum communication.

Quantum entanglement

Quantum entanglement is a signature property of quantum systems. By definition, a quantum system is entangled if its density operator $\hat{\rho}_{\mathrm{AB}}$ is inseparable. For a bipartite quantum state, the density operator is separable if it can be expressed as a convex sum of product states [35]

$$\hat{\rho}_{\mathrm{AB}} = \sum_i p_i \hat{\rho}_{i,\mathrm{A}} \otimes \hat{\rho}_{i,\mathrm{B}}, \tag{2.37}$$

where p_i is the probability to be in product state $\hat{\rho}_{i,\mathrm{A}} \otimes \hat{\rho}_{i,\mathrm{B}}$, with $\hat{\rho}_{i,\mathrm{A}}$ and $\hat{\rho}_{i,\mathrm{B}}$ the density matrices of the local systems. There are several measures to quantify the entanglement of two-mode Gaussian states [28]. For our work, we use the negativity N given by [28]

$$N = \max\left[0, \frac{1 - 4\tilde{\nu}_-}{8\tilde{\nu}_-}\right]. \tag{2.38}$$

The negativity is based on the positivitiy of the partial transpose of the density matrix [36], which is necessary and sufficient to determine the separability of two-mode Gaussian states [37]. The quantity $\tilde{\nu}_-$ is the smallest symplectic eigenvalue of the partially transposed density matrix [38]

$$\tilde{\nu}_\pm = \sqrt{\frac{\tilde{\Delta} \pm \sqrt{\tilde{\Delta}^2 - 4I_4}}{2}}, \tag{2.39}$$

where $\tilde{\Delta} = I_1 + I_2 - 2I_3$ with reference to Eq. 2.16. The two-mode Gaussian state is separable if $\tilde{\nu}_- \geq 1/4$ and is entangled otherwise. As a result, a positive negativity N implies entanglement and $N \to \infty$ for maximally entangled states.

Quantum communication

Quantum communication is used to transfer quantum states or to improve classical communications. Quantum resources can be exploited to achieve advantages over classical communication in terms of efficiency and security. For example, entanglement can be used to implement superdense coding and the no-cloning theorem can guarantee secure

communication via quantum key distribution [11, 12]. In particular, our work focuses on the quantum teleportation protocol, which allows the disembodied transfer of unknown quantum states and unconditionally secure communication of classical information. Details about the theory and implementation of quantum teleportation are presented in Chapter 3.

2.2 Josephson parametric amplifier

One of the central building blocks for our experiments conducted throughout this work is the Josephson parametric amplifier [16, 39, 40]. A flux-driven JPA [41] is a superconducting resonator that consists of a coplanar waveguide (CPW) short-circuited to ground via a direct current superconducting quantum interference device. The JPA can be used to achieve parametric amplification of microwave signals and to generate squeezed states.

2.2.1 Josephson junctions

The Josephson effect [42] occurs when two superconductors are weakly coupled to each other, often by introducing a thin insulating barrier and forming a Josephson junction. This macroscopic quantum phenomenon is described by the first and second Josephson equations [43]

$$I_\mathrm{s}(\varphi) = I_\mathrm{c}\sin(\varphi), \tag{2.40}$$

$$\frac{\partial\varphi}{\partial t} = \frac{2\pi}{\Phi_0}V(t), \tag{2.41}$$

where φ is the gauge-invariant phase difference across the junction, I_s is the supercurrent through the junction, I_c is the Josephson critical current, $V(t)$ is the voltage across the junction, and $\Phi_0 = h/(2e)$ is the magnetic flux quantum. We see that a constant voltage V applied across the Josephson junction causes a sinusoidal oscillation in the supercurrent I_s. We can then use the definition of inductance $V = LdI/dt$ to obtain the nonlinear inductance of the Josephson junction [43]

$$L_\mathrm{s}(\varphi) = \frac{\Phi_0}{2\pi I_\mathrm{c}\cos(\varphi)} = L_\mathrm{c}\frac{1}{\cos(\varphi)}, \tag{2.42}$$

where $L_\mathrm{c} = \Phi_0/(2\pi I_\mathrm{c})$ is the minimum junction inductance. The Josephson junction is a crucial component in superconducting circuits, since it is often used as a nonlinear and lossless inductance.

2.2.2 DC-SQUID

The direct current superconducting quantum interference devices is a powerful quantum device and consists of two Josephson junctions in a superconducting loop. For simplicity, we assume that the two Josephson junctions have the same critical current I_c. Then, the phase difference between the Josephson junctions is given by

$$\varphi_1 - \varphi_2 = \frac{2\pi\Phi}{\Phi_0} + 2\pi n. \tag{2.43}$$

where $n \in \mathbb{Z}_0$ and Φ is the total magnetic flux through the loop. The total magnetic flux $\Phi = \Phi_{\text{ext}} + L_{\text{loop}} I_{\text{circ}}$ can be decomposed into the externally applied flux Φ_{ext} and the self-induced flux $L_{\text{loop}} I_{\text{circ}}$, where L_{loop} is the self-inductance of the superconducting loop and I_{circ} is the circulating current. The total flux through the DC-SQUID loop is given by

$$\frac{\Phi}{\Phi_0} = \frac{\Phi_{\text{ext}}}{\Phi_0} - \frac{\beta_{\text{L}}}{2} \cos\left(\frac{\varphi_1 + \varphi_2}{2}\right) \sin\left(\frac{\varphi_1 - \varphi_2}{2}\right), \tag{2.44}$$

where $\beta_{\text{L}} \equiv 2L_{\text{loop}} I_c / \Phi_0$ is the screening parameter [44]. In the case $\beta_{\text{L}} \simeq 0$, the self-induced flux can be neglected and we have $\Phi \approx \Phi_{\text{ext}}$. We can express a maximum transport current of the DC-SQUID [43]

$$I_s^{\max}(\Phi_{\text{ext}}) = 2I_c \left| \cos\left(\pi \frac{\Phi_{\text{ext}}}{\Phi_0}\right) \right|. \tag{2.45}$$

In this regime, the DC-SQUID can be viewed as a single Josephson junction with maximum supercurrent modulated by an external flux. We can then express a flux-tunable inductance of the DC-SQUID [45]

$$L_s(\Phi_{\text{ext}}) = \frac{\Phi_0}{4\pi I_c \left| \cos\left(\pi \frac{\Phi_{\text{ext}}}{\Phi_0}\right) \right|}. \tag{2.46}$$

This implies that the DC-SQUID can be regarded as a flux-tunable inductance, and we can exploit it as a nonlinear building block in superconducting circuits.

2.2.3 Coplanar waveguide resonators

The coplanar waveguide is a central element of the JPA and acts as a quasi-one-dimensional transmission line. Since the physical dimensions of the CPW is comparable to microwave wavelengths, we should describe the CPW with a distributed-element model as shown by the schematic in Fig. 2.5. Furthermore, we can neglect losses in the superconducting CPW and use the telegrapher's equations to derive its characteristic impedance [18]

$$Z = \sqrt{\frac{L_0}{C_0}} \tag{2.47}$$

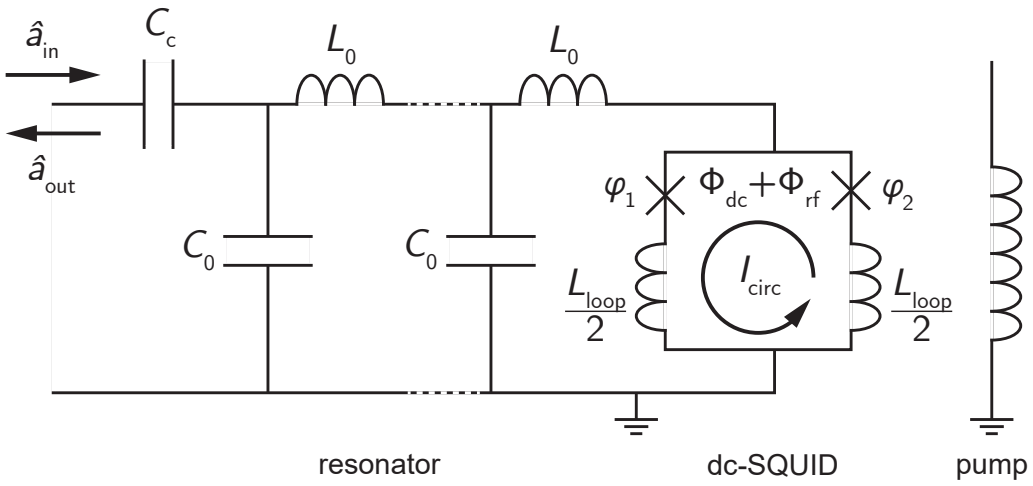

Figure 2.5: Circuit diagram of a JPA that consists of a CPW resonator short-circuited to ground via a DC-SQUID. The crosses denote Josephson junctions. The DC-SQUID inductively couples to the external magnetic flux $\Phi_{\mathrm{DC}} + \Phi_{\mathrm{rf}}$. The alternating flux Φ_{rf} is generated by the adjacent pump line.

where L_0 and C_0 denote the respective inductance and capacitance per unit length of the transmission line. We apply boundary conditions on the waves propagating through the transmission line to create a resonator. At one end, the CPW is capacitively coupled with capacitance C_{c}, which defines the external quality factor and hence the coupling to external fields. At the other end, the CPW is short-circuited to ground. This creates a quarter-wavelength resonator with electrical length d. The fundamental resonance frequency is given by [18]

$$f_{\mathrm{res}} = \frac{1}{4d\sqrt{L_0 C_0}} = \frac{1}{4\sqrt{L_{\mathrm{res}} C_{\mathrm{res}}}}, \tag{2.48}$$

where $L_{\mathrm{res}} = dL_0$ is the resonator inductance and $C_{\mathrm{res}} = dC_0$ is the resonator capacitance. We observe that changing the inductance L_{res} with the flux-dependent DC-SQUID by Eq. 2.46 would change the resonance frequency f_{res}. Therefore, the resonance frequency becomes tunable with an external flux.

The resonator can be characterized by its quality factor, defined as [18]

$$Q = 2\pi \frac{\text{average energy stored}}{\text{energy loss/cycle}} = \frac{\omega_{\mathrm{res}}}{\kappa_{\mathrm{int}} + \kappa_{\mathrm{ext}}}, \tag{2.49}$$

where $\omega_{\mathrm{res}} = 2\pi f_{\mathrm{res}}$ is the angular resonance frequency, κ_{int} is the internal loss rate, and κ_{int} is the external loss rate. The internal quality factor $Q_{\mathrm{int}} = \kappa_{\mathrm{int}}/\omega_{\mathrm{res}}$ provides information about internal losses of the resonator, where κ_{int} is determined by the sum of various

loss mechanisms. The external quality factor $Q_{\text{ext}} = \kappa_{\text{ext}}/\omega_{\text{res}}$ determines the coupling strength to the signal port, where the κ_{ext} is mainly defined by the coupling capacitance. The internal and external quality factors can be experimentally measured.

2.2.4 Flux-driven parametric amplification

In our experiments, we use flux-driven JPAs [41] to generate squeezed states and to produce signal gain. The flux-driven JPA can be described using the input-output formalism developed by Yamamoto *et al.* [46]. We begin with an unperturbed harmonic oscillator that has resonance frequency ω_0 and then introduce a periodic modulation such that $\omega_0 \rightarrow \omega_0[1 + \epsilon/2\cos(\alpha\omega_0 t)]$, where $\epsilon/2$ is the amplitude of modulation and $\alpha\omega_0$ is the frequency of modulation. We consider only small modulation amplitudes and can write the JPA Hamiltonian as

$$\hat{H}(t) = \hbar\omega_0 \left[\hat{a}^\dagger\hat{a} + \frac{1}{2} + \epsilon\cos(\alpha\omega_0 t)(\hat{a} + \hat{a}^\dagger)^2\right]. \tag{2.50}$$

By introducing a signal and loss port to the oscillator, we can solve for the output field of the JPA in the rotating frame with frequency $\alpha\omega_0$. More details on the derivation can be found in Ref. [46]. Ideal parametric amplification occurs when we have pump frequency $\omega_{\text{pump}} = 2\omega_0$. The resonance frequency f_0 can be chosen by applying a direct current flux Φ_{DC} through the DC-SQUID loop.

The parametric amplification process can be described as a three-wave mixing process characterized by [16]

$$\omega_{\text{pump}} = \omega_{\text{signal}} + \omega_{\text{idler}}, \tag{2.51}$$

where ω_{pump} is the pump mode frequency, ω_{signal} is the signal mode frequency, and ω_{idler} is the idler mode frequency. The pump photon splits into one signal photon and one idler mode such that energy is conserved. When $\omega_{\text{pump}} \neq 2\omega_{\text{signal}}$, we have nondegenerate or phase insensitive amplification. When $\omega_{\text{pump}} = 2\omega_{\text{signal}}$, we have degenerate or phase sensitive amplification. Due to strong quantum correlations between the signal and idler modes, interference between these modes in the degenerate regime causes squeezing.

Amplification processes can be characterized by their power gain. In any amplification procedure, it is important to consider the amplification noise added to the signal. For phase insensitive amplification, the minimum number of added noise photons is bounded by [47]

$$n_{\text{amp}} \geq \frac{1}{2}\left|1 - \frac{1}{G_{\text{s}}}\right|, \tag{2.52}$$

where G_{s} is the gain in the signal mode. We see that in the limit of large gain, at least half a noise photon is added to the signal. For phase sensitive amplification, one quadrature is amplified, while the orthogonal is deamplified. In this case, the number of added noise

photons is given by [47]

$$n_1 n_2 \geq \frac{1}{16}\left|1 - \frac{1}{\sqrt{G_1 G_2}}\right|^2, \tag{2.53}$$

where η_1, η_2 are the added noise photons for each quadrature and G_1, G_2 are the gains for each quadrature. We observe that we can obtain noiseless amplification when $G_1 G_2 = 1$. This implies the possibility of noiseless amplification of one quadrature if the conjugate quadrature is simultaneously deamplified by the inverse gain, which corresponds to the squeezing operation. When using a flux-driven JPA in the phase sensitive regime, the JPA Hamiltonian generates a unitary evolution that corresponds to the squeezing operator [12]

$$\hat{U}(t) = \exp\left[-\frac{i}{\hbar}\hat{H}_{\text{int}} t\right] = \exp\left[\frac{\lambda}{2}\left(\hat{a}^2 e^{-i\varphi} - (\hat{a}^\dagger)^2 e^{i\varphi}\right) t\right], \tag{2.54}$$

where $\hat{H}_{\text{int}}$ is the JPA Hamiltonian in the interaction picture, λ is the effective frequency modulation, and φ is the pump tone phase. We can identify the squeezing factor $r = \lambda t$ to recover the original squeezing operator in Eq. 2.28.

Furthermore, the JPA degenerate gain can be parameterized as [46]

$$G_{\text{d}}(\theta) = \frac{\left(\frac{\kappa_{\text{ext}}^2 - \kappa_{\text{int}}^2}{4} - 4\chi^2\omega_0^2\right)^2 + 4\chi^2\kappa_{\text{ext}}^2\omega_0^2 - 4\chi\kappa_{\text{ext}}\omega_0\left(\frac{\kappa_{\text{ext}}^2 - \kappa_{\text{int}}^2}{4} - 4\chi^2\omega_0^2\right)\sin(2\theta)}{\left(\frac{(\kappa_{\text{ext}} + \kappa_{\text{int}})^2}{4} - 4\chi^2\omega_0^2\right)^2}, \tag{2.55}$$

where θ is the phase difference between the signal mode and pump tone and χ is the pump tone amplitude. The maximum and minimum gains, describing amplification and deamplification, can be written as [46]

$$G_{\text{d}}^{\max} = \left(\frac{2\chi\omega_0 - (\kappa_{\text{ext}} - \kappa_{\text{int}})/2}{2\chi\omega_0 + (\kappa_{\text{ext}} + \kappa_{\text{int}})/2}\right)^2, \quad \text{for } \theta \equiv \frac{\pi}{4} \pmod{\pi} \tag{2.56}$$

$$G_{\text{d}}^{\min} = \left(\frac{2\chi\omega_0 + (\kappa_{\text{ext}} - \kappa_{\text{int}})/2}{2\chi\omega_0 - (\kappa_{\text{ext}} + \kappa_{\text{int}})/2}\right)^2, \quad \text{for } \theta \equiv \frac{3\pi}{4} \pmod{\pi} \tag{2.57}$$

where we assume $\kappa_{\text{ext}} > \kappa_{\text{int}}$. If we have $\kappa_{\text{int}} = 0$, then we obtain the condition $G_{\text{d}}^{\max} G_{\text{d}}^{\min}$ for noiseless amplification.

Chapter 3

Quantum teleportation

Quantum communication utilizes the fundamental laws of quantum physics to exceed the performance of classical communication protocols regarding efficiency and security. One of the most famous quantum communication protocols is quantum teleportation, where an unknown quantum state is transferred between two distant communication parties using a shared entanglement resource and a classical feedforward channel [48, 49]. Quantum teleportation has been implemented in both discrete variable systems [50] and continuous variable systems [32]. Continuous variable quantum communication is especially advantageous due to its high bit rates [51], and has ongoing research in quantum key distribution [52], quantum teleportation [14], and open-air quantum communication [53].

In this chapter, we explain the analog quantum teleportation protocol realized in our experiment. In Section 3.1, we discuss the principles of quantum teleportation. We describe the general teleportation protocol and the criteria for successful quantum teleportation. In Section 3.2, we present continuous-variable (CV) quantum teleportation with Gaussian states. We discuss the security of this teleportation protocol and the practical requirement of using finite-energy codebooks. In Section 3.3, we introduce teleportation over thermal channels. We describe the effect of thermal noise on the performance of quantum teleportation and demonstrate that the protocol realizes an error correction scheme for Gaussian imperfections.

3.1 Principles of quantum teleportation

Quantum teleportation is a quantum communication protocol that enables the transfer of quantum states without directly sending them. In order to accomplish this protocol, a quantum entanglement resource is shared between the communication parties and consumed during communication. In general, the quantum teleportation protocol can be used to transfer unknown quantum states, which is useful for quantum information processing procedures such as quantum gate teleportation and entanglement swapping [54]. Also, the quantum nature of this protocol implies that it cannot be perfectly eavesdropped and can enable unconditionally secure classical communication.

3.1.1 General framework for quantum teleportation

Quantum teleportation enables the disembodied transfer of unknown quantum states between two spatially separated communication parties, conventionally named as Alice and Bob. In a general quantum teleportation experiment, Alice utilizes a predistributed entanglement resource and a classical feedforward channel to transmit an unknown input state to Bob. Alice begins by entangling the input state with her part of the shared entangled state and then performs a Bell measurement on the resulting bipartite state. The measurement outcome is sent to Bob as a classical signal through the feedforward channel. Depending on Alice's measurement outcome, Bob then performs a local unitary operation on his part of the shared entangled state, which lets him recreate the input state. For a continuous-variable teleportation protocol, the entanglement resource is a TMS state, the Bell measurement is a joint quadrature measurement by Alice, and the local unitary is a phase-space displacement by Bob [12].

In the teleportation protocol, the input state can be unknown to Alice and Bob, otherwise Alice could just provide classical instructions for Bob to prepare the state. The no-cloning theorem is not violated, since the input state is altered due to the Bell measurement [12]. Furthermore, special relativity is not violated, since a classical signal is required, which excludes faster-than-light communication.

3.1.2 Fidelity criteria for quantum teleportation

After performing the teleportation protocol, it is necessary to verify whether quantum teleportation has worked successfully. Successful teleportation can be determined by measuring the statistical overlap of input and output states, with the general formula for fidelity in Eq. 2.6. For single-mode Gaussian states, we can calculate the Uhlmann fidelity by

$$F(\bar{\mathbf{r}}_{\text{in}}, \mathbf{V}_{\text{in}}, \bar{\mathbf{r}}_{\text{out}}, \mathbf{V}_{\text{out}}) = \frac{1}{2} \frac{\exp(-\frac{1}{2}\delta^{\intercal}(\mathbf{V}_{\text{in}} + \mathbf{V}_{\text{out}})^{-1}\delta)}{\sqrt{\boldsymbol{\Lambda} + \boldsymbol{\Delta}} - \sqrt{\boldsymbol{\Lambda}}}, \tag{3.1}$$

where we write

$$\delta = \bar{\mathbf{r}}_{\text{in}} - \bar{\mathbf{r}}_{\text{out}} \tag{3.2}$$

$$\boldsymbol{\Lambda} = \det(\mathbf{V}_{\text{in}} + \mathbf{V}_{\text{out}}) \tag{3.3}$$

$$\boldsymbol{\Delta} = 16 \left(\det \mathbf{V}_{\text{in}} - \frac{1}{16}\right) \left(\det \mathbf{V}_{\text{out}} - \frac{1}{16}\right), \tag{3.4}$$

and where $\bar{\mathbf{r}}_{\text{in}}$ and $\mathbf{V}_{\text{in}}$ are the input state displacement and covariance, and $\bar{\mathbf{r}}_{\text{out}}$ and $\mathbf{V}_{\text{out}}$ are the output state displacement and covariance. The fidelity equals one if the input and output states coincide, and equals zero if the they are orthogonal. The input state can be drawn from a codebook with probability distribution $P(\bar{\mathbf{r}}_{\text{in}})$, but the particular state of

each teleportation event is unknown. Thus, we use the average fidelity

$$\bar{F} = \int P(\bar{\mathbf{r}}_{\text{in}}) F(\bar{\mathbf{r}}_{\text{in}}, \mathbf{V}_{\text{in}}, \bar{\mathbf{r}}_{\text{out}}, \mathbf{V}_{\text{out}}) d\bar{\mathbf{r}}_{\text{in}}. \tag{3.5}$$

If the codebook of input states includes all possible coherent states, the best attainable classical teleportation average fidelity is bounded by [55]

$$\bar{F}_{\text{classical}} \leq \frac{1}{2}. \tag{3.6}$$

Here, we define "classical teleportation" as the teleportation protocol without having entanglement. In order to verify quantum teleportation, we need $\bar{F} > \max \bar{F}_{\text{classical}} = 1/2$, which is obtained for any finite entanglement in an idealistic scenario.

The unconditional security of quantum teleportation can also be verified by the fidelity. For an infinitely large codebook of coherent input states, this is achieved when the fidelity exceeds the asymptotic no-cloning threshold $\bar{F} > \bar{F}_{\text{no-cloning}} = 2/3$ [56]. However, in realistic application scenarios, infinitely large codebooks cannot be implemented, which leads to no-cloning thresholds larger than 2/3. The influence of finite-energy codebooks is further discussed in 3.2.3.

3.2 Gaussian quantum teleportation with analog feedforward

In our experiment, we realize the continuous-variable quantum teleportation protocol with an analog classical feedforward signal. In this section, we describe the CV teleportation protocol and present the formalism for Gaussian quantum teleportation. We also discuss the security of quantum teleportation and analyze the influence of a finite-energy codebook. The analog CV quantum teleportation of coherent quantum states is schematically depicted in Fig. 3.1.

3.2.1 Continuous-variable teleportation

In the CV quantum teleportation protocol, the entanglement resource is a TMS state with squeezing level S, the Bell measurement by Alice is a joint quadrature measurement, and the unitary operation by Bob is a displacement in phase-space. In experiment, the Bell measurement is performed with a heterodyne detection setup, consisting of two phase-sensitive amplifiers which amplify orthogonal quadratures with a gain $G \gg 1$. The resulting analog classical signal is then directly transmitted to Bob, who performs his displacement operation by employing an asymmetric beam splitter that couples the feedforward signal to his part of the resource state with coupling $\beta \ll 1$. As demonstrated in Ref. [14], the joint action of the analog detector and the asymmetric beam splitter

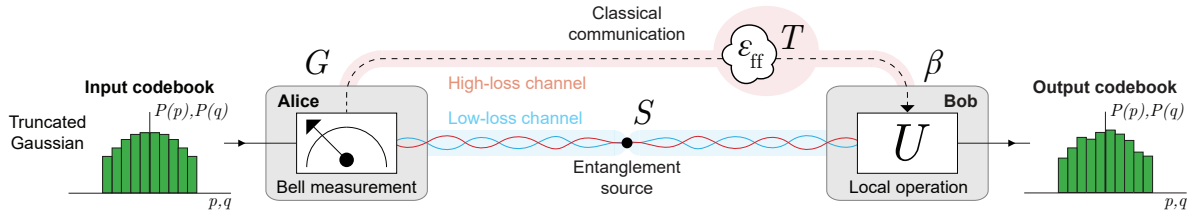

Figure 3.1: Schematic of a realistic quantum teleportation protocol. A two-mode squeezed state is shared between Alice and Bob through a low-loss quantum channel. Alice performs a Bell operation on a codeword and her entangled state and the measurement result is sent to Bob through a high-loss feedforward channel. Bob performs a local operation on his entangled state according to the feedforward signal and obtains the teleported codeword. An ensemble of codewords constructs the codebook, which follows a truncated Gaussian distribution.

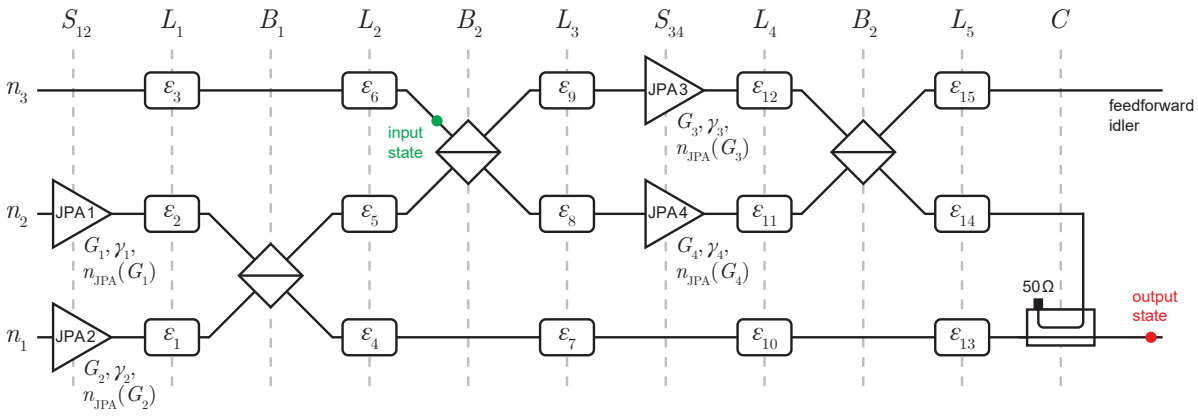

Figure 3.2: Schematic for realistic continuous-variable quantum teleportation. Ambient thermal noise is coupled to the quantum states through losses ε_i via the loss operators $\hat{L}_k$. Gain-depended noise $n_j(G_j)$ is considered for each JPA.

realizes a projective measurement if we meet the criterion $G\beta = 4$. This is the case where the feedforward gain exactly compensates the two beam splitters in the heterodyne detection scheme as well as the coupling β [49]. In the following, we present the formalism for the analog CV teleportation protocol [14], which is schematically depicted in Fig. 3.2.

We need three propagating microwave channels to describe the teleportation protocol: channel 1 for the resource state at Bob, channel 2 for the resource state at Alice, and channel 3 for the input state. We introduce a unitary operator for each of the microwave components involved in the quantum teleportation protocol. We also introduce loss matrices L_i and noise matrices A_i, N_i to model the experimental imperfections of the

protocol. For ease of notation, we define the amplification and rotation matrices

$$\mathrm{Amp}(G) \equiv \begin{pmatrix} G^{-\frac{1}{2}} & 0 \\ 0 & G^{\frac{1}{2}} \end{pmatrix}, \quad \mathrm{Rot}(\gamma) \equiv \begin{pmatrix} \cos\gamma & \sin\gamma \\ -\sin\gamma & \cos\gamma \end{pmatrix}. \tag{3.7}$$

Since we consider only Gaussian states, quadrature moments up to the second order are sufficient to fully describe the quantum states. Thus, it is sufficient to analyze the teleportation protocol on the displacement vector d and covariance matrix V. We begin with the initial displacement vector and covariance matrix

$$d_0 = (0, 0, 0, 0, \sqrt{n_d}\cos\phi_d, \sqrt{n_d}\sin\phi_d)^\intercal, \tag{3.8}$$

$$V_0 = \frac{1}{4}\begin{pmatrix} (1+2n_1)\mathbb{I}_2 & \mathbb{0}_2 & \mathbb{0}_2 \\ \mathbb{0}_2 & (1+2n_2)\mathbb{I}_2 & \mathbb{0}_2 \\ \mathbb{0}_2 & \mathbb{0}_2 & (1+2n_3)\mathbb{I}_2 \end{pmatrix}, \tag{3.9}$$

where n_d is the initial displacement photon number, ϕ_d is the initial displacement angle, n_1, n_2, n_3 are the initial noise photons in the respective channels, $\mathbb{I}_2$ is the 2×2 identity matrix, and $\mathbb{0}_2$ is the 2×2 zero matrix. JPA1 and JPA2 are used to generate the squeezed states for the TMS entanglement resource. This squeezing operation J_{12} is given by

$$S_{12} = \begin{pmatrix} \mathrm{Amp}(e^{2r_1}) & \mathbb{0}_2 & \mathbb{0}_2 \\ \mathbb{0}_2 & \mathrm{Amp}(e^{2r_2}) & \mathbb{0}_2 \\ \mathbb{0}_2 & \mathbb{0}_2 & \mathbb{I}_2 \end{pmatrix}, \quad R_{12} = \begin{pmatrix} \mathrm{Rot}(\gamma_1) & \mathbb{0}_2 & \mathbb{0}_2 \\ \mathbb{0}_2 & \mathrm{Rot}(\gamma_2) & \mathbb{0}_2 \\ \mathbb{0}_2 & \mathbb{0}_2 & \mathbb{I}_2 \end{pmatrix}, \tag{3.10}$$

$$J_{12} = R_{12} S_{12} R_{12}^\dagger, \tag{3.11}$$

where r_1, r_2 are the squeezing factors for the respective JPAs and γ_1, γ_2 are the squeezing angles for the respective JPAs. The symmetric beam splitter operations B_1, B_2 used to superimpose the channels are given by

$$B_1 = \frac{1}{\sqrt{2}}\begin{pmatrix} \mathbb{I}_2 & \mathbb{I}_2 & \mathbb{0}_2 \\ -\mathbb{I}_2 & \mathbb{I}_2 & \mathbb{0}_2 \\ \mathbb{0}_2 & \mathbb{0}_2 & \sqrt{2}\mathbb{I}_2 \end{pmatrix}, \quad B_2 = \frac{1}{\sqrt{2}}\begin{pmatrix} \sqrt{2}\mathbb{I}_2 & \mathbb{0}_2 & \mathbb{0}_2 \\ \mathbb{0}_2 & \mathbb{I}_2 & \mathbb{I}_2 \\ \mathbb{0}_2 & -\mathbb{I}_2 & \mathbb{I}_2 \end{pmatrix}. \tag{3.12}$$

JPA3 and JPA4 are used for the phase-sensitive amplification to implement the Bell

measurement. This amplification operation J_{34} is given by

$$S_3 = \begin{pmatrix} \mathbb{I}_2 & \mathbb{0}_2 & \mathbb{0}_2 \\ \mathbb{0}_2 & \mathrm{Amp}(G_3) & \mathbb{0}_2 \\ \mathbb{0}_2 & \mathbb{0}_2 & \mathbb{I}_2 \end{pmatrix}, \quad R_3 = \begin{pmatrix} \mathbb{I}_2 & \mathbb{0}_2 & \mathbb{0}_2 \\ \mathbb{0}_2 & \mathrm{Rot}(\gamma_3) & \mathbb{0}_2 \\ \mathbb{0}_2 & \mathbb{0}_2 & \mathbb{I}_2 \end{pmatrix}, \tag{3.13}$$

$$S_4 = \begin{pmatrix} \mathbb{I}_2 & \mathbb{0}_2 & \mathbb{0}_2 \\ \mathbb{0}_2 & \mathbb{I}_2 & \mathbb{0}_2 \\ \mathbb{0}_2 & \mathbb{0}_2 & \mathrm{Amp}(G_4) \end{pmatrix}, \quad R_4 = \begin{pmatrix} \mathbb{I}_2 & \mathbb{0}_2 & \mathbb{0}_2 \\ \mathbb{0}_2 & \mathbb{I}_2 & \mathbb{0}_2 \\ \mathbb{0}_2 & \mathbb{0}_2 & \mathrm{Rot}(\gamma_4) \end{pmatrix}, \tag{3.14}$$

$$J_{34} = R_3 S_3 R_3^\dagger R_4 S_4 R_4^\dagger, \tag{3.15}$$

where G_3, G_4 are the gain factors for the respective JPAs and γ_3, γ_4 are the measurement angles for the respective JPAs. The directional coupler is used to perform the state displacement by Bob. This displacement operation C is given by

$$C = \begin{pmatrix} \sqrt{1-\beta}\mathbb{I}_2 & \sqrt{\beta}\mathbb{I}_2 & \mathbb{0}_2 \\ -\sqrt{\beta}\mathbb{I}_2 & \sqrt{1-\beta}\mathbb{I}_2 & \mathbb{0}_2 \\ \mathbb{0}_2 & \mathbb{0}_2 & \mathbb{I}_2 \end{pmatrix}, \tag{3.16}$$

where β is the coupling strength. The losses L_i and noise A_i, N_i incurred between microwave components are modelled by

$$L_i = \begin{pmatrix} \sqrt{1-\varepsilon_{3(i-1)+1}}\mathbb{I}_2 & \mathbb{0}_2 & \mathbb{0}_2 \\ \mathbb{0}_2 & \sqrt{1-\varepsilon_{3(i-1)+2}}\mathbb{I}_2 & \mathbb{0}_2 \\ \mathbb{0}_2 & \mathbb{0}_2 & \sqrt{1-\varepsilon_{3(i-1)+3}}\mathbb{I}_2 \end{pmatrix}, \tag{3.17}$$

$$A_i = \frac{1}{4}(1+2n_{\mathrm{th}}) \begin{pmatrix} \varepsilon_{3(i-1)+1}\mathbb{I}_2 & \mathbb{0}_2 & \mathbb{0}_2 \\ \mathbb{0}_2 & \varepsilon_{3(i-1)+2}\mathbb{I}_2 & \mathbb{0}_2 \\ \mathbb{0}_2 & \mathbb{0}_2 & \varepsilon_{3(i-1)+3}\mathbb{I}_2 \end{pmatrix} \tag{3.18}$$

where $i \in \{1,2,3,4,5\}$, ε_j are the local losses, and n_{th} is the ambient thermal photon number. The noise added by JPA3 and JPA4 is modelled by

$$N_3 = \frac{n_{\mathrm{JPA}}(G_3)}{2} \begin{pmatrix} \mathbb{0}_2 & \mathbb{0}_2 & \mathbb{0}_2 \\ \mathbb{0}_2 & \mathbb{I}_2 & \mathbb{0}_2 \\ \mathbb{0}_2 & \mathbb{0}_2 & \mathbb{0}_2 \end{pmatrix}, \quad N_4 = \frac{n_{\mathrm{JPA}}(G_4)}{2} \begin{pmatrix} \mathbb{0}_2 & \mathbb{0}_2 & \mathbb{0}_2 \\ \mathbb{0}_2 & \mathbb{0}_2 & \mathbb{0}_2 \\ \mathbb{0}_2 & \mathbb{0}_2 & \mathbb{I}_2 \end{pmatrix}, \tag{3.19}$$

where $n_{\mathrm{JPA}}(G_3)$, $n_{\mathrm{JPA}}(G_4)$ are the gain-dependent noise photon numbers. We model the gain-dependent noise by $n_{\mathrm{JPA}} = \chi_1(G_i - 1)^{\chi_2}$, where G_i is the degenerate gain for JPA i, and χ_1 and χ_1 are parameters fit to measurement data. We can then write the teleportation protocol as

$$T = CL_5B_2L_4J_{34}L_3B_2L_2B_1L_1J_{12}. \tag{3.20}$$

The input state displacement vector d_i, final state displacement vector d_f, and final state covariance matrix V_f can be found by

$$d_\mathrm{i} = L_2 B_1 L_1 S_{12} d_0 \equiv (d_{\mathrm{i},1}, d_{\mathrm{i},2}, d_{\mathrm{i},3})^\intercal, \tag{3.21}$$

$$d_\mathrm{f} = T d_0 \equiv (d_{\mathrm{f},1}, d_{\mathrm{f},2}, d_{\mathrm{f},3})^\intercal, \tag{3.22}$$

$$V_\mathrm{f} = T V_0 T^\dagger + A, \tag{3.23}$$

where the noise term is given by

$$\begin{aligned} A = {} & C L_5 B_2 L_4 J_{34} L_3 B_2 L_2 B_1 A_1 B_1^\dagger L_2^\dagger B_2^\dagger L_3^\dagger J_{34}^\dagger L_4^\dagger B_2^\dagger L_5^\dagger C^\dagger \\ & + C L_5 B_2 L_4 J_{34} L_3 B_2 A_2 B_2^\dagger L_3^\dagger J_{34}^\dagger L_4^\dagger B_2^\dagger L_5^\dagger C^\dagger \\ & + C L_5 B_2 L_4 J_{34} (A_3 + N_3 + N_4) J_{34}^\dagger L_4^\dagger B_2^\dagger L_5^\dagger C^\dagger \\ & + C L_5 B_2 A_4 B_2^\dagger L_5^\dagger C^\dagger \\ & + C A_5 C^\dagger. \end{aligned} \tag{3.24}$$

The Uhlmann fidelity can then be calculated from the displacement vectors and covariance matrices. A detailed description of the theory model can be found in the supplementary material of Ref. [14].

For the output state to match the input state, we require $d_{\mathrm{f},1} = d_{\mathrm{i},3}$. Assuming that there are no losses in the protocol, this condition is achieved when $G\beta = 4$. We further assume that there is no JPA amplification noise and take $G \to \infty$ for an ideal Bell measurement. The Ulhmann fidelity is then given by

$$F = \frac{1}{1 + e^{-2r}}, \tag{3.25}$$

where r is the common squeezing factor of JPA1 and JPA2. As expected, in such an ideal teleportation protocol, the maximum fidelity is obtained when $r \to \infty$, corresponding to perfect quantum correlations in the TMS state. In the ideal protocol, the asymptotic classical limit $F = 1/2$ is recovered when $r = 0$, and the asymptotic no-cloning threshold $F = 2/3$ is exceeded when $r \approx 0.35$. In experiment, a quantum advantage is achieved when the teleportation fidelity exceeds the classical limit, and unconditionally secure communication is guaranteed when the teleportation fidelity exceeds the no-cloning threshold.

3.2.2 Security of teleportation protocol

Quantum teleportation promises secure exchange of information between remote parties [57]. As a result of the no-cloning theorem, unconditional security is provided when teleportation fidelities beyond the no-cloning threshold are reached. For continuous variable quantum teleportation with Gaussian states, the optimal attack of an eavesdropper

Eve to intercept the message from Alice is to clone the quantum state that is sent, such that one copy is kept and the other one is transmitted to Bob. This optimal cloning scheme for Gaussian codebooks is described in Refs. [58–60] and requires Eve to have a priori knowledge about the codebook of transmitted states. For coherent state quantum teleportation, this codebook can be described by a probability distribution $P(\alpha)$. In the case that $P(\alpha)$ covers the whole phase-space, it can be shown that Eve's attack results in a no-cloning threshold for the average teleportation fidelity of $\bar{F}_{\mathrm{nc}} = 2/3$. Hence, if Bob measures an average teleportation fidelity beyond 2/3, he knows with certainty that the state has not been cloned.

We review the results for a codebook in a Gaussian distribution [59], where an optimal cloning scheme is known. A Gaussian codebook has a probability distribution

$$P_\sigma(\alpha) = \frac{1}{2\pi\sigma^2} e^{-|\alpha|^2/2\sigma^2}, \tag{3.26}$$

where α is a particular state amplitude and σ is the codebook variance. The optimal average cloning fidelity is given by

$$F_\sigma \leq \begin{cases} \frac{4\sigma^2+2}{6\sigma^2+1} & \sigma^2 \geq \frac{1}{2} + \frac{1}{\sqrt{2}} \\ \frac{1}{(3-2\sqrt{2})\sigma^2+1} & \sigma^2 \leq \frac{1}{2} + \frac{1}{\sqrt{2}}. \end{cases} \tag{3.27}$$

This fidelity defines the no-cloning threshold for a Gaussian codebook, and quantum teleportation is unconditionally secure if the measured average fidelity exceeds this threshold. We see that in the limit of a infinitely large and uniformly distributed codebook as $\sigma \to \infty$, the no-cloning fidelity approaches the asymptotic value $F_\sigma \to 2/3$.

Nevertheless, in a realistic application scenario, it is not possible to teleport coherent states with arbitrarily large displacement photon numbers due to finite energy capacities and limiting effects such as amplifier compression in the Bell measurement setup. These restrictions limit the codebook size and eventually lead to higher no-cloning thresholds $\bar{F}_{\mathrm{nc}} > 2/3$. Lastly, we note that the optimal cloning machine for coherent states is non-Gaussian and leads to an optimal cloning fidelity 0.68 [60]. In a quantum teleportation experiment, such a non-Gaussian cloner can be ruled-out by checking the statistics of the Bell-like measurements, which should be Gaussian for a Gaussian state input.

3.2.3 Finite-energy codebook

In the following, we consider the influence of employing a finite realistic codebook on the no-cloning limit and thereby on the unconditional security of Gaussian quantum teleportation[1]. Such a practical codebook should show polar symmetry in phase-space to

[1] We acknowledge that the work related to the finite-energy codebook has been done in close collaboration with Dr. Roberto Di Candia. In particular, the calculations for finding an upper bound on the no-cloning threshold emerge from the ideas of Di Candia.

have no constraint on the signal phase, which can contain the information in teleportation-based application scenarios such as quantum key distribution. For these purposes, we choose a truncated Gaussian codebook, constructed by truncating a Gaussian codebook with variance σ^2 at a cutoff photon number N_S and then rescaling for normalization. The probability distribution for a truncated Gaussian codebook is

$$P_{\sigma,N_\mathrm{S}}(\alpha) = \frac{e^{-\frac{|\alpha|^2}{2\sigma^2}}}{2\pi\sigma^2(1-e^{N_\mathrm{S}/2\sigma^2})}\Theta(N_\mathrm{S}-|\alpha|^2), \tag{3.28}$$

where Θ is the Heaviside step function. This is a suitable codebook for our purposes because the truncation provides an upper energetical bound and the Gaussian shape allows a no-cloning threshold to be derived from the well-known theory for Gaussian codebooks.

Since we do not know the optimal cloning attack for the truncated Gaussian codebook, we instead determine a bound on its optimal cloning fidelity. This can be done by comparing the truncated Gaussian codebook $P_{\sigma,N_\mathrm{S}}(\alpha)$ with the Gaussian codebook $P_\sigma(\alpha)$, for which the optimal cloning fidelity is known. We first consider the cloning machine as an arbitrary Gaussian process $\mathcal{N}$, and write the average cloning fidelity

$$\bar{F}(\mathcal{N}) = \int F(\mathcal{N},\alpha)P_{\sigma,N_\mathrm{S}}(\alpha)d^2\alpha. \tag{3.29}$$

We then have

$$\begin{aligned}\bar{F}(\mathcal{N}) &= \int F(\mathcal{N},\alpha)[P_{\sigma,N_\mathrm{S}}(\alpha)-P_\sigma(\alpha)]d^2\alpha + \int F(\mathcal{N},\alpha)P_\sigma(\alpha)d^2\alpha \\ &\leq ||P_{\sigma,N_\mathrm{S}}(\alpha)-P_\sigma(\alpha)||_1 + \bar{F}_\sigma(\mathcal{N}),\end{aligned} \tag{3.30}$$

where $||f(\alpha)||_1 = \int |f(\alpha)|d^2\alpha$ is the 1-norm and $\bar{F}_\sigma(\mathcal{N})$ is the average cloning fidelity with respect to $P_\sigma(\alpha)$. The optimal cloning fidelity is found by maximizing this quantity over $\mathcal{N}$ with

$$F_\mathrm{TG} = \max_{\mathcal{N}} \bar{F}(\mathcal{N}) \leq ||P_{\sigma,N_\mathrm{S}}(\alpha)-P_\sigma(\alpha)||_1 + F_\sigma, \tag{3.31}$$

where we use the known result $\max_{\mathcal{N}} \bar{F}_\sigma(\mathcal{N}) = F_\sigma$. We can calculate the 1-norm

$$||P_{\sigma,N_\mathrm{S}}(\alpha)-P_\sigma(\alpha)||_1 = 2\pi\int_0^\infty \left|\frac{\alpha e^{-\frac{|\alpha|^2}{2\sigma^2}}}{2\pi\sigma}\right| \left|\frac{\Theta(N_\mathrm{S}-|\alpha|^2)}{1-e^{-\frac{N_\mathrm{S}}{2\sigma^2}}}-1\right| d|\alpha| = 2e^{-\frac{N_\mathrm{S}}{2\sigma^2}}. \tag{3.32}$$

Thus, we find that an upper bound for the no-cloning threshold F_TG of a truncated Gaussian codebook is given by

$$F_\mathrm{TG} \leq \begin{cases} \frac{4\sigma^2+2}{6\sigma^2+1} + 2e^{-N_\mathrm{S}/2\sigma^2} & \sigma^2 \geq \frac{1}{2}+\frac{1}{\sqrt{2}} \\ \frac{1}{(3-2\sqrt{2})\sigma^2+1} + 2e^{-N_\mathrm{S}/2\sigma^2} & \sigma^2 \leq \frac{1}{2}+\frac{1}{\sqrt{2}}. \end{cases} \tag{3.33}$$

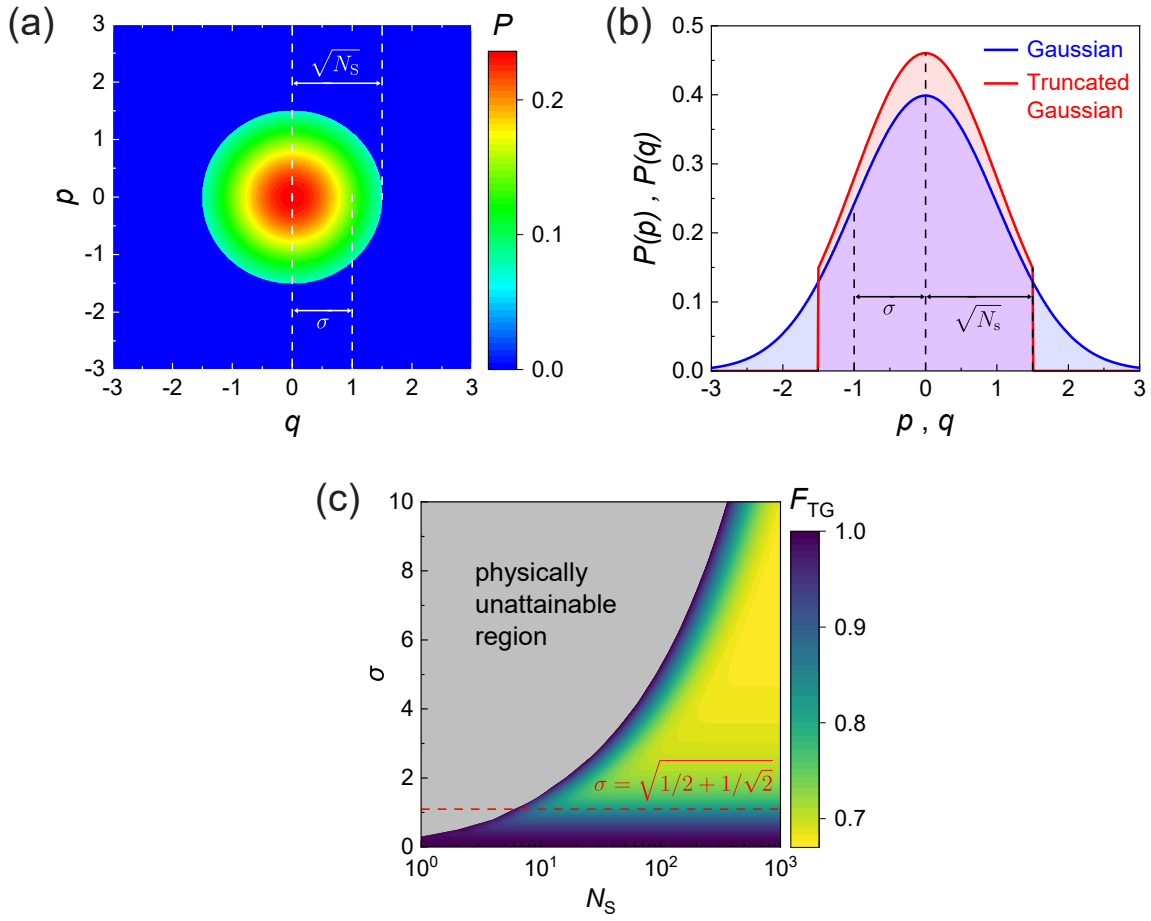

Figure 3.3: (a) Probability distribution function for a truncated Gaussian distribution with truncation limit $\sqrt{N_S}$, constructed from a Gaussian distribution with variance σ^2. (b) The truncated Gaussian codebook is constructed by truncating the a Gaussian codebook with variance σ^2 at a certain photon displacement N_S, and renormalizing the remaining region such that total probability remains 1. (c) Dependence of the no-cloning threshold for the truncated Gaussian codebook on truncation photon number N_S and distribution variance σ^2. The gray region represents $F_{TG} > 1$, where this upper bound for no-cloning fidelity is a physically unattainable value.

We see that this bound adds the deviation between the truncated Gaussian codebook and its corresponding Gaussian codebook to the exactly known no-cloning threshold for a Gaussian codebook. We note that comparing the truncated Gaussian codebook to a Gaussian codebook with the same variance σ^2 is optimal, because a different variance would cause additional deviations between the distributions. Fig. 3.3 shows F_{TG} as a function of σ^2 and N_S. The no-cloning bound approaches the optimal Gaussian case for $N_S \to \infty$ and $\sigma \ll N_S$. This is because the truncated Gaussian codebook approaches a Gaussian at large cutoff photon number and exponentially small error in its tail distribution. In the gray region of Fig. 3.3, we have $F_{TG} > 1$, implying that the upper bound F_{TG} for

no-cloning fidelity is a physically unattainable value. We remark that from a practical point of view, a truncated uniform codebook might be more convenient. Nevertheless, in this case, a sufficiently tight no-cloning threshold is hard to derive as it would require an accurate approximation of an arbitrary uniform distribution with a Gaussian, which is not possible in general.

3.3 Teleportation over thermal channels

For a realistic teleportation scenario, finite coupling to the ambient thermal environment must be considered. In this section, we examine the nature of thermal noise and calculate the influence of experimental imperfections in the communication channels. We present quantum teleportation as an error correction scheme for Gaussian imperfections. We also insert realistic experimental parameters to predict the performance of quantum teleportation.

3.3.1 Thermal noise

The analog quantum teleportation protocol transfers the quantum entanglement resource and classical feedforward as analog signals from Alice to Bob. In general, the channels that transport these analog signals can be affected by finite losses and temperatures. It is then important to determine how the teleportation protocol is influenced by these imperfections. For example, it is practically useful to consider quantum teleportation over long distance and at room temperature (RT) conditions, which consist of large losses and large thermal noise.

We consider the ambient thermal environment by coupling the thermal modes to our quantum system via a beam splitter model. The coupling strength is determined by the losses of the transport channels. This is procedure formally written as Eq. 3.17 and Eq. 3.18. The number of ambient thermal photons is given by the Planck distribution as in Eq. 2.19. At a frequency of 5 GHz, this photon number is 0.0083 at 50 mK and 208 at 297 K. We observe that quantum microwave signals, which are on the order of a few photons, are sensitive to thermal noise. While the ambient photon number is still negligible at 50 mK, the thermal noise becomes overwhelming when examining room temperature applications.

3.3.2 Imperfect entanglement distribution and feedforward channels

We consider analog CV quantum teleportation in the presence of realistic imperfections such as finite losses and interaction of the quantum system with a thermal bath. In particular, we investigate the influence of thermal noise in the analog feedforward as well as in the TMS distribution channel. In a realistic application scenario, these paths potentially pass a thermal environment, either via a cryogenic link or by free-space propagation.

In the first step, we consider power losses in the entanglement distribution channel ε_{ent} (denoted as ε_{13} in Fig. 3.2) and the feedforward channel ε_{ff} (denoted as ε_{14} in Fig. 3.2), which couple to an environmental bosonic bath with temperature T. Apart from these imperfections, we treat the quantum teleportation as lossless and noiseless. We find that in the limit of $G \gg 1$ and $\beta \ll 1$, the feedforward losses ε_{ff} simply act as a renormalization of the projection condition, which is then given by $G\beta(1-\varepsilon_{\text{ff}}) = 4$. Under the latter assumption, the fidelity for coherent state quantum teleportation can then be expressed as

$$F = \frac{2}{f(r, \varepsilon_{\text{ent}}, T_{\text{ent}}, \omega) + \beta\varepsilon_{\text{ff}} \coth\left(\frac{\hbar\omega}{2k_{\text{B}}T_{\text{ff}}}\right)}, \tag{3.34}$$

$$f(r, \varepsilon_{\text{ent}}, T_{\text{ent}}, \omega) = (2-\varepsilon_{\text{ent}})\cosh 2r - 2\sqrt{1-\varepsilon_{\text{ent}}}\sinh 2r + 2 + \varepsilon_{\text{ent}} \coth\left(\frac{\hbar\omega}{2k_{\text{B}}T_{\text{ent}}}\right), \tag{3.35}$$

where T_{ent} is the ambient temperature in the entanglement distribution channel and T_{ff} is the ambient temperature in the feedforward channel. We see from Eq. 3.35 that ε_{ent} introduces thermal noise from the channel environment and alters the interference mechanism of the teleportation protocol. Unlike the ε_{ff} term that is modulated by the coupling β, the influence of ε_{ent} cannot be suppressed. This implies that losses and noise in the entanglement distribution channel should be reduced as much as possible without alternative.

In the next step, we set $\varepsilon_{\text{ent}} = 0$ to investigate the influence of losses and noise in the feedforward channel. Under this assumption, we obtain the teleportation fidelity

$$F = \frac{2}{2 + 2e^{-2r} + \beta\varepsilon_{\text{ff}} \coth\left(\frac{\hbar\omega}{2k_{\text{B}}T_{\text{ff}}}\right)} = \frac{1}{1 + e^{-2r} + \beta\varepsilon_{\text{ff}} S(\omega, T_{\text{ff}})}, \tag{3.36}$$

where $S(\omega, T)$ is the coupled thermal noise power spectral density at mode frequency ω. In the limit of a perfect entanglement resource $r \to \infty$, we get

$$F = \frac{1}{1 + \beta\varepsilon_{\text{ff}} S(\omega, T_{\text{ff}})}. \tag{3.37}$$

We observe that we achieve resilience against thermal noise in the feedforward channel if we let $\beta\varepsilon_{\text{ff}} S(\omega, T) \to 0$, which is possible by making the coupling β sufficiently small. From an intuitive point of view, this result reflects that the feedforward signal is classical, for which an attenuating channel can be fully compensated by amplification. This property is also fulfilled for a digital feedforward, corresponding to strict $\beta = 0$ and $G \to \infty$. Nevertheless, Eq. 3.37 implies that for an analog feedforward signal, the asymptotically finite positive values of β and G eventually set an upper limit to the tolerable environmental temperature. In the high loss limit, $\varepsilon_{\text{ff}} \to 1$, fidelities beyond the classical limit of 1/2 can be reached

up to a maximal temperature

$$T_{\mathrm{c}} = \frac{\hbar\omega}{2k_{\mathrm{B}}\mathrm{arcoth}\,(2/\beta)} \simeq \frac{\hbar\omega}{k_{\mathrm{B}}\beta}. \tag{3.38}$$

Furthermore, Eq. 3.37 can be used to obtain the bath temperature T_{nc} corresponding to the no-cloning fidelity. In the case $F_{\mathrm{nc}} = 2/3$, we obtain $T_{\mathrm{nc}} \simeq T_{\mathrm{c}}/2$. For realistic experimental parameters $\beta = -15\,\mathrm{dB}$ and $\omega/2\pi = 5\,\mathrm{GHz}$, we find that $T_{\mathrm{c}} \simeq 7.6\,\mathrm{K}$. Thus, even in the high loss limit, it is possible to transmit the feedforward signal though a liquid Helium bath in a state of the art experiment. As can be seen in Eq. 3.38, the temperature T_{c} can be raised to arbitrarily high values by decreasing β. In practice, it is hard to reach this asymptotic value since reducing coupling $\beta \to 0$ requires a large gain $G \to \infty$, and we are eventually limited by compression effects. The technical challenge in this regard is the balance between maximizing degenerate gain G of the measurement JPAs and simultaneously minimizing noise from compression effects.

3.3.3 Teleportation as error correction

Fig. 3.4 shows the results from a simulation of our quantum teleportation protocol with losses and thermal noise only in the feedforward channel. Components apart from the feedforward channel are so far assumed to be noiseless. In Fig. 3.4(a), we choose experimentally attainable parameters of $\beta = -15\,\mathrm{dB}$ and $S = 6\,\mathrm{dB}$, where the feedforward gain is set to the optimal point, $G = 4/[\beta(1-\varepsilon_{\mathrm{ff}})]$, to compensate for the coupling β, the two hybrid rings in the detection setup, and the feedforward losses. Under these conditions, we observe that teleportation fidelity can exceed our previously derived truncated Gaussian no-cloning threshold, where we choose $N_{\mathrm{S}} = 100$, up to liquid helium ($4.2\,\mathrm{K}$) and liquid nitrogen ($77\,\mathrm{K}$) temperatures for sufficiently small feedforward losses. Even in the high loss limit, the no-cloning threshold can be surpassed for temperatures $\lesssim 1\,\mathrm{K}$, well achievable with conventional dilution refrigerators. Figure 3.4(b) shows the same simulation as Fig. 3.4(a), but for a smaller coupling, $\beta = -35\,\mathrm{dB}$. Indeed, the high-fidelity region is extended to significantly higher temperatures and feedforward losses, though the maximally achievable fidelity remains approximately the same. Finally, we increase the resource squeezing to $S = 20\,\mathrm{dB}$ in Fig. 3.4(c) and find that the overall fidelity increases. This is the case because higher squeezing implies that we increase the strength of the quantum correlations, responsible for destructive interference of the quantum noise at the directional coupler, in a more efficient way. We note that at a non-ideally chosen gain, $G \neq 4/[\beta(1-\varepsilon_{\mathrm{ff}})]$, higher squeezing level may actually decrease the fidelity because of imperfect interference effects. We observe that quantum teleportation implements an error correction scheme on the feedforward channel, as thermal noise $S(\omega, T_{\mathrm{ff}})$ can be suppressed by the coupling β and feedforward losses $\varepsilon_{\mathrm{ff}}$ can be fully compensated by the gain G. Note that in experimental implementations, a lower bound of β is determined by

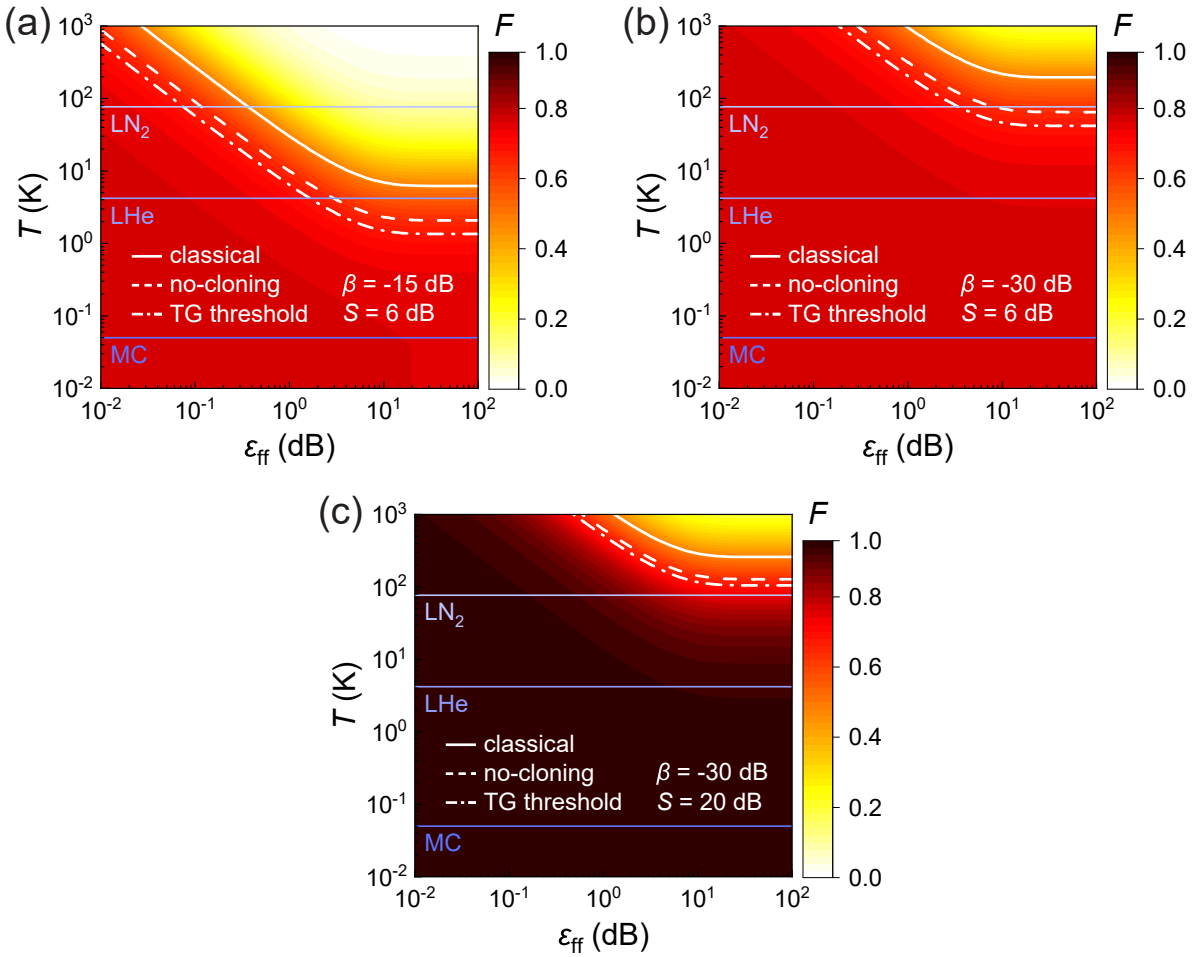

Figure 3.4: Teleportation fidelity as a function of feedforward temperature and loss. All other components in the teleportation protocol are assumed to have no noise and losses. Finite coupling and squeezing values are chosen, and gain is set to exactly compensate for coupling and feedforward attenuation. Solid lines represent the asymptotic classical limit of $F = 1/2$, dashed lines represent the asymptotic no-cloning limit of $F = 2/3$, and dash-dotted lines represent the truncated Gaussian no-cloning limit of F_{TG} when $N_{\mathrm{S}} = 100$. (a) Coupling of $-15\,\mathrm{dB}$ and squeezing of $6\,\mathrm{dB}$ gives intermediate fidelity values. (b) Reducing the coupling to $-30\,\mathrm{dB}$ extends the desired temperature and loss region. (c) Strengthening the squeezing to $20\,\mathrm{dB}$ increases the overall fidelity values.

the maximally achievable measurement gain G, and the maximum resource squeezing is determined by the quantum efficiency of the phase-sensitive amplifiers that generate the TMS state.

The previous results indicate that the asymptotic robustness of analog CV quantum teleportation crucially depends on minimizing the coupling β. However, Eq. 3.37 and Eq. 3.38 are derived under the idealistic assumption that the projection condition is exactly fulfilled and that we use noiseless cryogenic microwave components. We generalize our analysis in the following by employing a realistic theory model that takes into account

experimental imperfections according to Fig. 3.2, which is evaluated in a method based on that in Ref. [14].

3.3.4 Realistic teleportation with experimental imperfections

Except for the feedforward channel, we have so far considered the quantum teleportation setup as ideal. However, the passive components as well as the amplifiers also contribute to losses and noise in a realistic experimental teleportation protocol. Most of these sources of noise cannot be suppressed by decreasing the coupling β because they mainly occur before the Bell measurement step or in the entanglement distribution setup. Thus, the teleportation protocol does not act as an error-correcting scheme for these imperfections. In this section, we include all of these imperfections and study their implications for teleportation fidelity. Our study about the impact of realistic imperfections in the analog CV quantum teleportation of coherent microwave states is based on the theory model developed in Ref. [14].

Figure 3.5(a) shows the teleportation fidelity for the realistic protocol as a function of $\varepsilon_{\mathrm{ff}}$ and ambient temperature T in the feedforward channel. In contrast to the ideal scenario in Fig. 3.4(a), we fix the gain to $G = 21\,\mathrm{dB}$, causing non-ideal projectivity. In practice, the feedforward losses are not exactly known and it is not possible to exactly meet the projection condition. The value of 21 dB is chosen according to the prediction from ideal theory and compensates for the 6 dB of loss due to the beam splitters in the detection setup and for the coupling $\beta = -15\,\mathrm{dB}$. We observe that fidelity as a function of feedforward noise behaves similarly as for the ideal case in Fig. 3.4(a), but with overall lower values. As expected, the feedforward channel is robust against noise, since fidelities with quantum advantage can still be attained at 7 dB losses and up to liquid helium temperatures, which is already much higher than operating temperatures of 50 mK inside dilution refrigerators. Note that we do not observe the asymptotic robustness in the high loss limit $\varepsilon_{\mathrm{ff}} \to 1$ as seen in the idealistic scenario of Fig. 3.4(a). This is due to the fact that we set the feedforward gain to a constant, hence it cannot compensate for varying feedforward losses.

In order to suppress feedforward noise with a sufficiently weak coupling β, the gain G needs to be increased to compensate for the total attenuation in the feedforward channel. In the ideal protocol, this fact is reflected by the projection condition. The situation becomes more subtle in the realistic case. The fidelity dependence on β and G is shown in Figure 3.5(b) for a feedforward loss of $\varepsilon_{\mathrm{ff}} = 0.5\,\mathrm{dB}$ and squeezing $S = 6\,\mathrm{dB}$. We observe that, also in the realistic scenario, the fidelity maxima are close to the projection criterion $G\beta(1 - \varepsilon_{\mathrm{ff}}) = 4$. The linear relationship is especially evident in the limit of $G \gg 1$, but there is asymmetry in the low gain regime, which is a result from noise and loss in the experimental setup.

By using sufficiently weak coupling, analog CV quantum teleportation becomes robust

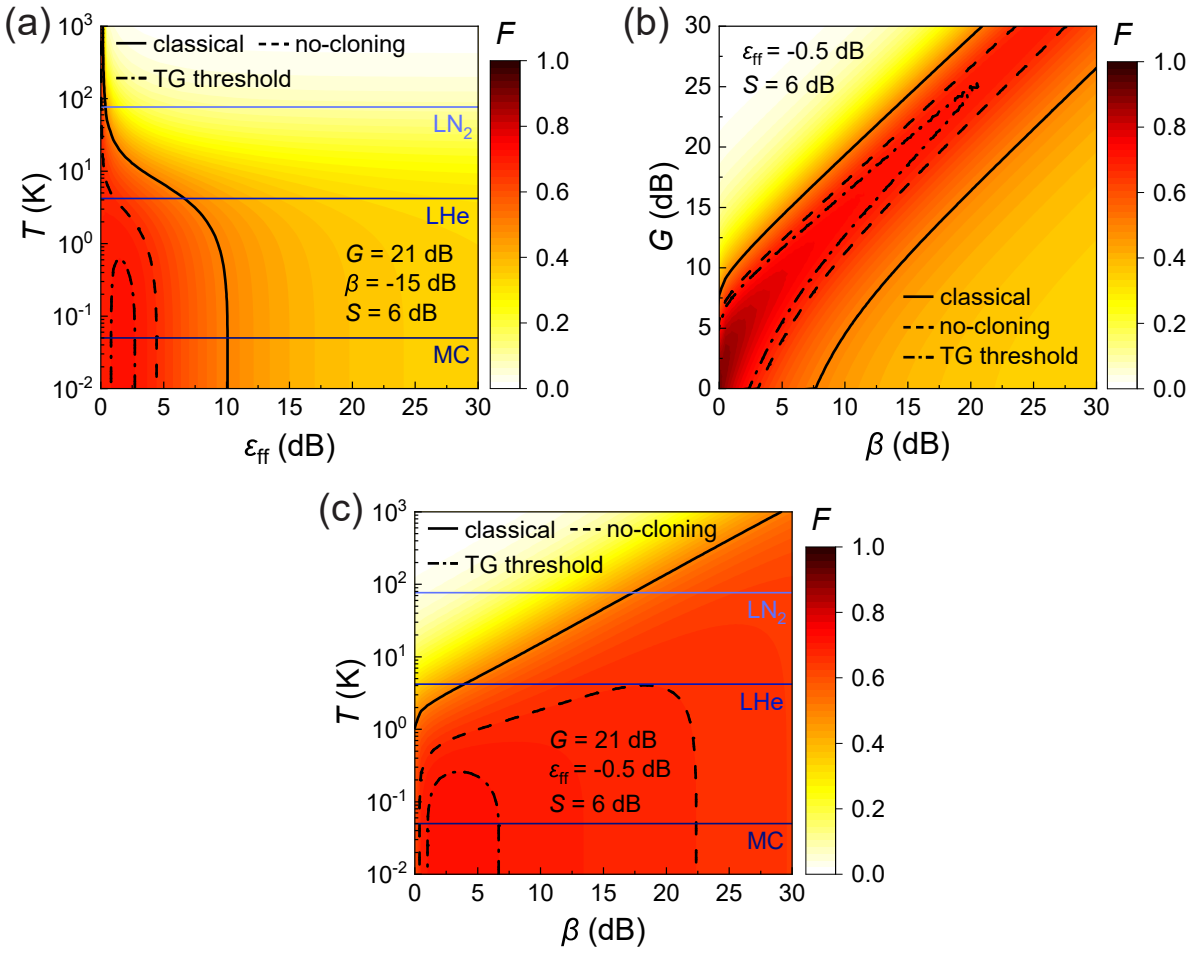

Figure 3.5: Teleportation fidelity as a function of various parameters. All experimental noise and losses are considered. Solid lines represent the asymptotic classical limit of $F = 1/2$, dashed lines represent the asymptotic no-cloning limit of $F = 2/3$, and dash-dotted lines represent the truncated Gaussian no-cloning limit of F_{TG} when $N_{\mathrm{S}} = 100$. (a) Dependence on feedforward temperature and loss $\varepsilon_{\mathrm{ff}}$. Fidelity maintains quantum advantage at 7 dB losses up to liquid helium temperatures. (b) Dependence on gain and coupling β. Fidelity maxima are close to the projection criterion and converge onto the projection criterion as squeezing S increases. (c) Dependence on temperature and coupling β. Fidelity maintains quantum advantage up to room temperature at $\beta = -30$ dB.

against arbitrary feedforward noise. In agreement with our analytical calculations in Eq. 3.37, Fig. 3.5(c) shows that teleportation fidelities attain a quantum advantage up to room temperature at coupling $\beta = -30$ dB. Although the effective value of β can in principle be arbitrarily reduced by adding a sufficiently large cold attenuation to the coupled port [49], the crucial constraint for implementing this weak coupling limit is the maximally achievable gain and compression of cold amplifiers. As an example, Josephson parametric amplifiers can reach up to 50 dB degenerate gain but eventually decrease the overall state purity due to gain-dependent noise [61]. Even though chaining multiple cold amplifiers

might lead to a reduction of the amplification noise, the overall performance is limited by the quantum efficiency of the Bell measurement, according to the Friis formula.

Chapter 4

Experimental techniques

In this chapter, we present the experimental methods and techniques used to generate and measure quantum microwave states. This requires advanced cryogenic and room temperature setups, in combination with various signal reconstruction methods. In particular, we focus on the techniques and characterization measurements that are relevant for implementing the quantum teleportation protocol in this work. For our experiments, we use a setup similar to Ref. [62]. In Section 4.1, we describe the cryogenic components of our experimental setup, which include the cryostat and microwave components. In Section 4.2, we explain the data acquisition process in our quantum teleportation experiment, which include the room temperature setup, the PID temperature control, and the reference state reconstruction. In Section 4.3, we describe the JPA parameter measurements that include finding a suitable JPA working point, determining the JPA degenerate gain, and balancing the two-mode squeezed state.

4.1 Cryogenic setup

The cryogenic setup is crucial for this work, since temperatures of around 50 mK are required to successfully generate quantum microwave states. In this section, we describe the experimental devices used in our cryogenic setup. The main instrument is a dilution cryostat that maintains the low temperatures needed in our experiment. We also detail the main cryogenic microwave components used to generate and control our quantum microwave states.

4.1.1 Cryostat

Dilution cryostat are used to maintain the cryogenic environment needed for our experiments. We use dry cryostats that hold high vacuum, which insulates the experimental setup from room temperature. Cooling units in the cryostat then generate the cooling power needed to lower the temperature of inner stages to their desired levels. The experimental setup is placed in the innermost and coldest stage of the cryostat. Control of the experimental setup is done through input and output lines that run through the cryostat.

Dilution refrigerator

The dilution refrigerators used in this experiment consist of five stages, namely pulse tube 1 (PT1) stage, pulse tube 2 (PT2) stage, 1K stage, distillation (still) stage, and mixing chamber stage (MC). With the exception of the 1K stage, each of the mentioned stages are connected with cylindrical radiation shields that prevent radiation from other layers from reaching the inner setup. In addition, there is an outer vacuum (OVC) shield as the outermost layer of the cryostat which holds up to 10^{-6} mbar of high vacuum. This vacuum is especially important to minimize thermal coupling between respective layers.

The dilution refrigerator is designed such that the temperature becomes lower as we go down the stages. The approximate achievable temperatures for each stage are shown in Fig. 4.1(a). At the first two stages, a pulse tube refrigerator (PTR) is used to generate cooling power. The PTR is suitable for a cryostat since it does not have moving parts in the lower temperature part of the device. Furthermore, using a PTR allows the cryostat to remain "dry". Wet cryostats require the stages to be submerged in a liquid helium bath to maintain a temperature of 4.2 K. Current PTR cryocoolers can achieve around 50 K at the first PT1 stage, and around 4 K at the second PT2 stage.

Below the PTR is the 1K stage, which has a temperature of around 1.2 K. This temperature can be achieved in different ways. Rather directly, it can be achieved by evaporative cooling of liquid helium from a 1K pot. Another method is by using a Joule-Thomson cooler, which exploits the Joule-Thomson effect whereby real gases cool upon expansion when throttled through an orifice.

The lowest temperatures in the cryostat is achieved by dilution cooling, which exploits evaporative cooling between the concentrated and dilute phases of helium-3/helium-4 mixture. At low temperatures, the concentrated phase contains almost 100% helium-3, while the dilute phase contains about 6.6% helium-3. In the mixing chamber, these two phases are in equilibrium and separated by a phase boundary. A turbomolecular pump in the distillation chamber removes helium-3 from the dilute phase, causing helium-3 from the concentrated phase to cross the phase boundary into the dilute phase. Since this process is endothermic, heat is removed from the mixing chamber stage. This cooling results in a temperature of below 50 mK at the mixing chamber stage.

In our experiment, we use one home-made dry dilution refrigerator from the Walther-Meißner-Institute and one commercial dry dilution refrigerator Triton from Oxford Instruments. More details about the operating principles of dilution refrigerators can be found in Ref. [63].

Sample stage

The sample stage is attached to the mixing chamber stage and holds the experiment setup. Being thermalized to the mixing chamber stage, the sample stage also has a base temperature below 50 mK. Fig. 4.1(b) shows the sample stage in the Alice cryostat of

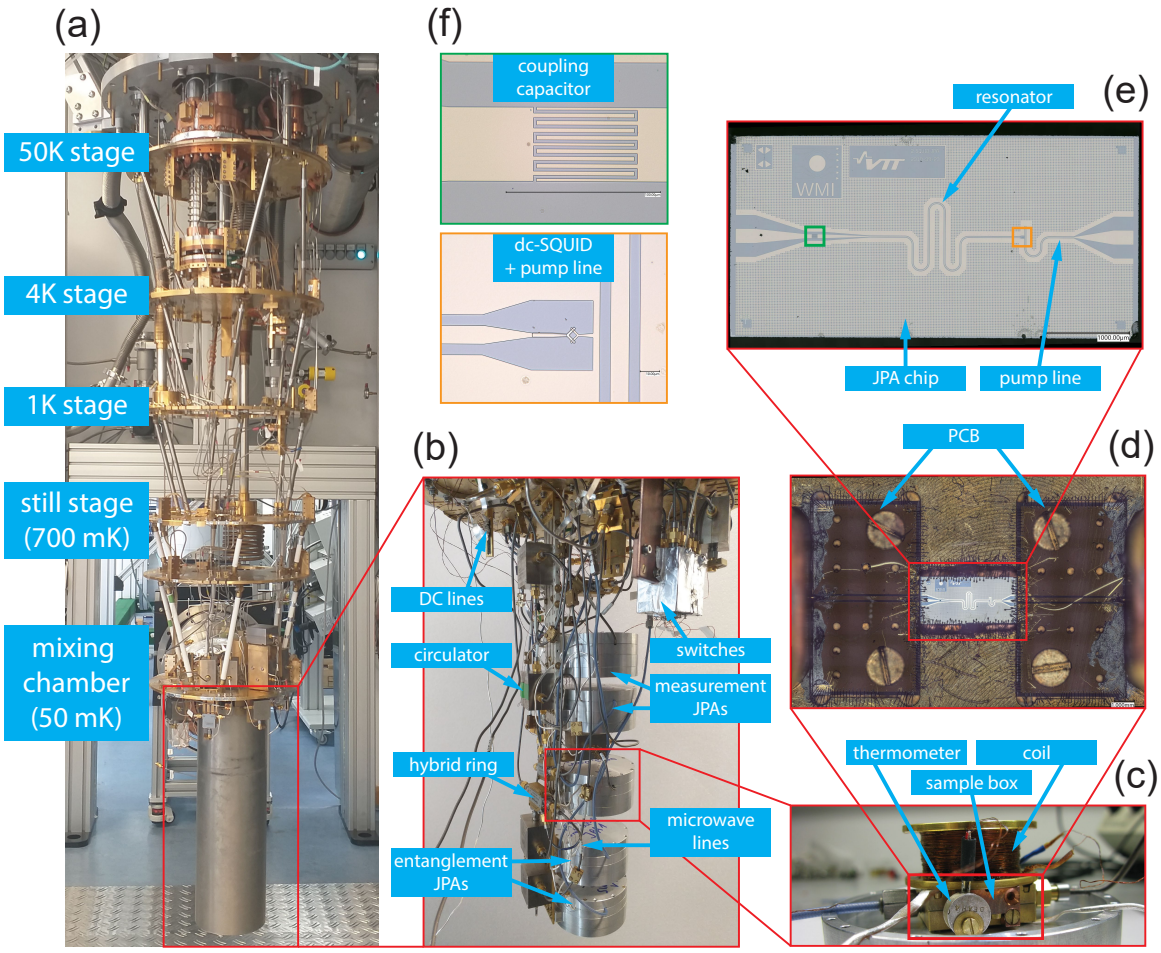

Figure 4.1: (a) Photograph of Alice dilution refrigerator with respective temperature stages. (b) Photograph of Alice sample stage with cryogenic devices. (c) Photograph of JPA sample box and superconducting coil. (d) Photograph of a JPA sample holder with a JPA installed. (e) Photograph of a JPA chip. (f) Photograph of the coupling capacitor and DC-SQUID inside a JPA.

our experiment. The quantum resources for our experiments are generated at the sample stage. The microwave components used are detailed in Section 4.1.2. Due to the unique setup of our quantum teleportation experiment, which connects two separate dilution refrigerators, the two sample stages in the cryostats are actually connected by a cryogenic link. The setup of the cryogenic link is described in Chapter 5. It is important to consider that the microwave components on the sample stage are controlled via lines that extend to the RT devices. Signals from the input lines and operation of the devices cause heating, which can raise the sample stage temperature during experiment.

Input and output lines

Input lines are used to apply signals to the experimental setup and output lines are used to measure the results of the experiment. It is important to consider these lines so that the desired quantum states can be created and that the results can be properly measured.

The input states are first generated at room temperature by a vector network analyzer (VNA) or microwave source. The signals are fed into the cryostat using flexible microwave lines, since they are more convenient to position and losses are not crucial for classical microwave signals. Inside the cryostat, stainless steel microwave coaxial cables (SC-219/50-SS-SS, Coax Co., Ltd) are used until the 4K stage. This is because stainless steel cables provide good thermal isolation between the temperature stages, though have significant losses of 5.9 dB/m at 5.0 GHz frequency and 4 K temperature. NbTi microwave coaxial cables (SC-219/50-NbTi-NbTi, Coax Co., Ltd) are used until the sample stage. This is because, below the critical temperature of NbTi (around 9.7 K), the cables become superconducting and the losses are less than 0.3 dB/m.

Furthermore, at each temperature stage in the cryostat, attenuators are inserted to the input lines such that the thermal radiation from room temperature is attenuated. To achieve a good signal-to-noise ratio at room temperature, a -55 dBm signal is generated with room-temperature Johnson-Nyquist noise. This Johnson-Nyquist noise is then attenuated at each stage to match the ambient temperature. As a result, the signal-to-noise ratio remains constant until the sample stage, and heat load is optimally distributed among the different cryostat stages. This procedure is important for our experiments, since we want quantum signals at the single photon level and otherwise the quantum states would be covered by noise.

The lines used for output are similar as the input, with superconducting cables (SC-219/50-NbTi-NbTi, Coax Co., Ltd) below the 4K stage and normal-conducting cables (SC-219/50-SSS-SS, Coax Co., Ltd) above the 4K stage. In contrast to the input, the output lines do not require attenuators because the thermal noise at the sample stage is already much lower than the upper stages. Instead, the output lines require chained amplifiers, so that the weak quantum signals can be detected by room temperature electronics. For this purpose, we use cryogenic high-electron-mobility transistor (HEMT) amplifiers (LNF-LNC4_8A, Low Noise Factory) and RT amplifiers (AMT-A0033, Agile MwT). We note that the HEMT is the dominant noise source in the output line. We also insert circulators (CTH1184-KS18, Quinstar and RADC-4-8-Cryo, Raditek) between stages, so that signals can propagate from the lower temperature stages to the higher temperature stages, but noise propagating in the opposite direction is suppressed. Finally, the output signals are transmitted into a VNA or a field programmable gate array (FPGA) for readout. The RT devices are described with more detail in Section 4.2.1.

4.1.2 Cryogenic microwave components

Cryogenic microwave components, including JPAs, microwave cables, and couplers, are needed to accomplish quantum optical experiments in the microwave regime. Since the energy scale of microwave photons is much lower than that of optical photons, these microwave devices must operate with low noise and at cryogenic temperatures. We describe here some of the main microwave components, which are shown in Fig. 4.1(b-d).

Perhaps the most important component in our experimental setup is the Josephson parametric amplifier, which is used to squeeze vacuum states and to perform the Bell-type measurement. For our experiments, we use JPA chips designed and fabricated at NEC Smart Energy Research Laboratories Japan and RIKEN, Japan. The resonator and pump lines of the JPA are written into a 50-nm thick Nb film and then deposited onto a 300-μm thick silicon substrate. The DC-SQUID is fabricated by using aluminum shadow evaporation. We also use JPA chips from VTT Technical Research Centre of Finland. The VTT design coincides with that of NEC, with the difference that a 525-μm chip is used and the DC-SQUIDs are fabricated from niobium. We prepare the JPA chip by gluing it into a copper sample box and then galvanically coupling it to the box ground via aluminum bonds. The sample box allows the JPA to be connected to the microwave signal and pump lines. Then, a large coil made from superconducting wire (C510/NbTi, Supercon) is place on top of the sample box. This coil is used to generate the magnetic field for choosing the flux point of the JPA. Temperature sensors and heaters are also attached to the sample box to monitor the JPA temperature and implement PID temperature control. Finally, the entire configuration is mounted into an aluminum box, which protects the JPA from outside magnetic fields and confines the coil magnetic field inside the box. The sample JPA and its circuit components are shown in Fig. 4.1(d-f).

Another important component is the microwave cable used to carry the microwave signals between devices. For our experiment, we use stainless steel and NbTi coaxial cables manufactured by Coax Co., Ltd. In order to adapt the cables into our experiment setup, we manually cut and bend the cables. It is important to ensure that the cables maintain the 50 Ω impedance matching with the other microwave components, otherwise significant reflection may occur as signals enter the cable. We typically have an impedance mismatch of ± 2 Ω and can check for this mismatch using a time-domain reflectometer (TDR).

Other components used to manipulate the quantum microwave signals include circulators, hybrid ring couplers, and directional couplers. Circulators (CTH1184-KS18, Quinstar and RADC-4-8-Cryo, Raditek) are nonreciprocal devices that contain ferromagnets to break time-reversal symmetry, making the transmission dependent on the respective direction. This allows the microwave signal to travel in the desired direction, while suppressing the effects of reflection and back-propagating noise. Hybrid ring couplers (CPL-5850-100B, Miteq) are four-port microwave devices that act analogously to a beamsplitter. This is used for the entanglement sharing and Bell-type measurement in our experiment.

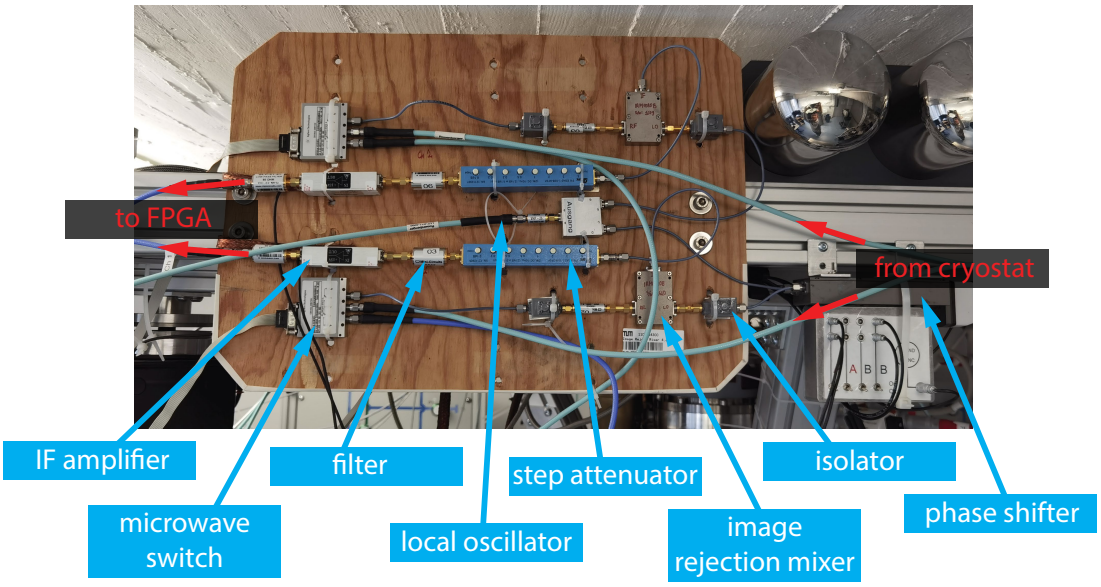

Figure 4.2: Photograph of the room temperature dual-path receiver.

Directional couplers (CPL-4000-8000-15-C, Sirius Microwave) are devices that realize highly asymmetric beam splitter operations. This is used for the state displacement in our experiment.

4.2 Data acquisition

Proper data acquisition is crucial to accurately perform tomography of quantum microwave states. In this section, we describe our setup and methods for data acquisition. We first describe the main components of our room temperature setup. We also briefly discuss the PID control loop used to stabilize the experiment temperature. We then explain the reference state reconstruction method, which is used to reconstruct quantum states from measurement readings.

4.2.1 Room temperature setup

In our experiment, the bulk of the data acquisition process happens in the room temperature setup. The microwave signals are generated at room temperature, with pump signals being high-pass filtered (VHF-8400+, Mini-Circuits) above 9 GHz, before entering cryostat. The output signals are received and measured by the room temperature setup. Fig. 4.2 shows the dual-path receiver used in our setup. One procedure for data acquisition is using a vector network analyzer (VNA), which is especially useful for testing and characterizing

the experimental setup. Another procedure for data acquisition is by generating a input microwave signals and measuring the output signal moments with a field-programmable gate array (FPGA).

Vector network analyzer

Vector network analyzers are instruments that measure the network parameters of electrical networks. It sends a signal through one port and measures this signal as it returns at another port. We can measure the S-parameters to observe the reflection and transmission of this signal through our experiment system. For our experiment, we use the Rohde & Schwarz ZVA24 vector network analyzer for calibration purposes. For instance, we can characterize the flux response of our JPAs by measuring the phase shift induced at different frequencies. Also, we can characterize the compression point of our JPAs by measuring the maximum gain produced at different input powers. More details about these parameter measurements are discussed in Section 4.3. Furthermore, we can use the VNA to check for problems in the experiment setup. For example, defects in a microwave line would show up as anomalous attentions on the VNA measurement.

Microwave sources

Microwave sources can be used to generate signals at the desired frequency and phase. For our experiment, we use the Rhode & Schwarz SGS100A SGMA RF Source, which has an output frequency up to 12.75 GHz and output power up to 25 dBm. This frequency range is sufficient for our signal frequency of 5-6 GHz and hence pump frequency of 10-12 GHz. The allowed power range is also useful to compensate for setup losses. Since we utilize several microwave sources, they are synchronized with a 10 MHz reference source in a cascaded manner. When making measurements, we want to compare different experimental configurations, such as when the Bell measurement JPAs are not pumped and when they are pumped. We do this measurement by letting the microwave sources output signals in a pulsed sequence, so that each pulse takes a different configuration, which is implemented using a data timing generator (DTG).

Field-programmable gate array

Field-programmable gate arrays can be used to digitize the input signals. For our experiment, we use the a National Instruments PXIe-7975R FPGA for data processing and a National Instruments NI-5782 transceiver module as an analog-to-digital converter (ADC), and operate the signal at a sampling rate of $f_S = 125$ MHz. Since the signal frequency f_{RF} lies around 5-6 GHz, which is much higher than f_S, we downconvert to an intermediate frequency $f_{IF} = 11$ MHz. This is done by mixing a strong local oscillator (LO) signal at frequency $f_{RF} + f_{IF}$ with the incoming signals via an image rejection mixer (IRM4080B, Polyphase). We choose $f_{IF} = 11$ MHz to avoid interference with the 10 MHz

reference source. After downconverting, we can adjust the signal amplitude with step attenuators (ESA2-1-10/8-SFSF, EPX microwave Inc.), which is used to balance the two signal paths and avoid compression effects. We also adjust the relative phase difference between the two signal paths to 180° using a manual phase shifter. The signal then goes through a band-pass filter (SBP-10.7+, Mini-Circuits) with bandwidth 9.5-11.5 MHz, and further amplified by IF-amplifiers (AU-1447-R, Miteq). Finally, the signal goes through a low-pass filter and a DC block before being sent to the analog-to-digital converters in the FPGA.

4.2.2 PID temperature control

A proportional-integral-derivative (PID) controller is a control loop mechanism that uses feedback to continuously control a system. The PID controller continuously calculates an error value as the difference between the desired setpoint and the current measured value, and applies a correction based on its proportional, integral, and derivative parameters. For our experiment, PID control is employed to stabilize the temperatures of various devices in our setup. We accomplish this by using rubidium oxide temperature sensors to monitor the current value and using resistance heaters to apply corrections. On the Alice cryostat, we can measure up to 16 temperature lines with a resistance bridge (Model 370, LakeShore) in the four-wire measurement scheme. Furthermore, two temperature lines can be used as PID controllers by employing two additional resistance bridges (AVS-47B, Picowatt) and two temperature controllers (TS-530A, Picowatt). On the Bob cryostat, we set up a resistance bridge (AVS-48SI, Picowatt) in the four-wire scheme for temperature measurement and PID control. Additionally, a PID controller to set mixing chamber temperature is integrated in the commercial software provided with Bob.

4.2.3 Quantum state reconstruction

Several methods can be used to reconstruct quantum microwave states. One possibility is to use single photon detectors a cryogenic temperatures [64, 65], but they are limit in their usability to detect quantum microwaves due various drawbacks such as high dark count rates and long reset times. Alternatively, the weak quantum signals can be linearly amplified and measured at room temperature with heterodyne detection [66]. In realistic scenarios, the best available commercial HEMT amplifiers add around 6-7 noise photons at 5 GHz, which cover the quantum signals with noise. In order to reconstruct quantum states with such significant noise contribution, we use the reference state reconstruction method, which we introduce in the following.

Photon number conversion factor

The photon number conversion factor (PNCF) is a method to calibrate amplification chains, such that we can convert the measured voltages at the FPGA to photon numbers at desired locations in our cryogenic setup. The photon number is calibrated by using a photon source that emits a known photon number as reference. In our experiment, we use a 30 dB attentuator as the photon source. The reason for this is because it approximates a black body radiator, where the emitted temperature-dependent power spectrum is white [67], while not attenuating input coherent signals too much. For our calibration measurements, we probe temperatures between 50 mK to 400 mK. Since we want to change the attenuator temperature without heating the mixing chamber, we establish weak thermal coupling of the attenuator to the cryostat. This is done by using stainless steel input cables and NbTi output cables. In addition, we use thin silver ribbons to thermally couple the heatable attenuator to the mixing chamber stage. This allows the attenuator to reach the 50 mK base temperature in reasonable time, without significantly heating the mixing chamber when attenuator is set to higher temperatures around 400 mK.

The detected power $P_{1,2}$ of the amplification chain at the FPGA is given by [67, 68]

$$P_{1,2} = \frac{\langle I_{1,2}^2 \rangle + \langle Q_{1,2}^2 \rangle}{R} = \frac{\kappa_{1,2}}{R} \left[\frac{1}{2} \coth \left(\frac{h f_0}{2 k_\mathrm{B} T_\mathrm{att}} + n_{1,2} \right) \right], \tag{4.1}$$

where $\langle I_{1,2}^2 \rangle, \langle Q_{1,2}^2 \rangle$ are the second order quadrature moments, $R = 50\ \Omega$, h is the Planck constant, k_B is the Boltzmann constant, f_0 is the center frequency of detection bandwidth, and T_att is the attenuator temperature. The subscripts $1, 2$ denote the two signal paths. The photon number conversion factor (PNCF) is defined as $\kappa = G_{1,2} \cdot R \cdot BW \cdot h f_0$, where BW is the full detection bandwidth. Additionally, $G_{1,2}$ is the amplification gain and $n_{1,2}$ is the amplification noise of the amplification chains. From Eq. 4.1, we see that changing the attenuator temperature T_att leads to different photon numbers and hence different measured powers. We can then extract $\kappa_{1,2}$ and $n_{1,2}$ by fitting the data from T_att and $P_{1,2}$ measurements. In Fig. 4.3, we show a PNCF calibration measurement at $f_0 = 5.6$ GHz. The fitting results give $\kappa_1 = 1.79 \pm 0.12 \times 10^{-8}\ \mathrm{V}^2$ and $\kappa_2 = 1.80 \pm 0.12 \times 10^{-8}\ \mathrm{V}^2$, which are similar due to balancing of the amplification chains. However, we have that $n_1 = 20.4 \pm 1.4$ and $n_2 = 99.3 \pm 6.6$. The much higher thermal noise in path 2 might be due to a noisy HEMT amplifier or problematic thermalization.

Reference state reconstruction

In reference state reconstruction, a known signal is used as a reference state to calibrate the effects of the amplification chain [69, 70]. In our experiments, we use choose the reference state to be a weak thermal state with about 0.01 photons at 5 GHz at 50 mK, which is well approximated by the vacuum state.

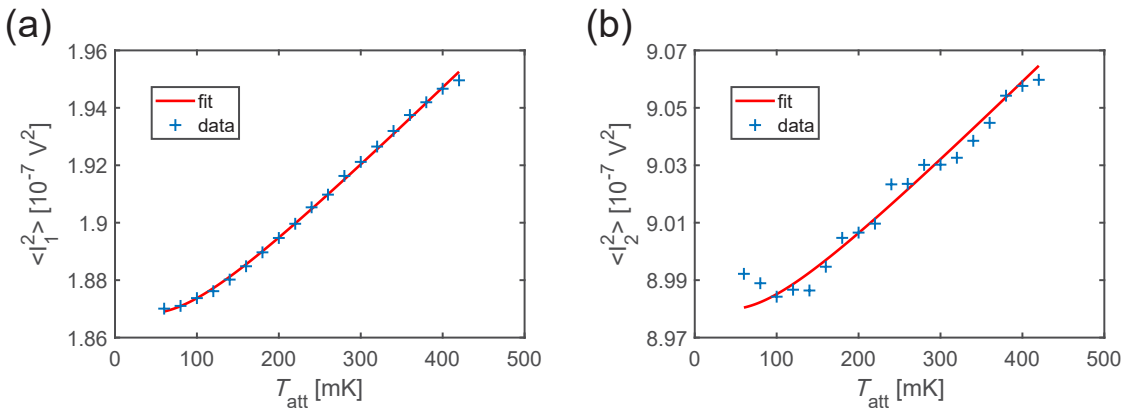

Figure 4.3: Photon number conversion factor (PNCF) calibration for path 1 (a) and path 2 (b). Markers represent measured data and the solid lines are fits according to Eq. 4.1. This calibration is obtained for the working point $f_0 = 5.6$ GHz.

We use the reference state reconstruction method to reconstruct the signal moments of the quantum state. The quadrature moments $\langle \hat{I}_1^n \hat{I}_2^m \hat{Q}_1^k \hat{Q}_2^l \rangle$ are related to the complex envelope functions by

$$\hat{\xi}_{1,2} = \frac{\hat{I}_{1,2} + i\hat{Q}_{1,2}}{\sqrt{\kappa}}. \tag{4.2}$$

This allows the complex envelope function moments $\langle (\hat{\xi}_1^\dagger)^n (\hat{\xi}_2^\dagger)^m \hat{\xi}_1^k \hat{\xi}_2^l \rangle$ to be computed from the quadrature moments. For the quantum states, the complex envelope functions can be written as

$$\hat{\xi}_{1,2} = \hat{a}_{1,2} + \hat{V}_{1,2}, \tag{4.3}$$

where $\hat{a}_{1,2}$ is the annihilation operator of the quantum signal and $\hat{V}_{1,2}$ is the added noise of the respective path. For the reference state, the complex envelope functions can be written as

$$\hat{\xi}_{\mathrm{ref};1,2} = \hat{v}_{1,2} + \hat{V}_{1,2}, \tag{4.4}$$

where $\hat{v}$ describes the weak thermal reference state. The reference state reconstruction computation is as follows. First we use Eq. 4.4 to calculate the noise moments $\langle (\hat{V}_1^\dagger)^n (\hat{V}_2^\dagger)^m \hat{V}_1^k \hat{V}_2^l \rangle$ from the known reference state moments $\langle (\hat{v}_1^\dagger)^n (\hat{v}_2^\dagger)^m \hat{v}_1^k \hat{v}_2^l \rangle$ and the complex envelope moments $\langle (\hat{\xi}_{\mathrm{ref};1}^\dagger)^n (\hat{\xi}_{\mathrm{ref};2}^\dagger)^m \hat{\xi}_{\mathrm{ref};1}^k \hat{\xi}_{\mathrm{ref};2}^l \rangle$. Then we use Eq. 4.3 to calculate the signal moments $\langle (\hat{a}_1^\dagger)^n (\hat{a}_2^\dagger)^m \hat{a}_1^k \hat{a}_2^l \rangle$ from the obtained noise moments $\langle (\hat{V}_1^\dagger)^n (\hat{V}_2^\dagger)^m \hat{V}_1^k \hat{V}_2^l \rangle$ and the complex envelope moments $\langle (\hat{\xi}_1^\dagger)^n (\hat{\xi}_2^\dagger)^m \hat{\xi}_1^k \hat{\xi}_2^l \rangle$. The complex envelope moments can be obtained from the measured quadrature moments by Eq. 4.2.

Reconstruction point

The reference state reconstruction method as given above reconstructs the quantum states at the noise source, namely the 30 dB attenuator. However, we often want to reconstruct quantum states at different positions in the experimental setup. For this purpose, we must carefully estimate the losses from the heatable attenuator to the desired reconstruction point. These losses affect the PNCF factors $\kappa_{1,2}$, which are needed for accurate reference state reconstruction. Given that there is L dB of losses between the heatable attenuator and the desired reconstruction point, the amplification chain gains are related by

$$G_{\mathrm{att};1,2} = G_{\mathrm{r};1,2} \cdot 10^{-L/10}, \tag{4.5}$$

where G_{att} is the gain referenced at the attenuator and G_{r} is the gain referenced at the reconstruction point. The PNCF factors are then related by

$$\kappa_{\mathrm{att};1,2} = \kappa_{\mathrm{r};1,2} \cdot 10^{-L/10}. \tag{4.6}$$

4.3 JPA parameter measurements

The JPA is used extensively throughout our experiments. Thus, it is important to characterize the properties of the JPAs used. In this section, we present the measurements to characterize and optimize the performance of our JPAs. First, we probe the DC-flux response of the JPA resonance frequency and use it to choose a suitable working point. Then, we measure the JPA nondegenerate gain and determine its 1 dB compression point. Finally, we characterize the performance of squeezing and entanglement generation, and balance the generated TMS state.

4.3.1 DC-flux tuning and nondegenerate gain

As explained in Section 2.2, the resonance frequency of a JPA can be tuned by generating a DC magnetic flux through the DC-SQUID loop. We experimentally apply this magnetic flux with a superconducting coil placed on top of the JPA sample box, as described in Section 4.1.2. In order to achieve parametric amplification with a JPA, we need to find a working regime of frequency and power for the microwave pump tone. For instance, a JPA with resonance frequency f_0, needs to be pumped with frequency $2f_0$. If we set a desired working frequency, then we need to perform calibration measurements on the JPA to determine suitable flux point and pump powers. We utilize a VNA to complete these calibration measurements. We send coherent input microwave signals to the JPA from channel 2 and receive output signals at channel 1, which we measure with the S_{12}-parameter on the VNA.

For a calibration of the JPA flux dependence, we sweep both the frequency of input sig-

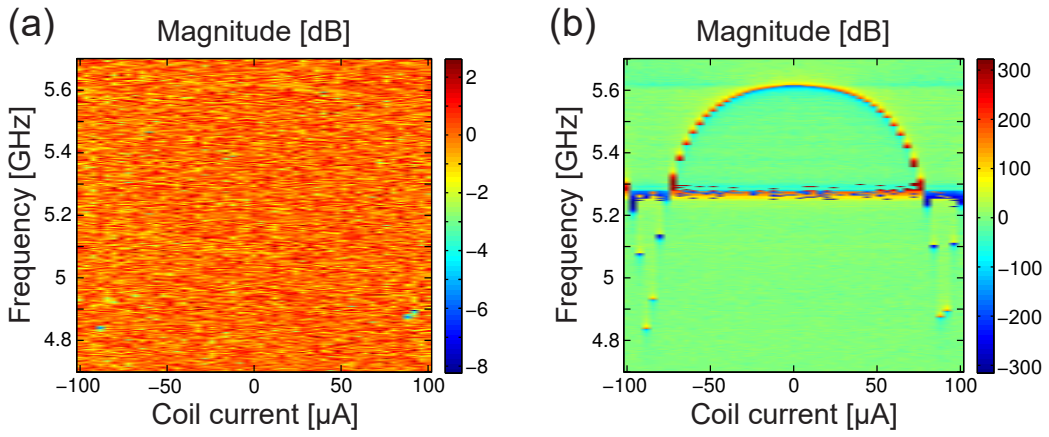

Figure 4.4: JPA resonance frequency as a function of applied magnetic flux. (a) Magnitude response on the probe signal. (b) Phase response on the probe signal.

nals and the DC current through the superconducting coil. Fig. 4.4 shows a measurement result for this calibration. We use a frequency span of $\Delta f = 1$ GHz and a coil current span of $\Delta I = 200$ μA. We see that the signal amplitude and phase response changes depending on the frequency and coil current. Fig. 4.4 actually shows processed data to have better clarity. For the amplitude response, an averaged background amplitude is subtracted from the measured data. For the phase response, a linear phase increase due to the unwrapped phase measurement is subtracted from the measured data. We see that indeed changing the coil current shifts the resonance frequency of the JPA. In the magnitude response, we observe the expected small attenuation due to internal losses of the JPA. In the phase response, we observe the expected 360° phase shift due to crossing the JPA resonance frequency, which verifies that the JPA is overcoupled $Q_{\text{int}} \gg Q_{\text{ext}}$. With this calibration result, we can choose a desired working frequency by tuning the coil current to the value that corresponds to its phase shift. Usually, a working point with an intermediate slope in the flux dependence is desired, because a small slope gives small amplification gain while a large slope creates large amplification noise.

For a calibration of the pump power dependence of the nondegenerate gain, we first set the coil current to the desired working point, and then sweep both the frequency of input signals and the pump power for the microwave pump tone. We note that this measures the nondegenerate gain of the JPA, where it is a phase insensitive amplifier. Fig 4.5 shows a measurement result for this calibration. We use a frequency span of $\Delta f = 80$ MHz and a pump power span of $\Delta P = 14$ dBm. We see an amplification of signal amplitude near the resonance frequency and is dependent on pump power. Fig. 4.5 actually shows processed data to show improved contrast, for which an averaged background amplitude is subtracted from the measured data. We observe the expected increase in amplification with increasing pump power, until a drop-off occurs due to entering the oscillator regime.

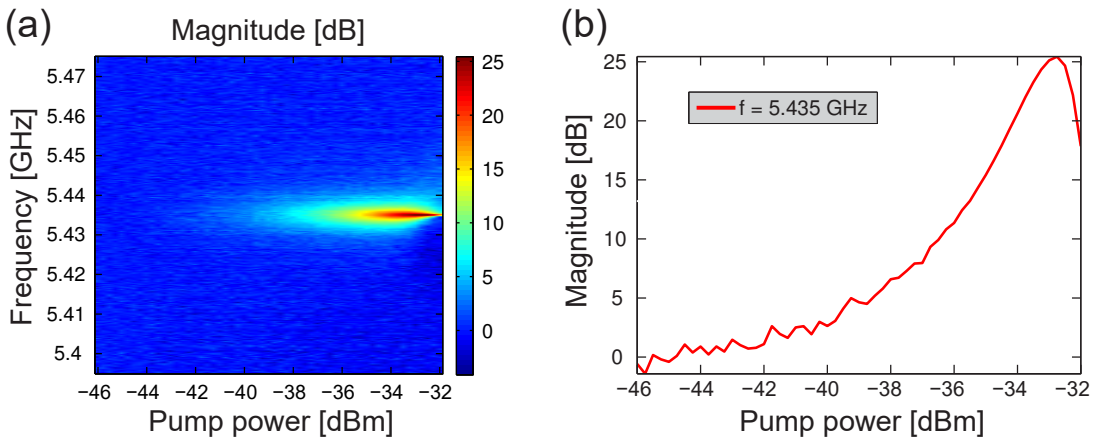

Figure 4.5: Nondegenerate gain as a function of the JPA pump power. (a) Magnitude response across different frequencies. (b) Magnitude response at the working point $f_0 = 5.435$ GHz. Pump powers are referenced to the pump port of the JPA sample holder.

With this calibration result, we can choose a desired gain by tuning the pump power to its corresponding value.

4.3.2 Degenerate gain and 1 dB compression point

In the degenerate gain regime, a JPA realizes a phase-sensitive amplifier. This is achieved when the pump frequency is twice the signal frequency, such that the idler mode is created at the same frequency as the amplified signal mode. This results in interference between the two modes, which can be constructive or destructive depending on their relative phase, and is controlled by the phase difference between the signal and the pump tone [71]. We utilize a microwave source and our FPGA setup to complete these calibration measurements. Since the signal source and pump source are synchronized, their phase difference can be controlled by a feedback loop that corrects for any phase mismatch between respective measurement sweeps.

For a calibration of the degenerate gain, we first choose a desired working point, and then sweep both the phase of input signals and the power of the pump tone. Fig 4.6 shows the result for this experiment. We use -11 to -1 dBm of pump power and cover 180° in phase since the behavior is 180°-periodic. We see that indeed changing the phase controls the interference behavior. We also observe the expected increase in maximum amplification with increasing pump power, until a drop-off occurs when the pump field exceeds the critical field in the model by Yamamoto *et al.* [46].

The 1 dB compression point is a figure of merit that denotes the power at which the signal power gain is 1 dB below the value expected for a linear device [18]. It characterizes the permitted input powers after which the signal gain starts to decrease due to nonlinearities of the JPA. For a calibration of the 1 dB compression point, we perform

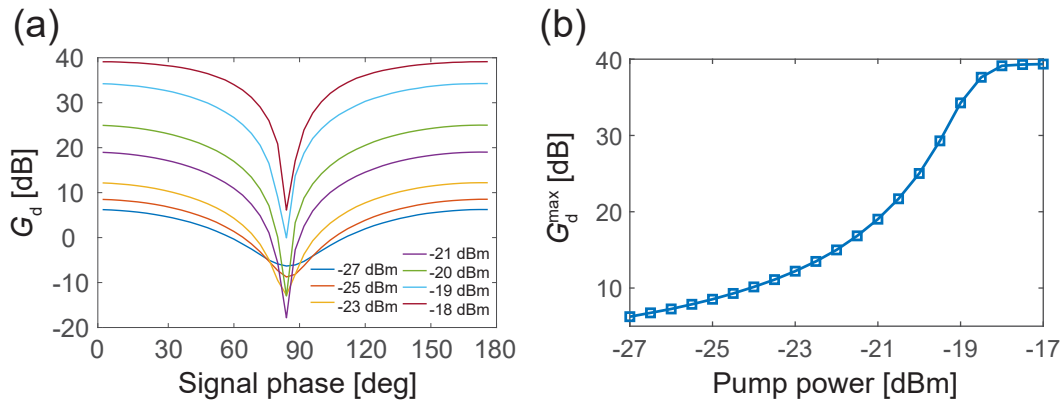

Figure 4.6: (a) Phase-dependent degenerate gain G_d for different values of pump power. (b) Maximum degenerate gain $G_\mathrm{d}^\mathrm{max}$ for different values of the pump power at the pump port of the JPA. The input signal has a frequency of 5.55 GHz and a power of −128 dBm.

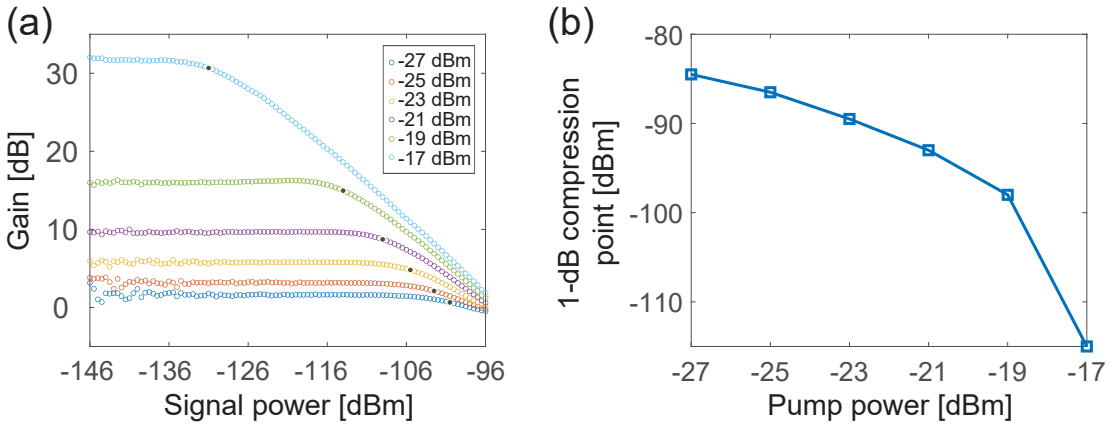

Figure 4.7: (a) JPA gain for different input signal powers. The 1 dB compression points are colored in black. (a) The 1 dB compression point as a function of JPA pump power. The JPA is operating at resonance frequency $f_0 = 5.55$ GHz.

the nondegenerate gain measurement for various input signal powers. Fig 4.7 shows a measurement result for this calibration. We use −130 to −80 dBm of signal power and −11 to −1 dBm of pump power. The signal power is referenced at the input of the JPA by adjusting the signal power from the microwave source with the attenuation in the input line. We see that indeed for higher signal powers the effective gain of the JPA decreases. We observe the expected linear amplification with increasing signal power, until a drop-off occurs due to compression.

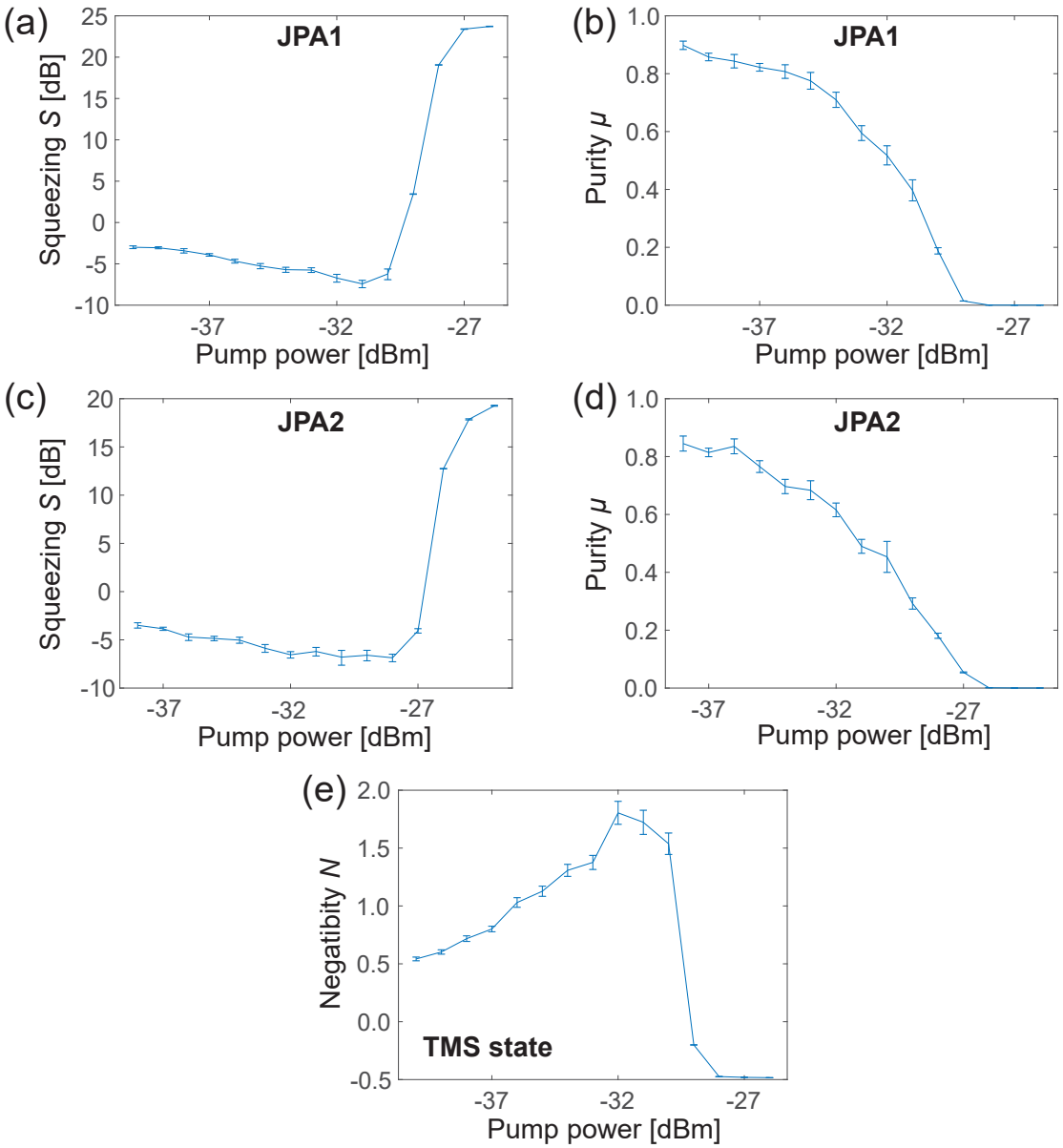

Figure 4.8: Measurement of squeezing levels and entanglement, generated from JPAs. The working point resonance frequency is $f_0 = 5.6$ GHz. Pump powers are referenced to the pump port of the JPA sample holder. (a) Squeezing level of JPA1 as a function of the pump power. (b) Purity of the JPA1 squeezed state as a function of pump power. (b) Squeezing level of JPA2 as a function of the pump power. (d) Purity of the JPA2 squeezed state as a function of pump power. (e) Negativity of the TMS state generated using the two squeezed states from JPA1 and JPA2. We see that $N > 0$ for certain pump powers, which implies entanglement is generated.

4.3.3 Squeezing and entanglement

Squeezed states are the resources used to generate entanglement in our experiment. In order to consistently generate squeezed states with our desired squeezing level and purity,

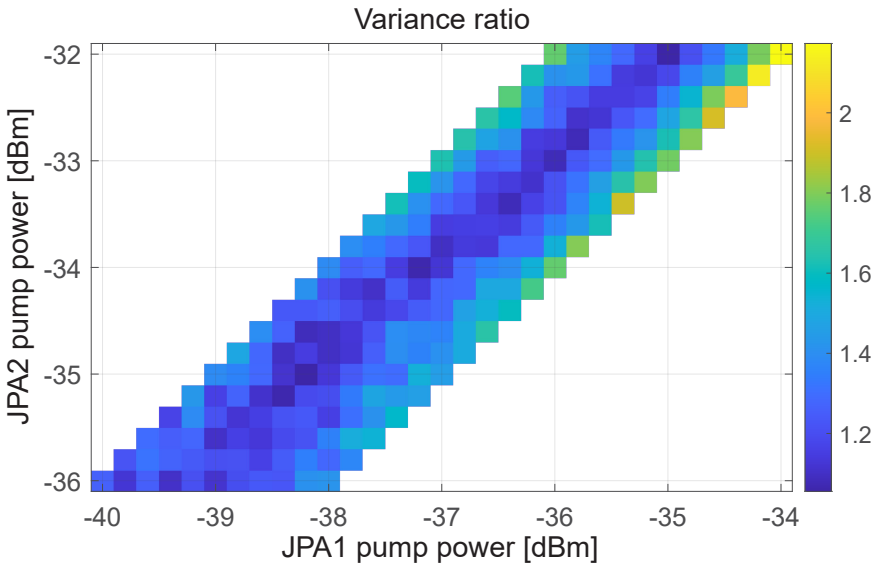

Figure 4.9: Measurement of the variance ratio σ_r^2 while sweeping the JPA1 and JPA2 pump powers. Pump powers are referenced to the pump port of the JPA sample holder. The TMS state is balanced if $\sigma_r^2 = 1$. We observe that the optimal variance ratios lie along the diagonal.

we characterize the squeezed states produced by the JPA. We utilize a FPGA to complete these characterization measurements. Instead of sending input microwave signals to the JPA, we use the weak thermal states emitted by our 30 dB heatable attenuators as input. By operating the JPA in the degenerate mode, the JPA implements a squeezing operation for this weak thermal state. If the JPA noise is sufficiently low, this allows us to suppress the fluctuations in one quadrature below the vacuum limit. The output signals are received at the FPGA.

For a characterization of the squeezing, we generate squeezed states for various JPA pump powers. Fig 4.8(a-d) shows a measurement result for this characterization. We observe that squeezing increases with pump power until a certain point, at which it drops due to higher-order nonlinear effects. We also observe that purity decreases monotonically with pump power.

Entanglement can be generated by superimposing two orthogonally squeezed states at a symmetric hybrid ring, which provides a TMS state at the outputs. The TMS state carries quantum correlations and is employed as a resource for our quantum communication experiments. To characterize entanglement, we generate TMS squeezed states at various JPA pump powers. Fig 4.8(e) shows a measurement result for this characterization. We observe that negativity increases with pump power until a maximum, and then drops due to the deteriorating squeezed states. We also observe that purity decreases monotonically with pump power. In experiment, we want to optimize the entanglement resources for larger squeezing levels, higher purity, and larger negativity.

4.3.4 TMS state balancing

TMS states are generated by superimposing two orthogonally squeezed states. It is the entanglement resource used in our experiments. For an ideal TMS state, the squeezing level of these two squeezed states should be equivalent, which implies that the TMS state locally looks like a symmetric thermal state. We accomplish this optimization by sweeping the pump powers for the two JPAs that produce the squeezed states, and measure the variance ratio $\sigma_{\mathrm{r}}^2 = \sigma_{\mathrm{a},1}^2/\sigma_{\mathrm{s},1}^2 \cdot \sigma_{\mathrm{a},2}^2/\sigma_{\mathrm{s},2}^2$, where $\sigma_{\mathrm{s,i}}^2$ and $\sigma_{\mathrm{a,i}}^2$ are the squeezed and antisqueezed variances for path $i = 1, 2$. The TMS state is balanced if $\sigma_{\mathrm{r}}^2 = 1$. Fig 4.9 shows a measurement result for this optimization. As seen from the measurement, we only need to sweep the diagonal because we want the two JPAs to generate comparable squeezing levels. We complete the optimization procedure by selecting pump power combinations that minimize σ_{r}^2.

Chapter 5

Microwave quantum cryogenic link

In this chapter, we present the microwave quantum cryogenic link (MQCL), which is a prototype structure that enables a quantum local area network (QLAN) in the microwave regime. The cryogenic link allows us to perform quantum teleportation between different labs since it cools down the relevant microwave components. Our MQCL connects two different dilution cryostats, spatially-separated by 6.5 m. In Section 5.1, we discuss the construction of the cryogenic link, including the modules, the superconducting channel, and its assembly. In Section 5.2, we present the experimental entanglement distribution performed over the cryogenic link.

5.1 Cryolink construction

The MQCL is designed in close collaboration with Oxford Instruments and assembled at the Walther-Meißner-Institute. Since the cryolink is a prototype, a large part of our work is devoted to its construction and optimization. In this section, we present the main modules of the MCQL and their respective functions. We discuss the superconducting connection that implements our microwave quantum communication network. We also describe the assembly procedure of the cryolink as well as our modifications to optimize its performance.

5.1.1 Cryolink modules

The MQCL consists of three main modules. The first module is a WMI home-built cryostat, which serves as Alice in the quantum teleportation protocol. The second module is a commercial Triton cryostat from Oxford Instrument, which serves as Bob in the protocol. The third module is a cryogenic link (cryolink), which serves as the communication channel between Alice and Bob. Fig. 5.1 shows the overall structure of the MQCL with the main modules labeled. The MQCL works in such a way that the quantum entanglement resource is generated in the Alice cryostat and then transferred through the cryogenic environment to the Bob cryostat.

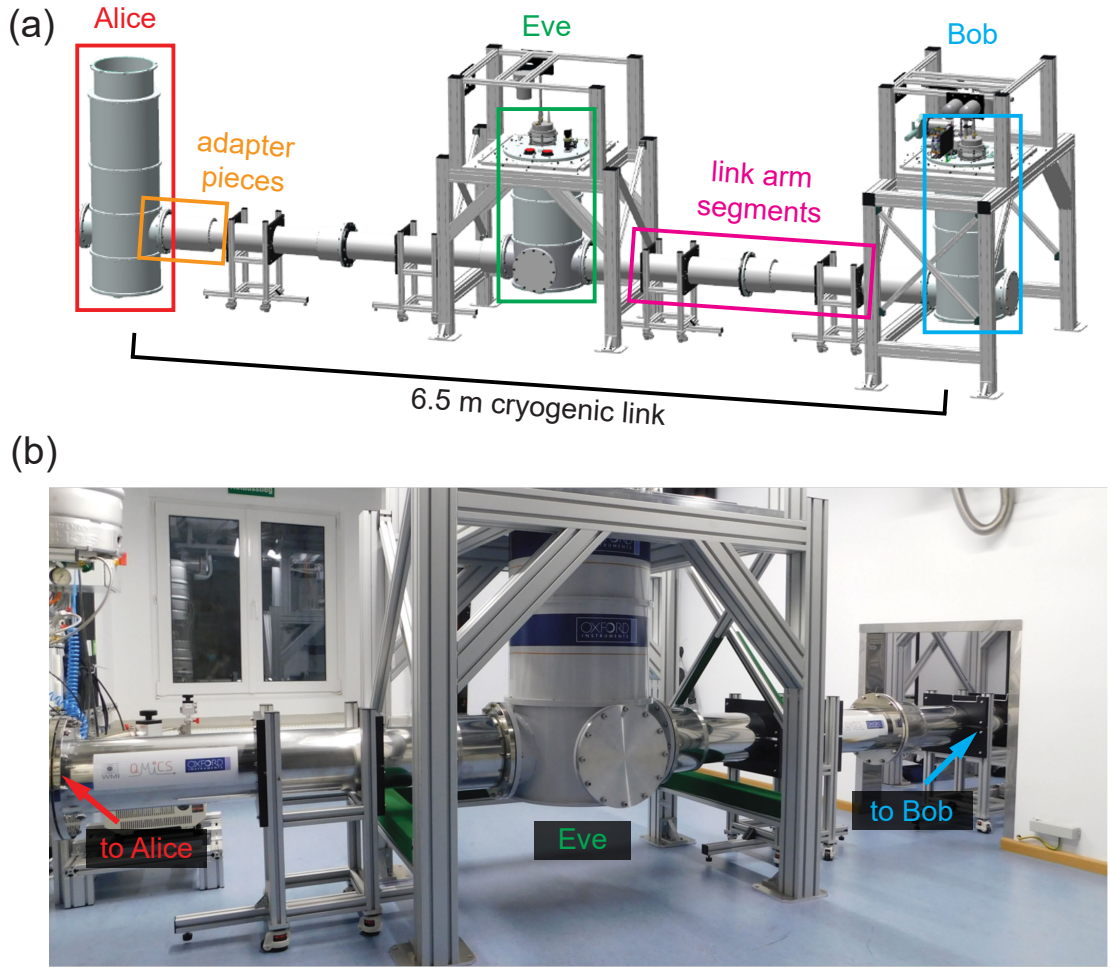

Figure 5.1: (a) CAD drawing of the microwave quantum cryogenic link (MQCL). The main modules are labeled, namely the Alice cryostat, the Eve cryostat, the Bob cryostat, and the cryogenic link. Image courtesy of Oxford Instruments. (b) Photograph of the Eve cryostat with the link arm segments.

Alice cryostat

The Alice cryostat is a dry dilution refrigerator home-built at the WMI [72], but with new shields adapted to the cryolink produced by Oxford Instruments. This cryostat consists of five layers, which from outermost to innermost are: outer vacuum chamber (OVC), pulse tube refrigerator stage 1 (PT1), pulse tube refrigerator stage 2 (PT2), distillation chamber (still), and mixing chamber (MC). The OVC, PT1, and PT2 shields are made of aluminum, while the still and MC shields are made of copper. We remark that these layers are consistent also for the Bob cryostat and cryogenic link, since the chambers are connected across the modules. The structure of the Alice cryostat can be seen from Figure 5.2.

The Alice cryostat uses a Cryomech PT420 pulse tube refrigerator (PTR) to cool the

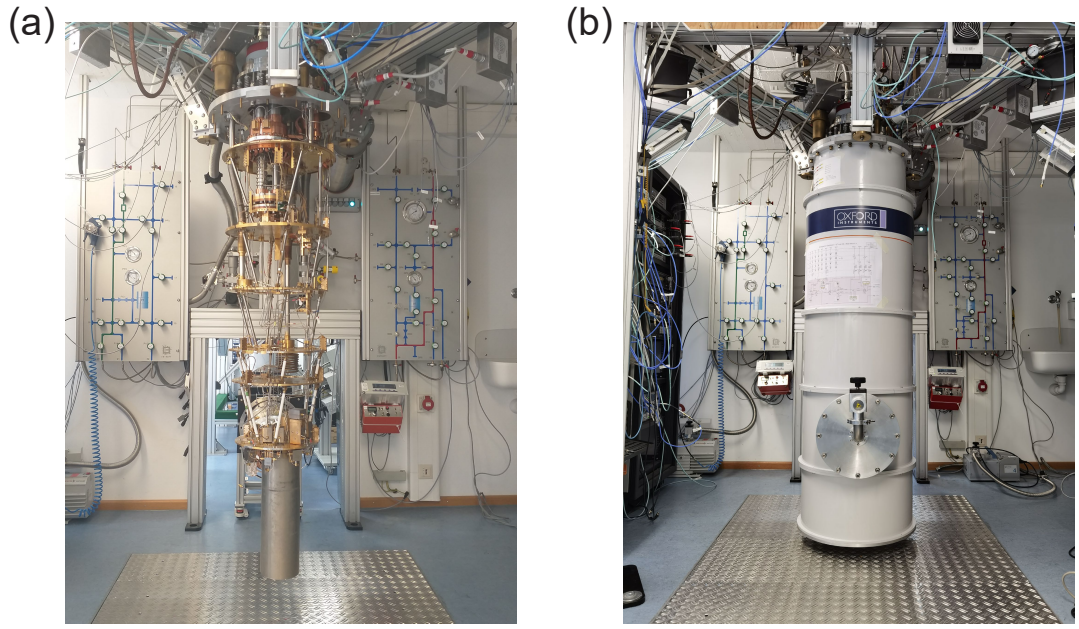

Figure 5.2: (a) Photograph of the inside of the Alice cryostat. (b) Photograph of the Alice cryostat with OVC shields installed.

PT1 and PT2 stages. This PT420 cooler is upgraded from the original PT410 cooler to provide additional cooling power for the Alice cryostat. At the PT1 stage, the PT420 cooler produces 55 W of cooling power at a temperature of 45 K to generate temperatures of $\sim$ 47 K [73]. At the PT2 stage, it produces 2.0 W of cooling power at a temperature of 4.2 K to generate temperatures of $\sim$ 3.5 K. After the PT2 stage, the 1 K pot stage uses evaporative cooling of helium-4 to generate temperatures of $\sim$ 1.2 K. Finally, dilution cooling of helium-3/helium-4 mixture is used at the mixing chamber (MC) stage to provide 300 μW of cooling power at 100 mK, which reaches a base temperature below 11 mK without load [74]. In experiment, we attain a base temperature of $\sim$ 35 mK at the MC stage.

The sample stage is attached and thermalized to the MC stage. During experiment with the cryolink, heatable components and input signals to the sample stage dissipate heat and hence heat up the mixing chamber to $\sim$ 50 mK. Without the cryolink attached, we reach a base temperature of $\sim$ 15 mK. The microwave building blocks installed at the sample stage are detailed in Section 4.1.2.

Bob cryostat

The Bob cryostat is a dry dilution refrigerator manufactured by Oxford Instruments. It uses the commercial Triton design from Oxford Instruments, but with an additional

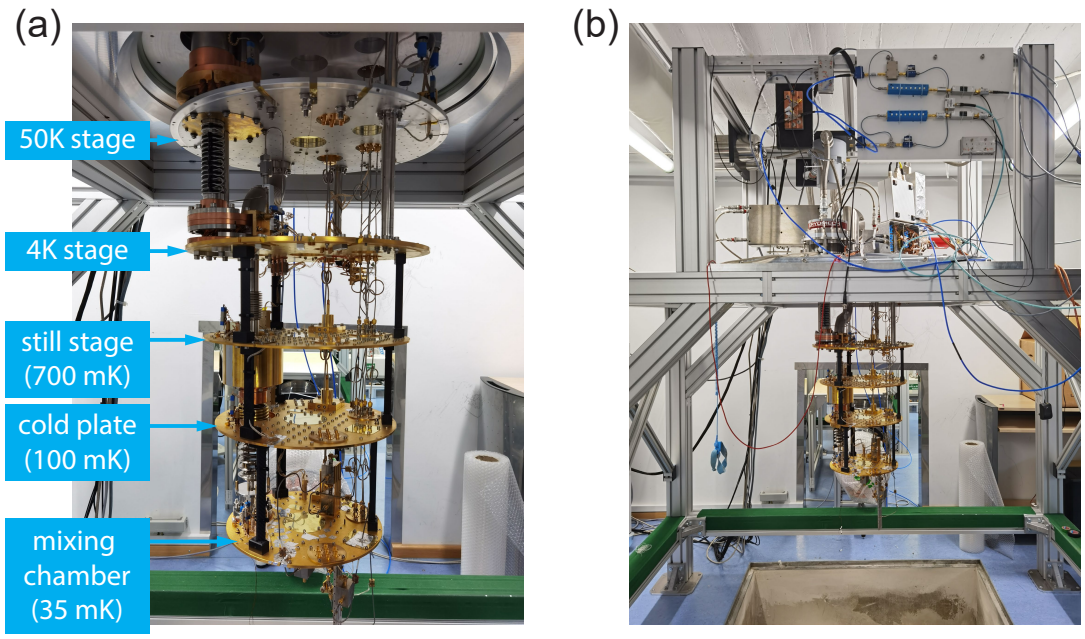

Figure 5.3: (a) Photograph of the Bob cryostat with labels for each temperature stage. (b) Photograph of the Bob cryostat along with the supporting frame.

opening at the bottom shields to connect to the cryolink. The layer structure for the shields of Bob cryostat coincides with that of Alice. However, the Bob cryostat is larger in radius and has significantly stronger cooling power. The structure of the Bob cryostat can be seen from Figure 5.3.

Similar to the Alice cryostat, the OVC, PT1, and PT2 shields are made of aluminum, while the still and MC shields are made of copper. The Bob cryostat uses a Cryomech PT415 Cryocooler PTR to cool the PT1 and PT2 stages. At the PT1 stage, it produces 40 W of cooling power at a temperature of 45 K to generate temperatures of $\sim$ 42 K [73]. At the PT2 stage, it produces 1.5 W of cooling power at a temperature of 4.2 K to generate temperatures of $\sim$ 3.4 K. The Bob cryostat does not have a 1 K pot, and instead uses a Joule-Thomson cooler to generate temperatures of $\sim$ 1.2 K. Dilution cooling is used in the MC to provide 500 μW of cooling power at 100 mK and 20 μW of cooling power at 20 mK [75]. In the case that the cryogenic link is attached, we attain a base temperature of $\sim$ 20 mK, which is lower than that achievable by the Alice cryostat.

During experiment, heatable components and input signals to the sample stage dissipate heat and thus heat up the mixing chamber to $\sim$ 35 mK. The microwave building blocks installed at the sample stage are detailed in Section 4.1.2.

The Bob cryostat shows improved performance compared to the Alice cryostat, mainly because the cryolink shields are designed specifically for the Bob cryostat but not for our home-built Alice cryostat. For example, the pre-cooling and mixing circuits in the Bob

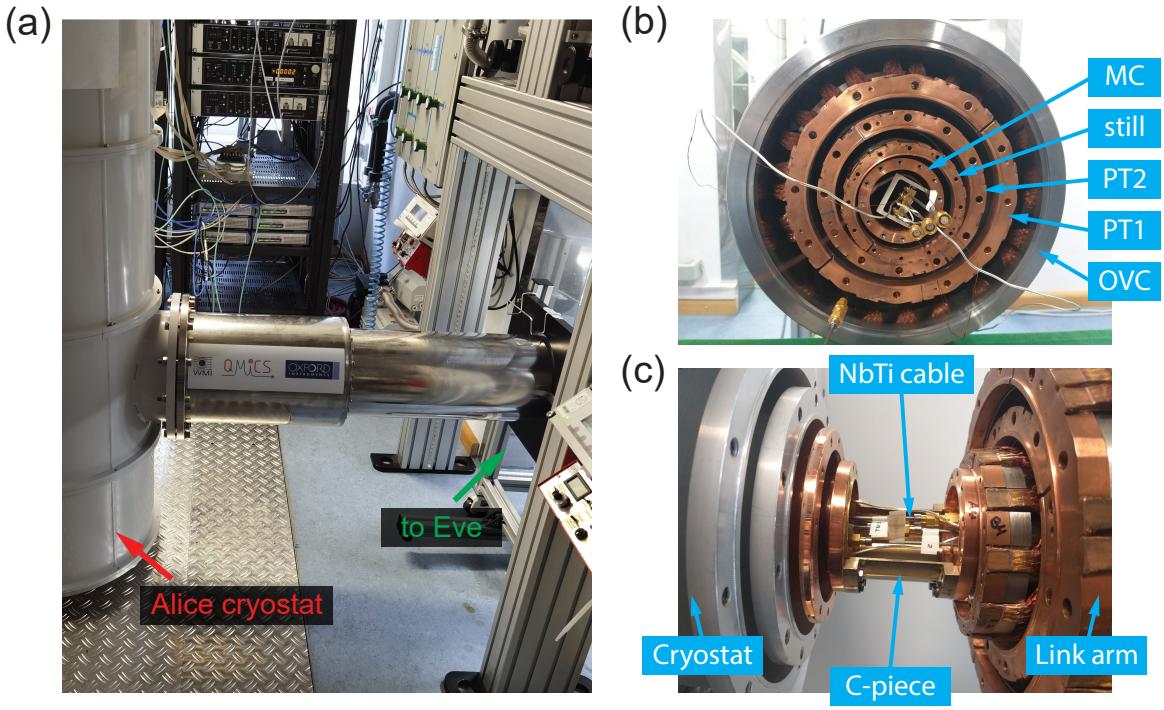

Figure 5.4: (a) Photograph of the adapter piece that connects the Alice cryostat with the link arm segment towards the Eve cryostat. (b) Photograph of the link arm segment with labels for each layer. (c) Photograph of the C-shaped pieces that contain the NbTi superconducting cables and connect the cryostat with the link arm.

cryostat allow greater throughput and the Joule-Thomson cooler requires less pre-cooling of the input mixture. Also, the cooldown is automatically executed in an optimized way, which results in a faster cooldown time. In comparison, the Alice cryostat valves are all manually operated during cooldown.

Cryogenic link

The cryogenic link is the main novel component of the MQCL. It directly connects the mixing chamber shields of the Alice cryostat and the Bob cryostat. The superconducting transmission lines in the cryolink serves as a quantum channel that allows, for instance, entanglement distribution between the Alice cryostat and Bob cryostat. It can also serve as a low-loss classical channel to transmit, for instance, the analog feedforward in our teleportation protocol. The structure of the cryolink can be seen from Figure 5.4.

Consistent with the cryostats, the cryolink consists of five layers separated by high vacuum. These layers are formed by the OVC, PT1, and PT2 shields made of aluminum, and the still and MC shields are made of polished copper. The ends of the cryolink are thermalized by direct contact with the Alice and Bob stages. At the center of the cryolink is a partially equipped cryostat, which we call Eve. The Eve cryostat only has a Cryomech PT415 PTR for cooling the PT1 and PT2 stages, but no dilution unit. The PT415 cooler

can reach a PT2 base temperature of 2.8 K without load. In combination with the cooling from the Alice and Bob mixing chambers, this is already enough to generate temperatures of $\sim$ 50 mK on the Eve mixing chamber tube and temperatures of $\sim$ 100 mK on the superconducting cables inside Eve. This temperature is measured at the center of the superconducting cable, which is threaded in the innermost layer of the cryolink. Thus, dilution cooling is not required for the Eve cryostat.

The Alice and Bob experimental setups are connected using 6-meter-long NbTi superconducting cables threaded through the cryolink. At a base temperature of $\sim$ 120 mK, the cyrogenic channel allows the cables to become superconducting. Thus, quantum signals sent across the cable experience negligible disturbances and we protect quantum coherence in our experiments.

5.1.2 Superconducting cryogenic channel

The cryogenic link connects the Alice mixing chamber with the Bob mixing chamber with a superconducting channel. This is implemented by threading three 6-meter-long NbTi superconducting cables through the cryolink and attaching them to the experimental setups via SMA connectors. These long superconducting cables are thermalized every meter with silver wires. Since the cables are superconducting at cryogenic temperatures, signals can travel through with negligible losses and low thermal noise.

In the experimental setup, three NbTi cables are threaded through the cryogenic link. For the teleportation experiment, one of the cables is used as the quantum channel for entanglement distribution. A second cable is employed as the classical channel for sending the analog feedforward signal. In this section, we discuss the cryogenic quantum and classical channels.

Quantum channel

The quantum channel carries the quantum resource from the Alice cryostat to the Bob cryostat. In the analog quantum teleportation protocol, a TMS state is shared between Alice and Bob as the entanglement resource. This is achieved by generating a TMS state in the Alice setup, by passing two orthogonally squeezed Gaussian states through a beam splitter, and then keeping one output at Alice and sending the other output to Bob. This distribution of quantum entanglement towards the Bob cryostat is done over the quantum channel.

Since the quantum channel utilizes a superconducting cable in cryogenic temperatures, the transferred quantum state can maintain their quantum coherence. This is because NbTi cables have superconducting losses of less than 0.3 dB/m. Furthermore, the thermal noise at the cryogenic link base temperature of $\sim$ 120 mK is $\sim$ 0.1 photons at microwave frequency modes, which is relatively small compared to the signal of $\gtrsim 1$ photons. Thus, the quantum resource can be obtained with relatively high purity at the

Bob cryostat, which enables the analog quantum teleportation protocol. We note here that the fluctuation-dissipation theorem implies that losses and noise cannot be regarded as decoupled quantities and only their product is relevant.

Classical channel

In the analog quantum teleportation protocol, the Bell measurement result is sent from Alice to Bob in the classical feedforward channel, and determines the displacement for retrieving the input state. The Bell measurement is realized by superimposing the input state and Alice's TMS resource state via a beamsplitter, and then projecting the superposition along two orthogonal quadratures. This operation is implemented by strongly amplifying the signal along certain quadratures, which approximates a projection in the large gain limit [14]. The feedforward signal becomes classical since the power of vacuum fluctuations becomes small compared to the signal power.

Similar to the quantum channel, the classical channel benefits from negligible losses and low thermal noise. However, these conditions are not necessary since the feedforward signal is relatively robust against losses and noise. In particular, losses in the classical channel can be compensated by increasing the gain before the classical channel. Also, ambient thermal noise in the classical channel is small when compared to the strongly amplified feedforward signal. Thus, we can interpret that quantum teleportation performs error-correction on the classical feedforwad signal, which is discussed in Section 3.3.3. The main deterioration of the feedforward signal happens due to the amplification noise of the amplification devices. This is due to the Friis equation, where the amplifier noise is effectively amplified in the same way as the signal.

In view of the robustness of the feedforward signal against losses and noise, a variation of the experimental setup is proposed. That is to send the feedforward signal over a room-temperature classical channel instead of through the cyrogenic link. This method is feasible because the main obstacle with implementing a room-temperature feedforward is the high thermal noise, which can eventually be overcome with sufficient amplification within the cryogenic stages. Analysis and simulation results in this regard are presented in Section 3.3.

5.1.3 Assembly of cryogenic link

The cryogenic link is a novel device, especially with arm segments that connect three cryostats. In total, the cryolink consists of around 60 shields and 2000 screws that must be installed for assembly. While the cryolink components have been tested by Oxford Instruments, we complete the first installation of the entire cryolink and discover many empirical solutions. Since assembling the cryolink requires great technical care and patience, we describe the whole assembly procedure in a precise way. In this section, we explain the assembly procedure and describe the alignment between the cryostats and the

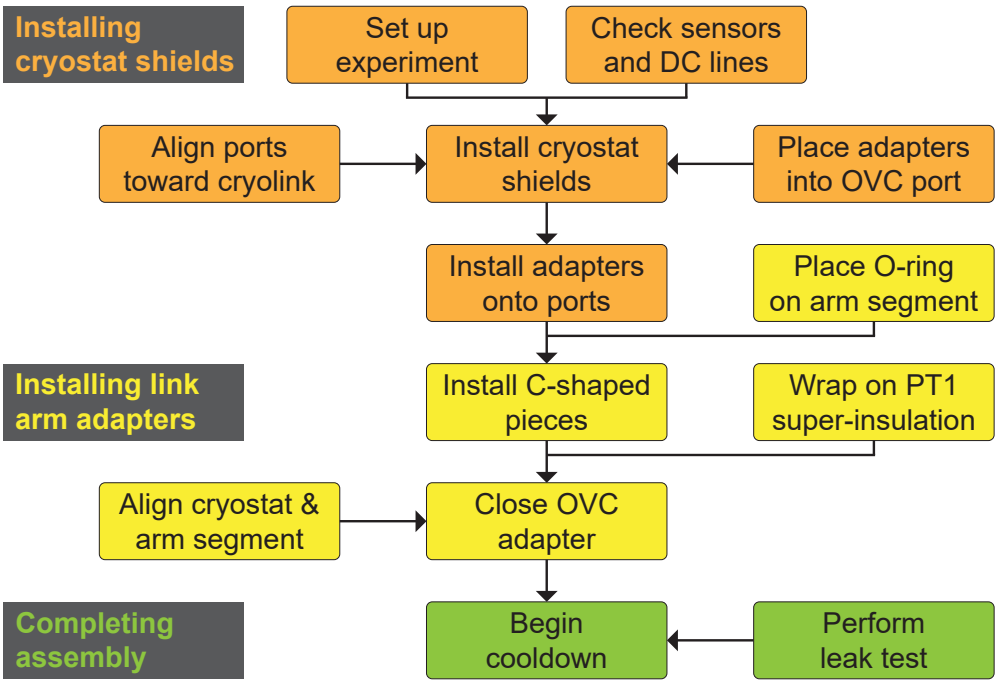

Figure 5.5: Flowchart of the assembly procedure for the cryogenic link. The middle column lists the main assembly procedures. The side columns list the auxiliary steps for each procedure.

cryolink arm. The system is ideally installed with three people.

Assembly procedure

We explain in detail the assembly procedure, since the cryolink parts fit together in an interdependent way. In particular, some components must be fixed in a specific order, otherwise they are not possible to access afterwards. The assembly procedure can be divided into three parts, namely installing the cryostat shields, installing the link arm adapters, and completing the assembly. Figure 5.5 is a flowchart of the assembly procedure.

In the first step, we close the shields of the respective individual cryostats and keep the bottoms of the shields open to maintain access to the experimental setup, before connection of the link arms. The procedure is similar for both the Alice and Bob cryostats. The shields must be screwed onto the cryostat starting from the uppermost stage and innermost layer, then proceeding downwards and outwards. This requires two to three people, with one person screwing and one to two people holding the shield. It is important to note the size of each shield before installing, as some outer shields are large, such that an inner shield of a lower stage should be installed before this outer shield. Great care should be taken when closing the OVC shields since the Viton O-rings used are susceptible to dust, which might eventually create leaks. The main difference between the MQCL

prototype and conventional cryostats is the connection to the link arm segments. When installing the shields that attach to the arm segments, the connection ports can be aligned via long screw holes. It is important to carefully align each cryostat shield with respect to the link arm, since the orientation of the inner shields cannot be changed after installation of the OVC shield. Once the shields are installed, corresponding blanks are fixed on the connection ports on the opposite side of the link arm.

Installing the link arm adapters requires careful alignment between the cryostat and the link arm. First, the cylindrical adapter pieces must be inserted coaxially inside the connection ports of the cryostat shields. This should be done when installing the OVC shield, such that the cylindrical adapter pieces are placed inside the connection port while the OVC shield is installed. Otherwise, there is not enough space to insert the cylindrical adapter pieces after the OVC shield is installed. Then, the cylindrical adapter pieces are screwed onto their corresponding shields, where the MC and still adapters are screwed from the inside of the cryostat and the PT2 and PT1 adapters are screwed from the outside. We use molybdenum washers on the MC to establish better thermal contact at cryogenic temperatures, since this type of washer compensates for the different contraction lengths of our stainless steel screws and copper pieces. The still and PT2 adapters should first be fixed with a few screws, which makes installing the MC cylindrical adapter pieces more convenient. After the link adapter pieces are screwed onto the cryostat ports, the C-shaped adapter pieces used to connect with the link arm segment can be installed. It is crucial to place the arm segment O-ring before attaching the C-shaped pieces, since the O-ring cannot be inserted after the adapter pieces are installed. Also, before installing the C-shaped pieces, we need to bend in situ the superconducting cables from the setup and the silver thermalization wires through the connection port for the mixing chamber. It is crucial to check that the superconducting cables and silver wires are connected, as they cannot be accessed after the C-shaped pieces are installed. While the C-shaped pieces allow for decent mechanical flexibility, the alignment must still be done slowly and precisely. Thus, it is better to screw the pieces with multiple revolutions, such that the tension is evenly distributed. We again use molybdenum washers on the MC pieces for better thermal contact. Next, we use aluminum tape to cover the gaps in the C-shaped pieces to reduce thermal radiation. To align the PT2 and PT1 pieces, we need to overcome greater tension in the link arm segment. Thus, it is easier to hold the arm segment in place and then to insert the C-shaped pieces. After installing the C-shaped pieces, it is important to wrap at least 20 layers of superinsulation around the PT1 pieces and link arm segments, as this significantly reduces the impact of thermal radiation from the room temperature shield. Finally, the OVC adapter can be attached. This is done by first screwing the adapter piece to the correct position on the link arm segment and then aligning the arm segment with the cryostat connection port. This alignment process is described in detail in the next section.

After the entire cryolink is installed, we complete the assembly procedure by performing

a leak test. The leak test is important to make sure that no gas from the atmosphere enters the cryolink, which would cause a thermal short between the layers. Once the leak test is completed, we can begin a full cooldown of the cryolink. We first start the pre-cooling process by turning on the PTRs of Alice, Bob, and Eve. After the PT2 stages reach temperatures below 4 K, we can start the 1K circuit and mixture circuit in Alice. We start the commercial cooldown script for Bob only when Alice nearly finishes condensation, since Bob condenses faster than Alice. The cooldown is complete when the mixtures in both Alice and Bob are fully condensed.

Cryolink alignment

Careful alignment of the cryostat connection ports with the link arm segment is crucial for establishing a vacuum-tight connection between the cryostat shields and the link arm. While there a a few centimeters of leeway in the cryolink design, the different modules of the cryolink move by a few centimeters after cooldown and disassembly due to thermal and mechanical stress in the system. Thus, the cryolink modules need to be almost completely realigned for each assembly. In particular, it is important to match the displacement and angle between the OVC adapter and its connection port for alignment. In the following, we describe how we realize this fine-tuned alignment.

There are several places which allow for flexibility regarding alignment. The Alice cryostat can be adjusted by the flexible washers and the pressure gauges in its supporting frame. The Eve cryostat can be adjusted by screwing the supporting plate on its frame, such that the screws push the cryostat in the opposite direction. The Bob cryostat can similarly be adjusted by screwing the supporting plate on its frame. The cryostat frames can also be moved by pushing to gain distance. The link arm segments can be raised by using a lifting crane, so that the link arms match in height with the cryostat connection ports. When aligning the cryolink, it is better to first match the angular orientation between the link arm segments and the cryostat connection ports while leaving a gap, and then adjust the displacement to close the gap. The angular orientation can be adjusted at the Alice and Bob cryostats by rotating the entire cryostats. The displacement can be adjusted by pushing the Eve cryostat. Once one side of the cryolink is closed, it is still possible to push the Eve cryostat towards the other side to gain distance. It is important to take care that the orientation between link arm segments and the cryostat connection ports match, because misalignment easily leads to a leak.

5.1.4 Cryolink modifications

We make several modifications to the MQCL to optimize its performance. In particular, the cooling power of the individual cryostats can be upgraded to support the larger cryolink structure. Additionally, we insert charcoal sorbs and superinsulation to let the cryolink run in a more stable manner. In this section, we discuss the cold head replacement and

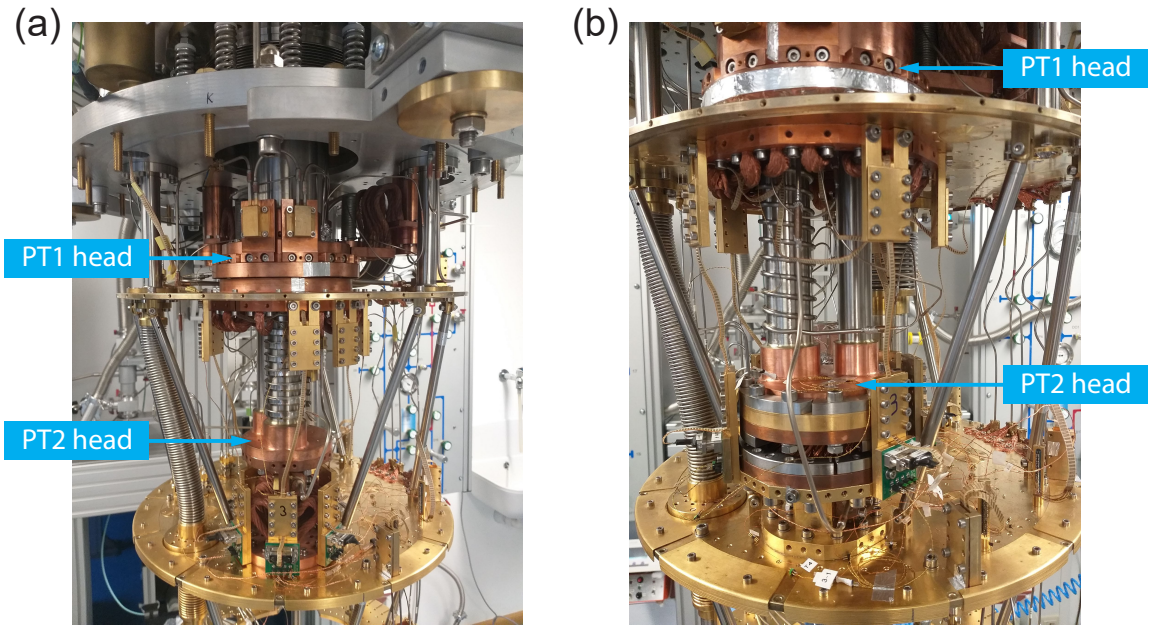

Figure 5.6: (a) Photograph of the old Cryomech PT410 PTR cold head installed in the Alice cryostat. (b) Photograph of the new Cryomech PT420 PTR cold head installed in the Alice cryostat.

additional components inserted to improve the cryolink performance.

Cold head replacement

The Alice cryostat originally uses a Cryomech PT410 Cryocooler pulse tube refrigerator, which has 40 W cooling power at 45 K and 1.0 W cooling power at 4.2 K, at its PT1 and PT2 stages [73]. However, in the first cooldown attempt with the entire cryolink, the Alice cryostat only reached final temperatures of 62 K at the PT1 stage and 5.6 K at the PT2 stage. These temperatures are significantly higher than the target values of $\sim$ 45 K at PT1 and $\sim$ 3 K at PT2, and are insufficient for recondensing the helium-3 that is pumped out of the still chamber with the TMP. The dilution cooling process does not work effectively and a mixing chamber temperature of only $\sim$ 500 mK is attained. Thus, we look to upgrade the cold head onto a Cryomech PT420 Cryocooler PTR, which has 55 W cooling power at 45 K and 2.0 W cooling power at 4.2 K [73]. In order to replace the cold head, new adapters must be designed since the old and new cold heads have slightly different heights. Furthermore, the capillaries for the helium circuits need to be resoldered for the cold head exchange. The entire modification process is done with care due to the tight space and myriad components inside the cryostat. Fig. 5.6 compares the old and new cold heads installed in the Alice cryostat.

After installing the Cryomech PT420 Cryocooler PTR, the Alice cryostat reaches

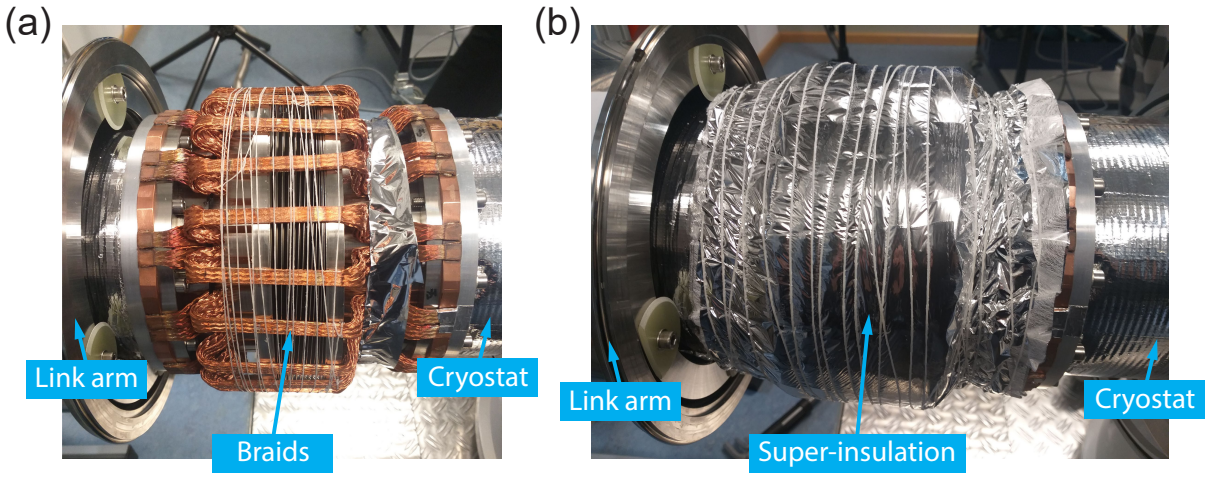

Figure 5.7: (a) Photograph of the thermalization braids at the cryolink arm segment. We tie down the braids with wax string to prevent thermal contact with the OVC adapter piece. (b) Photograph of the superinsulation wrapped around the thermalization braids. We add the superinsulation to reduce thermal radiation from the OVC layer to the PT1 layer.

temperatures of 59 K at the PT1 stage and 4.6 K at the PT2 stage, which is still insufficient to effectively execute dilution cooling. While the Alice mixing chamber reaches a temperature of $\sim$ 100 mK, it is largely due to cooling power from the Bob mixing chamber. After inspecting the entire cryolink, we find that the OVC adapters between the cryostats and the link arm segments are significantly colder compared to room temperature. We suspect that there is a touch between the PT1 braids in the link arm segment and the room-temperature OVC shields. Thus, we tie down the braids using multiple layers of wax string and cover them with superinsulation to reduce the thermal coupling, as shown in Fig. 5.7. As a result of this modification, the Alice cryostat attains 49 K at the PT1 stage and 3.5 K at the PT2 stage. This is then sufficient for a full cooldown and we achieve a base temperature of 35 mK at the Alice mixing chamber.

Charcoal sorbs and superinsulation

There are a few additional components added into the cryolink to improve its performance. During each cooldown, there is a clear uptrend in the Alice PT2 temperature of around 1 mK/hr. With an initial temperature 3.5 K and a limiting temperature around 4 K, at which liquid helium begins to evaporate, this means that the cryolink can only survive for around three weeks before it breaks down. This uptrend is probably a result from gas leakage into the cryolink vacuum through out Viton O-rings. Thus, we install several charcoal sorbs and more superinsulation, hoping to extend the lifetime of a cryolink cooldown. Fig. 5.8 show how these additional components are installed.

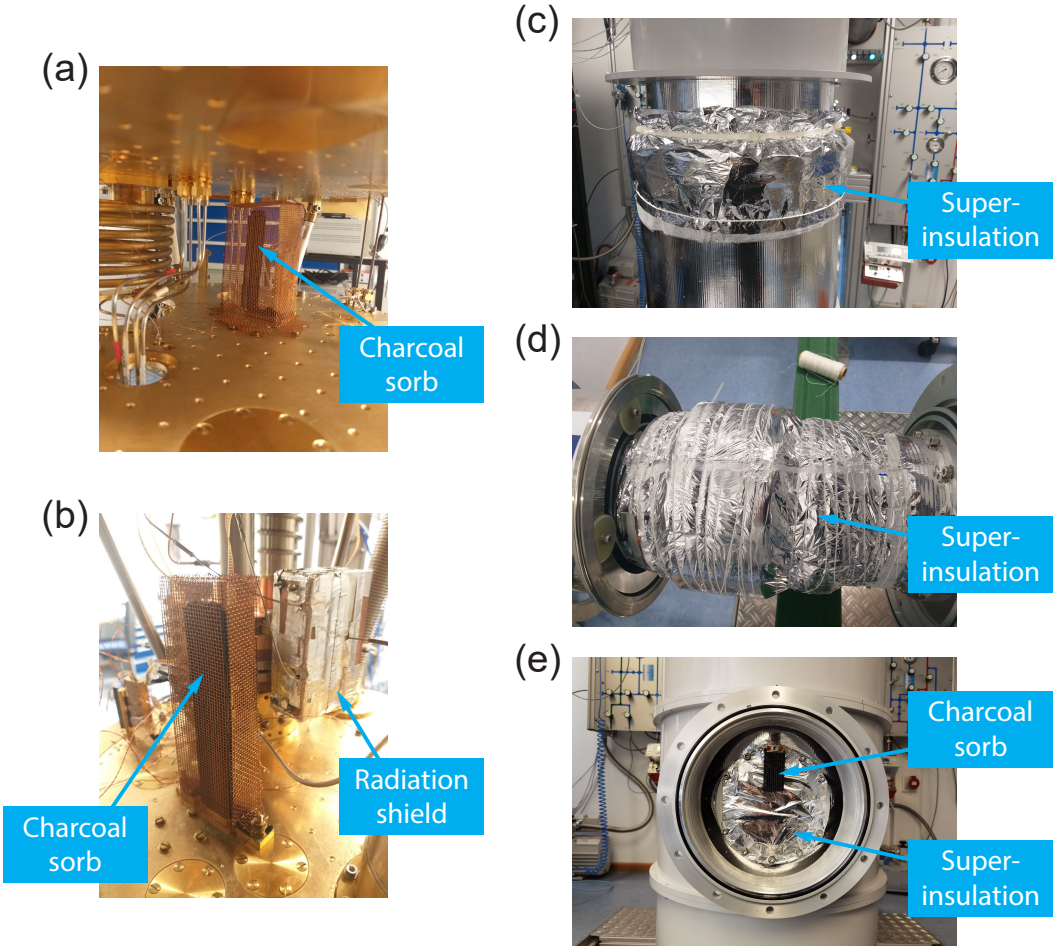

Figure 5.8: (a) Photograph of a small charcoal sorb placed between the still and MC stage of the Alice cryostat. (b) Photograph of a large charcoal sorb placed at the PT2 stage of the Alice cryostat. (c) Photograph of superinsulation wrapped around the PT1 shield of the Alice cryostat. (d) Photograph of the superinsulation wrapped around the thermalization braids near the PT1 link arm adapters. (e) Photograph of the superinsulation and charcoal sorb added to the PT1 blank.

Charcoal sorbs work as strong absorption pumps for fluids at cryogenic temperatures. We hypothesize that nitrogen and water may leak into the cryolink vacuum from the atmosphere. In addition, we potentially suffer from cold leaks in our resoldered helium circuits. These fluids create a thermal shortage between stages, which might create more heat leakage and reduce the effective cooling power of the system. Hence, we place charcoal sorbs at several strategically chosen locations around the cryolink, namely onto the PTR stage of the Alice cryostat, onto the coil exchanger stage of the Alice cryostat, and at the PT1 blanks of all three cryostats. However, this does not significantly improve the temperature uptrend of the cryolink, which means that the heating effect may not come

from helium leakage. From this experiment, we learn that these temperature uptrends are not a result from fluids which directly short different temperature stages, but potentially from water which freezes on top of the superinsulation and thereby changes the reflective properties of the PT1 shields.

Superinsulation improves the reflective surface properties and thereby reduces the heat load from thermal radiation. We cover the cryostat shields and link arm adapters of the PT1 stage with superinsulation and see a significant improvement in the cryolink temperatures, with the Alice PT2 initial temperature dropping from around 3.8 K to 3.5 K. This means that it is crucial to reduce thermal radiation from the OVC to the PT1. However, even with superinsulation the temperature uptrend still persists at the same rate, which means that the temperature uptrend probably results from the fact that the reflection properties of the superinsulation change over time due to gas adsorption. Nevertheless, the superinsulation extends the cryolink lifetime by multiple days.

The uptrend results from the change of the superinsulation reflection properties, which is likely due to water which diffuses through the O-rings. It might be helpful to investigate each module separately or with less thermal load, and observe how the system evolves. A possible solution is to improve the helium-3 precooling in the Alice cryostat, for example by installing a Joule-Thomson cooler or additional counterflow heat exchangers. In addition, we can add superinsulation to the remaining link arm segments, which have not been open since initial installation.

5.2 Entanglement distribution

The MQCL allows the sharing of quantum information in a cryogenic environment. Due to the cryogenic temperature, propagating quantum microwave signals can travel across the superconducting cable while maintaining quantum coherence. In our experiment, we demonstrate quantum state transfer and entanglement distribution over the MQCL. The success of these processes is the foundation for more advanced quantum communication protocols, such as quantum teleportation. In this section, we describe quantum state transfer and entanglement distribution over our the MQCL and present the corresponding experimental results. We also discuss entanglement distribution over a thermal channel which we artificially create by heating the center of our cryogenic link.

5.2.1 Quantum state transfer

Quantum state transfer is implemented in the MQCL by generating a squeezed state in the Alice cryostat and then sending it to the Bob cryostat. First, a pumped JPA in the Alice mixing chamber generates phase-space squeezing in a selected vacuum mode around 5 GHz. Then, the squeezed state propagates to Bob through a superconducting cable over the cryogenic link. We determine the success of quantum state transfer by amplifying the

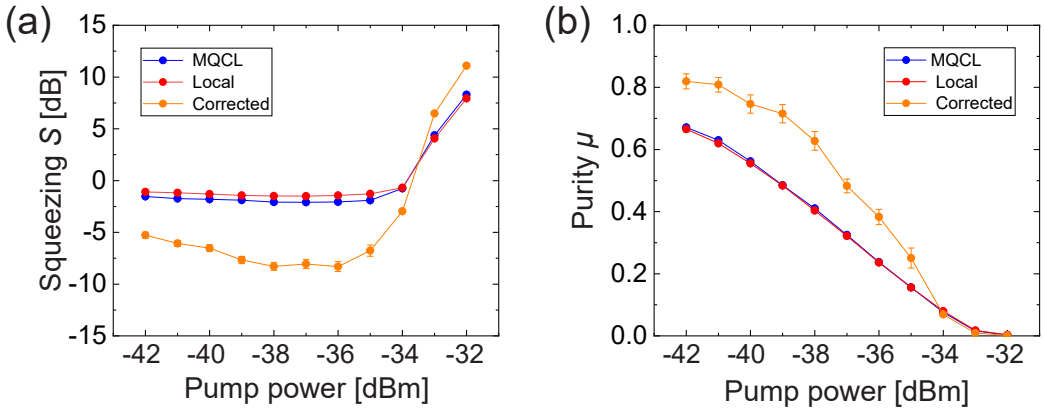

Figure 5.9: Measurement of quantum state transfer over the cryolink. The working point resonance frequency is $f_0 = 5.435$ GHz. Pump powers are referred to the input port of the JPA pump. (a) Squeezing level as a function of pump power. (b) Purity as a function of pump power. QLAN represents the state sent across the MQCL, local represents the state measured at Alice, and corrected represents the state after correcting for the hybrid ring.

propagating signal from Bob and measuring it with a room-temperature FPGA setup on the Alice side. Experimentally, we measure that indeed a squeezed state is retrieved in the Bob cryostat, which corresponds to the quantum state generated from the Alice cryostat.

Fig. 5.9 shows the experiment results for quantum state transfer. We compare the local version of a generated squeezed state with the version that is sent over the MQCL, and find that the results match well. We remark that the measured squeezing level is limited to 3 dB, because the squeezed state passes through a hybrid ring and becomes mixed with a weak thermal state. The weak thermal state contributes a minimum quadrature variance of 1/8, which corresponds to a squeezing level of 3 dB. We can retrieve the original squeezed state by using quantum state reconstruction as detailed in 4.2.3. With this method, we reconstruct a maximum squeezing level of around 8 dB. We also measure the purity of the squeezed state and see that purity decreases with higher pump power due to amplification noise. Thus, when generating squeezing states for our experiment, there is a trade-off between squeezing level and state purity.

5.2.2 Entanglement distribution over the cryolink

Entanglement distribution over the cryolink is implemented in the MQCL by generating a TMS state in the Alice cryostat and then distributing it between Alice and Bob. First, two pumped JPAs in the Alice mixing chamber generate phase-space squeezing along orthogonal quadratures in a selected vacuum mode around 5 GHz. The two squeezed states pass through a hybrid ring, which forms a TMS state at the outputs. Then, one output signal is kept in Alice and the other output signal is sent to Bob through a superconducting

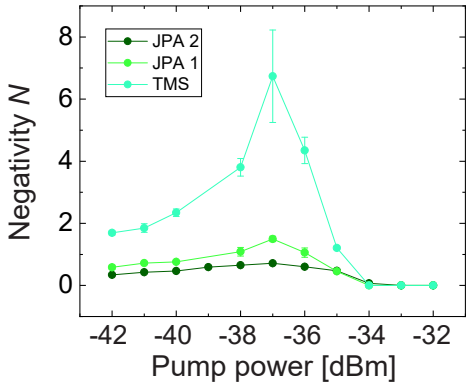

Figure 5.10: Measurement of entanglement distribution over the cryolink, by calculating negativity as a function of pump power. The working point resonance frequency is $f_0 = 5.435$ GHz. Pump powers are referred to the input port of the JPA pump. JPA1 represents the state when only JPA1 is pumped, JPA2 represents the state when only JPA2 is pumped, and TMS represents the state both JPAs are pumped. We see that $N > 0$ for certain pump powers, which implies that entanglement is shared over the cryolink.

cable over the cryogenic link. Finally, the TMS state is shared between Alice and Bob, with which we reconstruct the respective quantum correlations. In addition to the TMS state measurement, we also measure single-mode squeezed states, generated by JPA1 or JPA2 individually, that are split up by a hybrid ring. We determine the success of entanglement distribution by amplifying the propagating signals from Alice and Bob, and measuring them with a room-temperature FPGA setup. In this measurement, we look for quantum correlations between the signal quadratures and determine the negativity, which acts as an entanglement monotone. The negativity is defined as in Section 2.1.3. Experimentally, we measure that indeed the signals from Alice and Bob are entangled, which implies successful entanglement distribution.

Fig. 5.10 shows the experiment results for entanglement distribution over the cryolink. We measure the negativity of the states shared over the cryolink to determine the quantum entanglement. When we share quantum states between Alice and Bob with squeezing only in JPA1 or JPA2, we measure negativity $N > 0$ for all pump powers below 7 dBm , indicating shared quantum entanglement. When both JPAs generate squeezing and we share a TMS state between Alice and Bob, the negativity becomes much higher. This verifies that we indeed distribute quantum entanglement between Alice and Bob in the form of a TMS state.

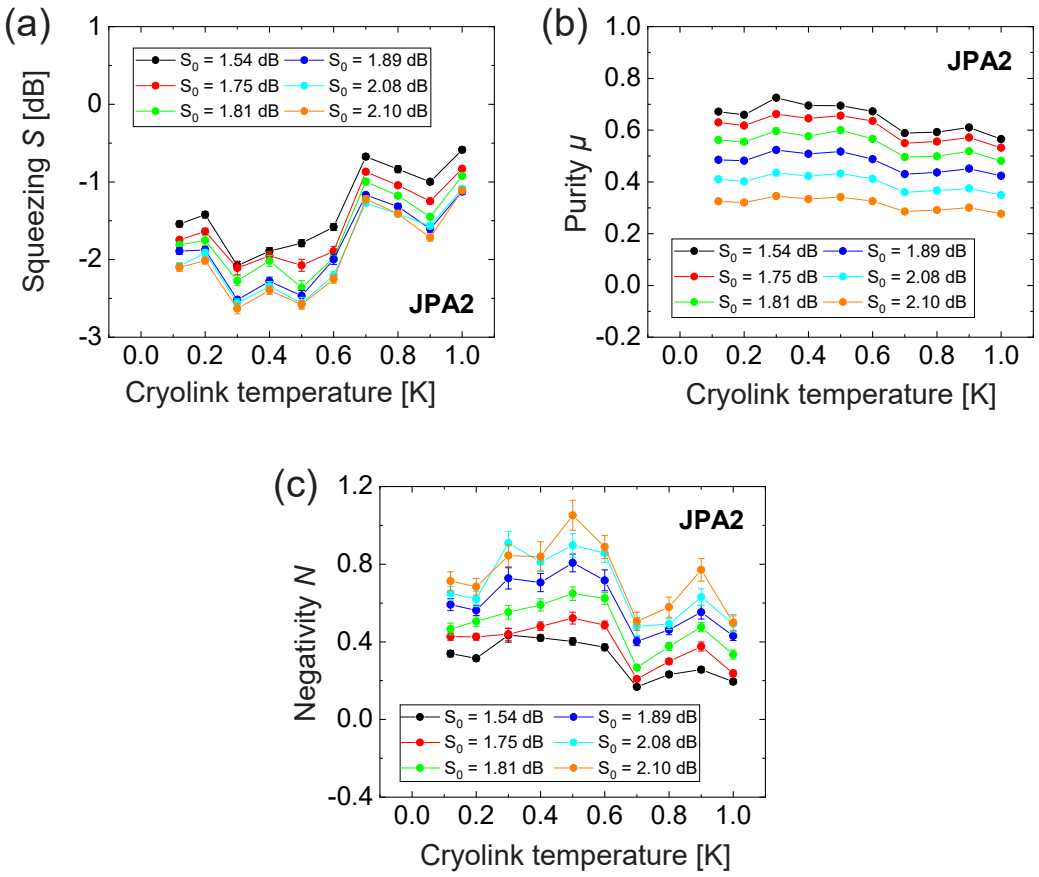

Figure 5.11: Measurement of entanglement distribution at elevated temperatures. The working point resonance frequency is $f_0 = 5.435$ GHz. S_0 represents the squeezing level at base temperature. The cryolink temperature is measured as the ambient temperature at the center of the cryolink. We share a squeezed state generated by JPA2 over the cryolink. (a) Squeezing level as a function of cryolink temperature. (b) Purity as a function of cryolink temperature. (c) Negativity as a function of cryolink temperature. We see that there are fluctuations in the squeezing level values.

5.2.3 Entanglement distribution over a thermal channel

Entanglement distribution over a thermal channel is implemented in the MQCL by repeating the previous experiments in Section 5.2.1 and Section 5.2.2 but for multiple PID-stabilized temperatures at the cryolink center. The temperature of our superconducting transmission lines inside the cryogenic link is controlled using PID control architecture, consisting of a 100 Ω heater and a rubidium oxide sensor. Since the heater is placed at the cryolink center, it provides the benefit of a localized heating in the center.

By inducing elevated temperatures in the cryolink environment, we can examine the effect of ambient thermal noise on the entanglement distribution. In general, additional thermal

noise in the environment couples into the quantum signal via the beam-splitter model and reduces the quantum correlations in the signal. However, since the superconducting cables used to carry the signal has low losses, the coupled thermal noise is negligible over the 6.5 m cryolink distance. Thus, as long as the channel is still superconducting, there should be no significant difference in the properties of entanglement distribution up to moderate temperatures. In this measurement, we follow the same procedure as in Section 5.2.1 and Section 5.2.2 to characterize entanglement distribution but vary the cryogenic link temperature from 120 mK base temperature up to 1 K. Experimentally, we measure that indeed the entanglement distribution performs similarly across temperatures and that the cryogenic channel is robust against ambient thermal noise.

Fig. 5.11 shows the experiment results for entanglement distribution at elevated temperatures. We generate a single-mode squeezed state and distribute it between Alice and Bob by splitting it through a hybrid ring. This procedure mixes the squeezed state at on input with a weak thermal state at the other input. We measure the squeezing, purity, and negativity of the shared state over the cryolink while changing the cryolink temperature. These values are relatively independent of the cryolink temperature, with fluctuations explained by variations in the heatable attenuator temperature. In particular, the purity of the shared state remains stable across temperatures, indicating that there is little influence from the thermal noise. This verifies that indeed entanglement distribution over our MQCL is robust against ambient thermal noise up to moderate temperatures. We thereby demonstrate the fluctuation-dissipation theorem.

Chapter 6

Experimental quantum teleportation

In this chapter, we present the experimental results for quantum teleportation over the MQCL. This is the first demonstration of microwave quantum teleportation between spatially-separated cryostats. The successful realization of the quantum teleportation protocol with propagating microwaves is a strong step towards establishing a QLAN in the microwave regime. In Section 6.1, we present the results of our quantum teleportation measurement, including the necessary calibration measurements. In Section 6.2, we discuss our plans for implementing quantum teleportation over a room temperature feedforward channel.

6.1 Microwave teleportation over MQCL

The MQCL is used in our quantum teleportation experiment to provide a cryogenic environment for entanglement distribution and for transmitting the feedforward signal. The measurements in our experiment are done in analogy to the measurements in Ref. [14]. In order to perform quantum teleportation with high fidelity, we need to generate a balanced TMS as state entangled resource and perform a balanced Bell measurement. Furthermore, we need to calibrate the input displacement photon number to determine our available codebook space and communication security. In this section, we describe the calibration and balancing measurements needed to perform quantum teleportation. Finally, we present the measurement results of our microwave quantum teleportation experiment. We note that JPA1 and JPA2 are used to generate the TMS state, while JPA4 and JPA5 are used to implement the Bell measurement. JPA3 is installed in the setup to generate squeezed input states, but is not utilized for our current experiment.

6.1.1 State displacement calibration

We perform a coherent photon number calibration in order to determine the displacement of our coherent signals at the input of Alice's measurement setup. This is needed when we want to generate input signals of a desired displacement and compare them to the output signal displacement. The amplitude and phase of the displacement is determined by the

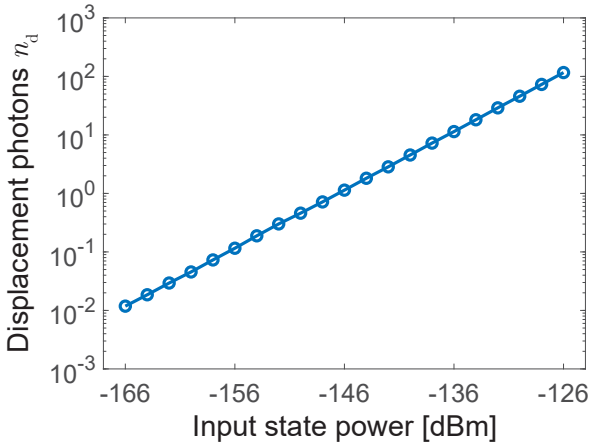

Figure 6.1: Calibration of displacement photons in terms of input state power, referred to the input port of the JPA signal line. The input signal has a frequency of 5.55 GHz.

power and phase of the coherent signal, respectively. Thus, we need to map the coherent input power to displacement photon numbers. We do this calibration by measuring the output when the SGS microwave source is chosen at a specific signal power, along with the reference when the SGS source is turned off and no displacement is applied. We run the measurement in a 2-pulse scheme using the DTG, where each pulse activates a different subset of microwave sources. We then use reference state reconstruction to determine the displacement photon number at our chosen signal power.

Fig. 6.1 shows the measurement results for our state displacement calibration, where we use working frequency $f_0 = 5.55$ GHz. We plot the displacement photon number n_d obtained from reference state reconstruction against the input signal power. We use input state powers ranging from -166 to -126 dBm, which correspond to displacements of around 10^{-2} to 10^2 photons. This range is sufficient to cover the displacement regime we are interested in for our quantum teleportation experiment, which ranges from a few photons to tens of photons. As expected, we see that the displacement photon number depends linearly on the input power.

6.1.2 State balancing calibration

We perform state balancing calibration in order to obtain higher fidelities and no phase dependence in our quantum teleportation result. We begin the calibration by choosing rough working points for JPA1 and JPA2 for generating a TMS state and by choosing rough working points for JPA4 and JPA5 for the Bell measurement. We then fix the JPA2 and JPA4 parameters, and optimize the state balancing by varying the JPA1 and JPA5 parameters. For the state balancing calibration, we use 1.1 displacement photons, corresponding to input signal power of -146 dBm. To begin the calibration procedure, we choose a squeezing level of 3 dB, corresponding to initial JPA1 pump power of -75

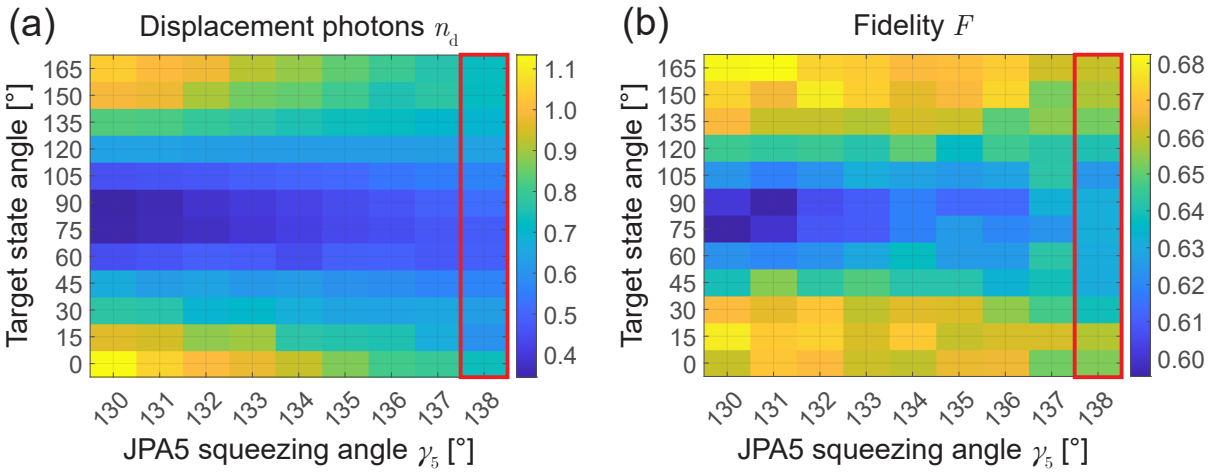

Figure 6.2: Optimization of JPA5 squeezing angle for the quantum teleportation experiment. The input signal has a frequency of 5.55 GHz and displacement photon number of 1.1. (a) Measurement of displacement photons n_d while sweeping JPA5 squeezing angle γ_5 and target state angle. (b) Measurement of fidelity F while sweeping JPA5 squeezing angle γ_5 and target state angle. The optimal JPA5 squeezing angle is chosen at $\gamma_5 = 138°$, which is denoted by the red box.

dBm and JPA2 pump power of −31 dBm, and also choose a Bell measurement gain of 21 dB, corresponding to initial JPA4 pump power of −20.45 dBm and −20.03 dBm. JPA1 and JPA4 squeezing angles are initialized at 45°, while JPA2 and JP5 squeezing angles are initialized at 135°.

JPA5 angle sweep

We balance the Bell measurement to reduce the displacement angle dependence of the teleportation protocol. In effect, we balance the electric path in length in both arms of the interferometer that forms the Josephson mixer. Ideally, the teleportation protocol should perform uniformly for all target state angles, so that we obtain a codebook symmetric in signal phase. We begin this calibration by fixing the JPA4 parameters and sweeping the JPA5 squeezing angle γ_5. Fig. 6.2 shows the measurement results for our JPA5 angle calibration. We sweep the JPA5 angle from 130° to 138° around our initial value. We cover 180° in the target state angle since the behavior is 180°-periodic. We see from Fig. 6.2(a) that the detected number of displacement photons is least dependent on target state angle at $\gamma_5 = 138°$. Moreover, we see from 6.2(b) that the teleportation fidelity is most uniform around $\gamma_5 = 138°$. Thus, we choose $\gamma_5 = 138°$ as the optimal JPA5 squeezing angle in this balancing step.

JPA5 power sweep

We continue to balance the Bell measurement, by fixing the JPA4 parameters and sweeping the JPA5 pump power P_5. Fig. 6.3 shows the measurement results for our JPA5 pump

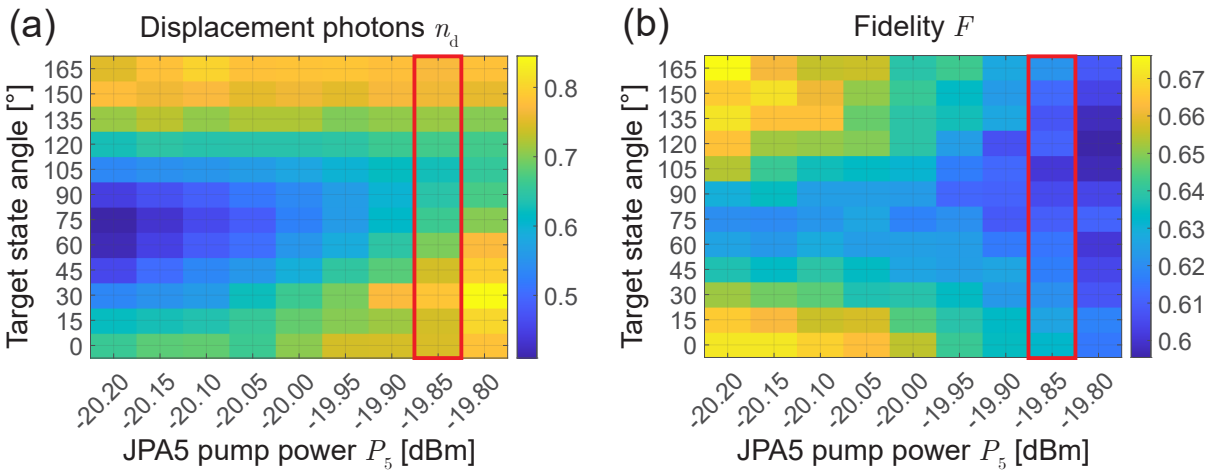

Figure 6.3: Optimization of JPA5 pump power for the quantum teleportation experiment. The input signal has a frequency of 5.55 GHz and displacement photon number of 1.1. Pump power is referred to the input port of the JPA pump. (a) Measurement of displacement photons n_d while sweeping JPA5 pump power P_5 and target state angle. (b) Measurement of fidelity F while sweeping JPA5 pump power P_5 and target state angle. The optimal JPA5 pump power is chosen at $P_5 = -19.85$ dBm, which is denoted by the red box.

power calibration. We sweep the JPA5 pump power from -20.20 to -19.80 dBm around our initial value. We see from Fig. 6.3(a) that the displacement photons is least dependent on target state angle at $P_5 = -19.85$ dBm. Moreover, we see from 6.3(b) that the teleportation fidelity is also most uniform around $P_5 = -19.85$ dBm. We note that teleportation fidelity deteriorates at higher pump powers due to increased amplification noise from the JPA. Thus, we choose $P_5 = -19.85$ dBm as the optimal JPA5 squeezing angle in this balancing step.

TMS state balancing

We then balance the TMS state to improve the interference effect of this entangled resource, and thereby optimize teleportation fidelity. Ideally, the TMS state should be balanced, so that we have perfect destructive interference of the quantum noise at Bob's directional coupler. We begin this calibration by fixing the JPA2 parameters and sweep the JPA1 squeezing angle γ_1 and pump power P_1. Fig. 6.4 shows the measurement results for our JPA1 calibration. We sweep the JPA1 squeezing angle from 15° to 55° and the JPA1 pump power from -75.7 to -74.3 dBm around our initial values. We see from Fig. 6.4 that the purity and variance ratio behave in opposing manners. Thus, we find an optimal compromise where simultaneously variance ratio is lowest and purity is highest at $\gamma_1 = 55°$ and $P_1 = -75.7\,\mathrm{dB\,m}$. This working point gives a variance ratio $\sigma_r^2 = 1.23$ and a purity $\mu = 0.389$.

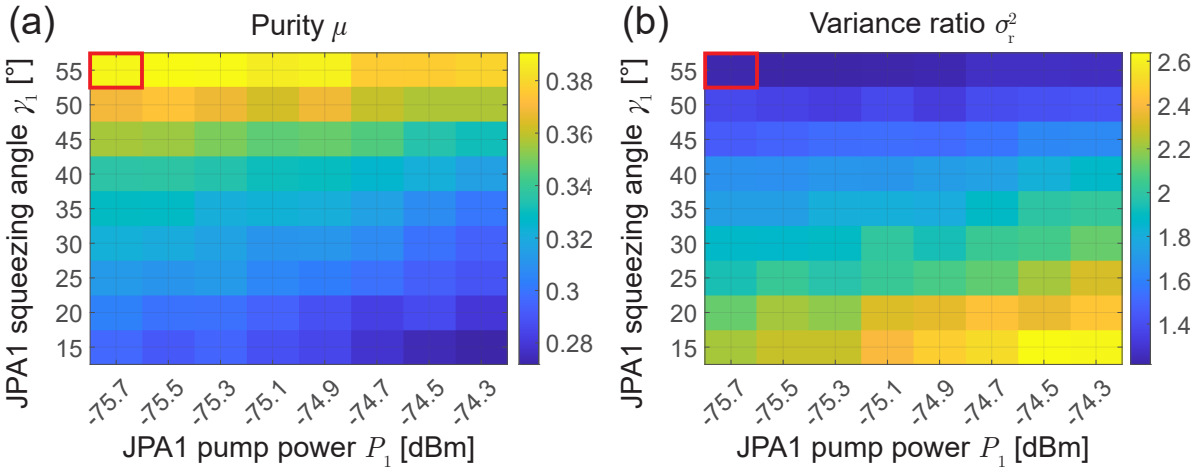

Figure 6.4: Optimization of TMS state balancing for the quantum teleportation experiment. The input signal has a frequency of 5.55 GHz and displacement photon number of 1.1. (a) Measurement of purity μ while sweeping JPA1 pump power P_1 and JPA1 squeezing angle γ_1. (b) Measurement of variance ratio σ_r^2 while sweeping JPA1 pump power P_1 and JPA1 squeezing angle γ_1. The optimal working point is chosen at $P_1 = -75.7$ dBm and $\gamma_1 = 55°$, which is denoted by the red box. This gives a variance ratio $\sigma_r^2 = 1.23$ and a purity $\mu = 0.389$.

6.1.3 Microwave quantum teleportation

After choosing the optimal working parameters, we can proceed with the quantum teleportation measurement. We run the measurement in a 8-pulse scheme using the DTG. The pulses that include only individual JPAs are used to stabilize the JPA squeezing angles. The pulse with no input signal and the pulse with only the coherent signal are used as references. The pulse that includes JPAs 1/2/4/5 and the coherent signal implements quantum teleportation. The pulse that includes only JPAs 4/5 and the coherent signal implements classical teleportation. We then compare the fidelities between the quantum teleportation and classical teleportation measurements to see if a quantum advantage is achieved.

Fig. 6.5 shows the results for our teleportation experiment. We sweep the full 360° target state angle and the target state power from −156 to −136 dBm, corresponding to displacement photon numbers from 0.07 to 7.79. We observe that fidelities are higher for small displacement photon numbers, since these states are more closely resembled by the ambient thermal noise and also the JPAs enter compression for high photon numbers. We see that classical teleportation attains higher fidelities for small displacement photon numbers, but is surpassed by quantum teleportation fidelity at around 1.11 displacement photons. In particular, quantum teleportation fidelity is on average 0.129 higher than classical teleportation fidelity at around 7.02 displacement photons. The reason that classical fidelity exceeds quantum fidelity at low displacement photon numbers is because we do not ideally match the projection condition $G\beta = 4$. Furthermore, the average

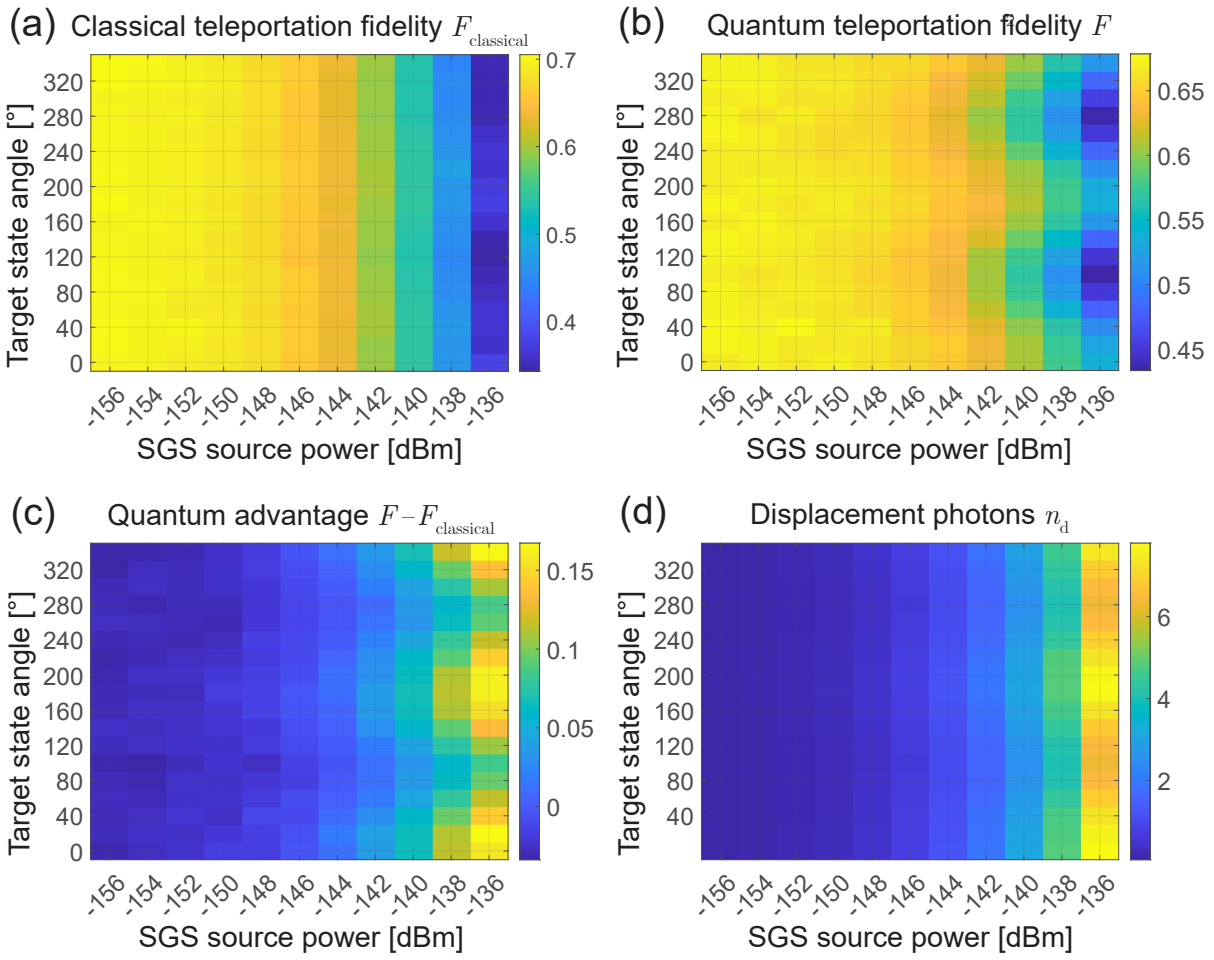

Figure 6.5: Results for a microwave quantum teleportation experiment over the cryogenic link. Input state power is referred to the input port of the JPA signal line. (a) Measurement of classical teleportation fidelity $F_{\text{classical}}$ while sweeping input state power and target state angle. (b) Measurement of quantum teleportation fidelity F while sweeping input state power and target state angle. (c) Measurement of quantum advantage $F - F_{\text{classical}}$ while sweeping input state power and target state angle. Quantum advantage is calculated here as the fidelity advantage of the quantum teleportation case over the classical teleportation case. (a) Measurement of displacement photons n_{d} while sweeping input state power and target state angle. We see that there is a quantum advantage above 1.11 displacement photons. Furthermore, the average quantum teleportation fidelity remains above 0.547 up to 4.45 displacement photons, which exceeds the asymptotic classical limit $F = 1/2$.

quantum teleportation fidelity remains above 0.547 up to 4.45 displacement photons, which exceeds the asymptotic classical limit $F = 1/2$. These results show that microwave quantum teleportation has been successfully demonstrated and indeed achieves a quantum advantage.

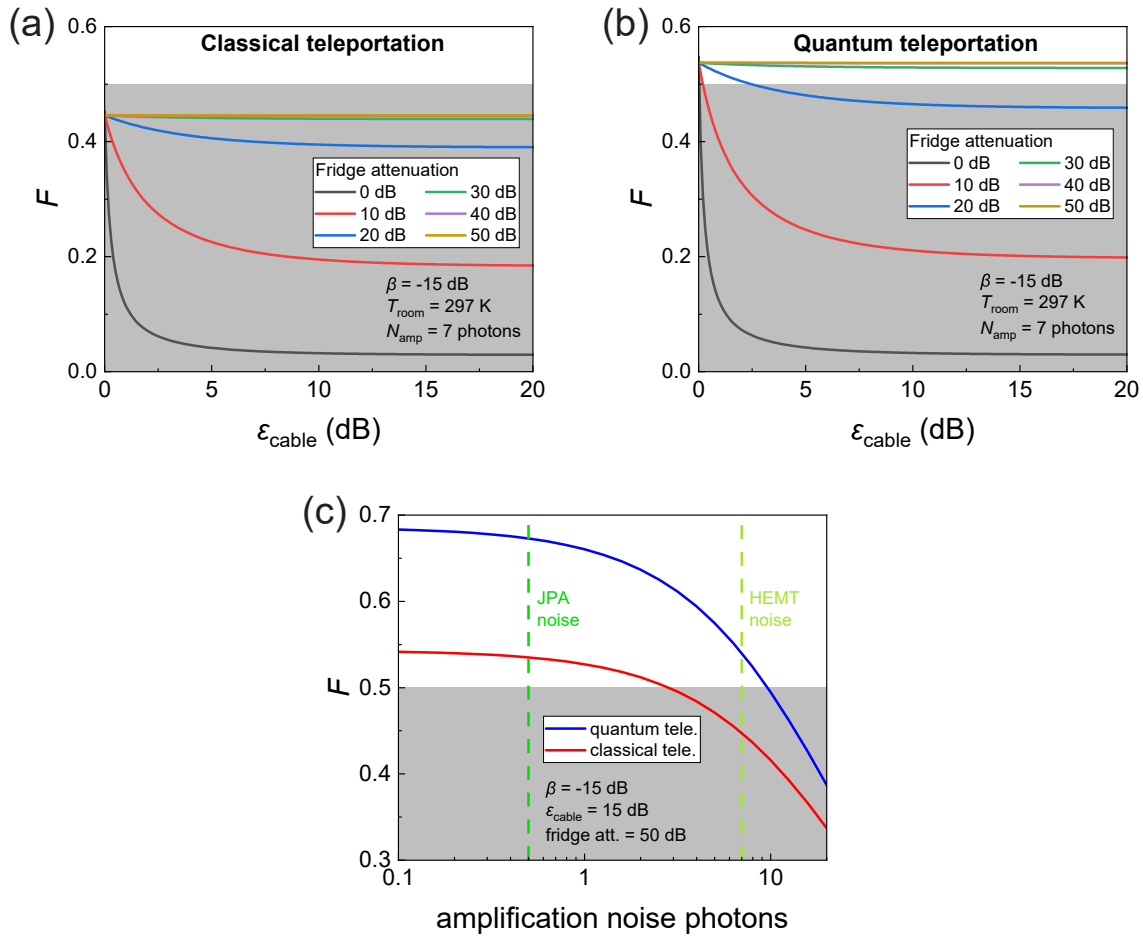

Figure 6.6: Simulation results for implementing a room temperature feedforward channel in the quantum teleportation experiment. We assume that the amplification chain fully compensates for the cable and fridge attenuations. (a) Classical teleportation fidelity for different attenuation levels in the RT cable and fridge. (b) Quantum teleportation fidelity for different attenuation levels in the RT cable and fridge. (c) Fidelity of quantum teleportation and classical teleportation depending on the amount of noise in the amplification chain before room temperature. We take JPA noise to be quantum-limited at 1/2 photons and HEMT noise to be 7 photons.

6.2 Analog quantum teleportation with room temperature feedforward

With the successful realization of quantum teleportation over the cryogenic link, we theoretically investigate quantum teleportation over a RT feedforward. We can then experimentally test our theory about teleportation over thermal channels and its function as an error-correction scheme for Gaussian imperfections, as described in Section 3.3. We simulate teleportation over a RT feedforward using the scheme in Fig. 3.2. From Fig. 6.6(a,b), we see that quantum teleportation fidelity surpasses classical teleportation

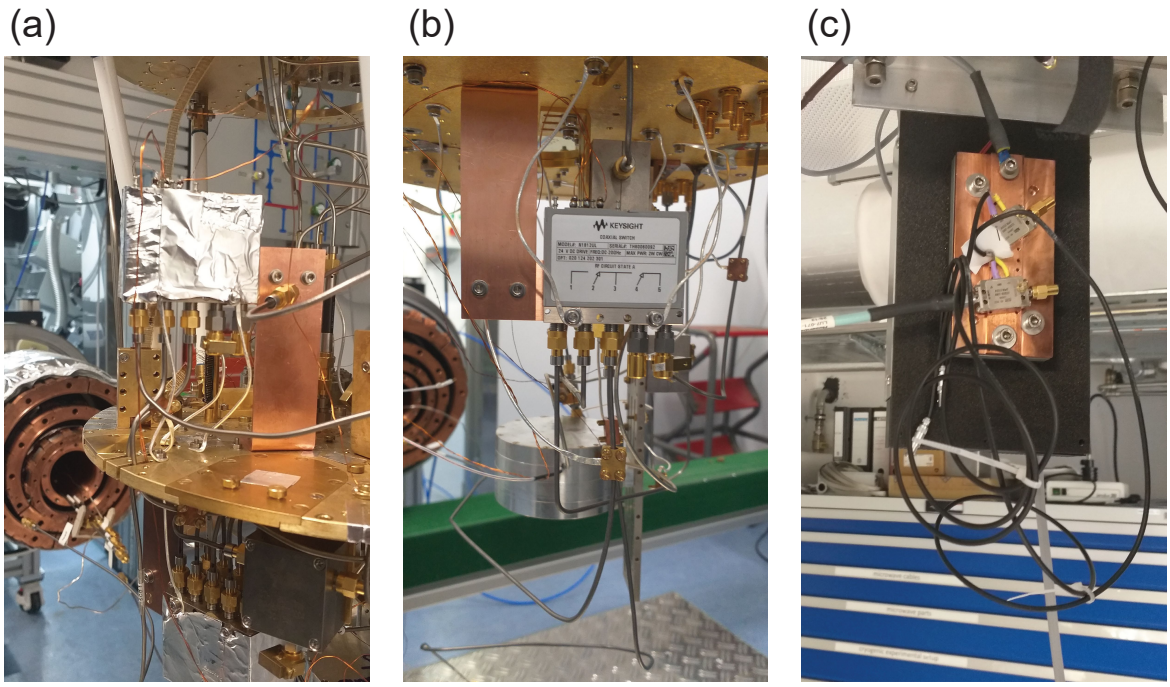

Figure 6.7: (a) Photograph of cryogenic switch in the Alice cryostat. (b) Photograph of the cryogenic switch in the Bob cryostat. (c) Photograph of the RT amplifier at Alice used to amplify the RT feedforward signal.

fidelity, and can exceed the asymptotic classical limit $F = 1/2$, given that there is sufficient attenuation of the RT signal before it enters the Bob fridge. We note that, in experiment, the RT cable attenuation is $\varepsilon_{\text{cable}} = 7$ dB and the fridge attenuation is 54 dB at 5 GHz. The large attenuation is needed to suppress the Johnson-Nyquist noise from room temperature. For the simulation, we assume that the amplification chain fully compensates for the RT cable and fridge attenuations. Furthermore, we see from Fig. 6.6(c) that teleportation fidelity is limit by the noise in the amplification chain before room temperature. In fact the HEMT is the main noise sources, because components before the HEMT have low noise, and noise sources after the HEMT becomes negligible due to the Friis equation, since the signal is greatly amplified.

We plan to implement quantum teleportation over a RT feedforward by introducing cryogenic switches at the feedforward superconducting cable. A switch is installed at the Alice sample stage and receives the feedforward signal after the Bell measurement. One output of the switch remains connected to the superconducting cables through the cryolink, while the other output would exit the Alice cryostat into a RT microwave cable (TrueBlue 090-2684, Teledyne Storm Microwave) and reenter the Bob cryostat as a room temperature input. The 11 m RT feedforward cable is made by connecting two 4 m cables and one 3 m cable, and has an attenuation of 7 dB at 5 GHz. The Bob cryostat has an attenuation of 54 dB at 5 GHz. To compensate for these losses, we need to utilize a cryogenic HEMT

(LNF-LNC4_8C) with 42 dB gain and a RT amplifier (AMT-A0033, Agile MwT) with 28 dB gain. Excessive gain can be reduced by adding attenuators in the RT cable. The RT feedforward signal then travels to the Bob sample stage through a microwave input line. Another switch is installed in the Bob sample stage, which receives the feedforward signal from either the cryolink or the room temperature path, and outputs the signal into the directional coupler. We can use this switch system to choose between operating with the cryogenic feedforward or the RT feedforward during measurement. Fig. 6.7 shows the installed switches and RT amplifier in preparation for the RT feedforward experiment. Studying microwave quantum teleportation under room temperature conditions can give us better understanding about how thermal noise affects quantum information and can have practical applications for microwave quantum communication.

Chapter 7

Conclusion and outlook

In this thesis, we analyze analog CV quantum teleportation under realistic scenarios and construct a cryogenic link to experimentally implement microwave quantum teleportation. Due to the promising advancements in quantum computers based on superconducting circuits, microwave quantum teleportation sees applications as an efficient communication protocol between superconducting quantum processors. Thus, we are motivated to realize a prototype quantum local area network in the microwave regime. In our experiments, we use Josephson parametric amplifiers to generate and manipulate propagating quantum microwaves, such as the two-mode squeezed state that serves as our entangled resource for quantum teleportation. We use our cryogenic link as a low temperature environment that connect Alice and Bob for our entanglement distribution and feedforward channels.

As our first main result, we analyze the influence of a finite-energy codebook and thermal channels on the performance of quantum teleportation. The available codebook size is limited by the 1 dB compression point of our JPAs, which affects the no-cloning threshold to guarantee unconditional security. We choose a truncated Gaussian codebook as a compromise between the Gaussian codebook with theoretically known results and truncation limit due to finite energy requirements. We are then able to derive an upper bound F_{TG} on the no-cloning threshold that is greater than the asymptotic no-cloning threshold $F = 2/3$. This result means that when considering a realistic codebook, we might require higher teleportation fidelities in order to guarantee secure communication. We then analyze the influence of ambient thermal noise in the entanglement distribution and feedforward channels. For the entanglement distribution channel, we find that any losses and noise deteriorate the interference mechanism of the quantum teleportation protocol, and thereby would reduce fidelity. However, the loss and noise term for the feedforward channel is modulated by the coupling β. This implies that losses and noise from the feedforward channel can be suppressed if we use sufficiently small coupling and correspondingly large gain, so that fidelity is not reduced. Thus, we find that quantum teleportation implements an error-correction scheme for Gaussian imperfections in the feedforward channel.

Another large part of our work is constructing the novel 6.5-meter-long microwave quantum cryogenic link. The MQCL consists of three modules, namely the Alice cryostat,

the Bob cryostat, and the cryogenic link. The Alice cryostat is a home-built dilution refrigerator at the Walther-Meißner-Institute. The Bob cryostat is a commercial Triton dilution refrigerator manufactured by Oxford Instruments. The cryolink is a custom-made connection that can maintain cryogenic temperatures between Alice and Bob, produced by Oxford instruments. We implement the entanglement distribution and feedforward channels in our quantum teleportation experiment by threading superconducting microwave cables through the cryolink and connecting them with the experiment setups at the Alice and Bob sample stages. After a full cooldown with the MQCL, we have base temperatures of ~ 35 mK at the Alice mixing chamber, ~ 20 mK at the Bob mixing chamber, and ~ 100 mK at the cryolink center. These temperatures are sufficiently low to perform experiments with propagating quantum microwaves and we successfully demonstrate entanglement distribution over the cryolink. Furthermore, we make measurements while heating the cryolink center to 1 K, and find that the quantum states transferred over the cryolink do not deteriorate due to low losses in the superconducting cable. With the successful installation of the MQCL, we move towards realizing a microwave quantum local area network.

Finally, we demonstrate analog continuous-variable quantum teleportation over the MQCL. This is the first demonstration of microwave quantum teleportation between spatially-separated cryostats. We begin by generating a TMS state from two orthogonally squeezed states with 3 dB squeezing level and distributing it between Alice and Bob through the cryolink. We then input a propagating quantum microwave state at Alice and perform a join quadrature measurement with 21 dB gain on the input state and Alice's part of the TMS state. We send the measurement result to Bob and use it to perform state displacement on Bob's part of the TMS state. This procedure then teleports the input state from Alice to Bob. In our quantum teleportation experiment, we send propagating microwave states with displacement photon numbers from 0.07 to 7.79 over the entire 360° phase angle. We measure that classical teleportation attains higher fidelities for small displacement photon numbers, but quantum advantage is achieved at around 1.11 displacement photons. In particular, quantum teleportation fidelity is on average 0.129 higher than classical teleportation fidelity at around 7.02 displacement photons. Furthermore, the average quantum teleportation fidelity remains above 0.547 up to 4.45 displacement photons, which exceeds the asymptotic classical limit $F = 1/2$. These measurement results show that we successfully demonstrate quantum advantage with microwave quantum teleportation over the MQCL.

In the next steps, we plan to include a room temperature feedforward channel in order to study quantum teleportation over thermal channels and its function as an error-correction scheme for Gaussian imperfections. This can be implemented by installing a switch that directs the feedforward signal from the superconducting cable in the cryolink to a microwave cable at room temperature. Due to additional attenuation from the room temperature cable and the Bob cryostat input line, we need to compensate by increasing

amplification with a cryogenic HEMT and a RT amplifier. Realizing quantum teleportation over a room temperature feedforward would be technologically useful and provide better understanding about where the microwave signal transitions from quantum to classical.

As an outlook, we can envision a quantum local area network with propagating microwaves, where quantum information is communicated using quantum teleportation schemes between nodes connected by cryogenic links. We can consider realizing quantum gate teleportation between spatially-separated superconducting quantum processors. We can also consider implementing an open-air feedforward channel by using microwave antennas.

Bibliography

[1] M. H. Devoret and R. J. Schoelkopf, "Superconducting Circuits for Quantum Information: An Outlook", Science **339**, 1169 (2013).

[2] N. Gisin and R. Thew, "Quantum communication", Nature Photonics **1**, 165 (2007).

[3] L. Steffen, Y. Salathe, M. Oppliger, P. Kurpiers, M. Baur, C. Lang, C. Eichler, G. Puebla-Hellmann, A. Fedorov, and A. Wallraff, "Deterministic quantum teleportation with feed-forward in a solid state system", Nature **500**, 319 (2013).

[4] S. Pirandola, B. R. Bardhan, T. Gehring, C. Weedbrook, and S. Lloyd, "Advances in photonic quantum sensing", Nature Photonics **12**, 724 (2018).

[5] S. Lloyd, "Enhanced Sensitivity of Photodetection via Quantum Illumination", Science **321**, 1463 (2008).

[6] C. Gross and I. Bloch, "Quantum simulations with ultracold atoms in optical lattices", Science **357**, 995 (2017).

[7] R. J. Schoelkopf and S. M. Girvin, "Wiring up quantum systems", Nature **451**, 664 (2008).

[8] A. Wallraff, D. I. Schuster, A. Blais, L. Frunzio, R.-. S. Huang, J. Majer, S. Kumar, S. M. Girvin, and R. J. Schoelkopf, "Strong coupling of a single photon to a superconducting qubit using circuit quantum electrodynamics", Nature **431**, 162 (2004).

[9] T. Niemczyk, F. Deppe, H. Huebl, E. P. Menzel, F. Hocke, M. J. Schwarz, J. J. Garcia-Ripoll, D. Zueco, T. Hümmer, E. Solano, A. Marx, and R. Gross, "Circuit quantum electrodynamics in the ultrastrong-coupling regime", Nature Physics **6**, 772 (2010).

[10] F. Arute *et al.*, "Quantum supremacy using a programmable superconducting processor", Nature **574**, 505 (2019).

[11] C. Weedbrook, S. Pirandola, R. García-Patrón, N. J. Cerf, T. C. Ralph, J. H. Shapiro, and S. Lloyd, "Gaussian quantum information", Rev. Mod. Phys. **84**, 621 (2012).

[12] S. L. Braunstein and P. van Loock, "Quantum information with continuous variables", Rev. Mod. Phys. **77**, 513 (2005).

[13] M. Mirhosseini, A. Sipahigil, M. Kalaee, and O. Painter, "Superconducting qubit to optical photon transduction", Nature **588**, 599 (2020).

[14] K. G. Fedorov, M. Renger, S. Pogorzalek, R. D. Candia, Q. Chen, Y. Nojiri, K. Inomata, Y. Nakamura, M. Partanen, A. Marx, R. Gross, and F. Deppe, "Experimental quantum teleportation of propagating microwaves", Science Advances **7**, eabk0891 (2021).

[15] B. Yurke, P. G. Kaminsky, R. E. Miller, E. A. Whittaker, A. D. Smith, A. H. Silver, and R. W. Simon, "Observation of 4.2-K equilibrium-noise squeezing via a Josephson-parametric amplifier", Phys. Rev. Lett. **60**, 764 (1988).

[16] B. Yurke, L. R. Corruccini, P. G. Kaminsky, L. W. Rupp, A. D. Smith, A. H. Silver, R. W. Simon, and E. A. Whittaker, "Observation of parametric amplification and deamplification in a Josephson parametric amplifier", Phys. Rev. A **39**, 2519 (1989).

[17] R. Movshovich, B. Yurke, P. G. Kaminsky, A. D. Smith, A. H. Silver, R. W. Simon, and M. V. Schneider, "Observation of zero-point noise squeezing via a Josephson-parametric amplifier", Phys. Rev. Lett. **65**, 1419 (1990).

[18] D. M. Pozar, *Microwave Engineering* (Wiley, Hoboken, 2012).

[19] D. F. Walls and G. J. Milburn, *Quantum Optics* (Springer, Berlin, Heidelberg, 2008).

[20] M. O. Scully and M. S. Zubairy, *Quantum Optics* (Cambridge University Press, 1997).

[21] E. Wigner, "On the Quantum Correction For Thermodynamic Equilibrium", Phys. Rev. **40**, 749 (1932).

[22] M. Hillery, R. O'Connell, M. Scully, and E. Wigner, "Distribution functions in physics: Fundamentals", Physics Reports **106**, 121 (1984).

[23] A. Wunsche, "Reconstruction of operators from their normally ordered moments for a single boson mode", Quantum Optics: Journal of the European Optical Society Part B **2**, 453 (1990).

[24] V. Bužek, G. Adam, and G. Drobný, "Quantum state reconstruction and detection of quantum coherences on different observation levels", Phys. Rev. A **54**, 804 (1996).

[25] V. Bužek, G. Adam, and G. Drobný, "Reconstruction of Wigner Functions on Different Observation Levels", Annals of Physics **245**, 37 (1996).

[26] A. Serafini, F. Illuminati, and S. D. Siena, "Symplectic invariants, entropic measures and correlations of Gaussian states", Journal of Physics B: Atomic, Molecular and Optical Physics **37**, L21 (2003).

[27] G. Adesso, A. Serafini, and F. Illuminati, "Determination of Continuous Variable Entanglement by Purity Measurements", Phys. Rev. Lett. **92**, 087901 (2004).

[28] G. Adesso and F. Illuminati, "Gaussian measures of entanglement versus negativities: Ordering of two-mode Gaussian states", Phys. Rev. A **72**, 032334 (2005).

[29] H. Nyquist, "Thermal Agitation of Electric Charge in Conductors", Phys. Rev. **32**, 110 (1928).

[30] K. G. Fedorov, L. Zhong, S. Pogorzalek, P. Eder, M. Fischer, J. Goetz, E. Xie, F. Wulschner, K. Inomata, T. Yamamoto, Y. Nakamura, R. Di Candia, U. Las Heras, M. Sanz, E. Solano, E. P. Menzel, F. Deppe, A. Marx, and R. Gross, "Displacement of Propagating Squeezed Microwave States", Phys. Rev. Lett. **117**, 020502 (2016).

[31] M. G. Paris, "Displacement operator by beam splitter", Physics Letters A **217**, 78 (1996).

[32] A. Furusawa, J. L. Sørensen, S. L. Braunstein, C. A. Fuchs, H. J. Kimble, and E. S. Polzik, "Unconditional Quantum Teleportation", Science **282**, 706 (1998).

[33] S.-H. Tan, B. Erkmen, V. Giovannetti, S. Guha, S. Lloyd, L. Maccone, S. Pirandola, and J. Shapiro, "Quantum Illumination with Gaussian States", Physical Review Letters **101**, 253601 (2008).

[34] U. L. Heras, R. D. Candia, K. G. Fedorov, F. Deppe, M. Sanz, and E. Solano, "Quantum illumination reveals phase-shift inducing cloaking", Scientific Reports **7** (2017).

[35] R. F. Werner, "Quantum states with Einstein-Podolsky-Rosen correlations admitting a hidden-variable model", Phys. Rev. A **40**, 4277 (1989).

[36] A. Peres, "Separability Criterion for Density Matrices", Phys. Rev. Lett. **77**, 1413 (1996).

[37] R. Simon, "Peres-Horodecki Separability Criterion for Continuous Variable Systems", Phys. Rev. Lett. **84**, 2726 (2000).

[38] A. Serafini, F. Illuminati, M. G. A. Paris, and S. De Siena, "Entanglement and purity of two-mode Gaussian states in noisy channels", Phys. Rev. A **69**, 022318 (2004).

[39] E. A. Tholén, A. Ergül, E. M. Doherty, F. M. Weber, F. Grégis, and D. B. Haviland, "Nonlinearities and parametric amplification in superconducting coplanar waveguide resonators", Applied Physics Letters **90**, 253509 (2007).

[40] B. Abdo, O. Suchoi, E. Segev, O. Shtempluck, M. Blencowe, and E. Buks, "Intermodulation and parametric amplification in a superconducting stripline resonator integrated with a dc-SQUID", EPL (Europhysics Letters) **85**, 68001 (2009).

[41] T. Yamamoto, K. Inomata, M. Watanabe, K. Matsuba, T. Miyazaki, W. D. Oliver, Y. Nakamura, and J. S. Tsai, "Flux-driven Josephson parametric amplifier", Applied Physics Letters **93**, 042510 (2008).

[42] B. Josephson, "Possible new effects in superconductive tunnelling", Physics Letters **1**, 251 (1962).

[43] R. Gross and A. Marx, *Festkörperphysik* (Oldenbourg Verlag, München, 2012).

[44] M. Tinkham, *Introduction to Superconductivity* (McGraw-Hill Inc., New York, 1996).

[45] M. Sandberg, C. M. Wilson, F. Persson, T. Bauch, G. Johansson, V. Shumeiko, T. Duty, and P. Delsing, "Tuning the field in a microwave resonator faster than the photon lifetime", Applied Physics Letters **92**, 203501 (2008).

[46] T. Yamamoto, K. Koshino, and Y. Nakamura, "Parametric Amplifier and Oscillator Based on Josephson Junction Circuitry", in *Principles and Methods of Quantum Information Technologies*, edited by Y. Yamamoto and K. Semba (Springer Japan, Tokyo, 2016), pp. 495–513.

[47] C. M. Caves, "Quantum limits on noise in linear amplifiers", Phys. Rev. D **26**, 1817 (1982).

[48] C. H. Bennett, G. Brassard, C. Crépeau, R. Jozsa, A. Peres, and W. K. Wootters, "Teleporting an unknown quantum state via dual classical and Einstein-Podolsky-Rosen channels", Phys. Rev. Lett. **70**, 1895 (1993).

[49] R. Di Candia, K. G. Fedorov, L. Zhong, S. Felicetti, E. P. Menzel, M. Sanz, F. Deppe, A. Marx, R. Gross, and E. Solano, "Quantum teleportation of propagating quantum microwaves", EPJ Quantum Technology **2**, 25 (2015).

[50] D. Bouwmeester, J.-W. Pan, K. Mattle, M. Eibl, H. Weinfurter, and A. Zeilinger, "Experimental quantum teleportation", Nature **390**, 575 (1997).

[51] S. Pirandola, C. Ottaviani, G. Spedalieri, C. Weedbrook, S. L. Braunstein, S. Lloyd, T. Gehring, C. S. Jacobsen, and U. L. Andersen, "High-rate measurement-device-independent quantum cryptography", Nature Photonics **9**, 397 (2015).

[52] F. Fesquet, F. Kronowetter, M. Renger, Q. Chen, K. Honasoge, O. Gargiulo, Y. Nojiri, A. Marx, F. Deppe, R. Gross, and K. G. Fedorov, "Perspectives of microwave quantum key distribution in open-air", arXiv (2022).

[53] M. Sanz, K. G. Fedorov, F. Deppe, and E. Solano, "Challenges in Open-air Microwave Quantum Communication and Sensing", in *2018 IEEE Conference on Antenna Measurements Applications (CAMA)* (2018), pp. 1–4.

[54] S. Pirandola, J. Eisert, C. Weedbrook, A. Furusawa, and S. L. Braunstein, "Advances in quantum teleportation", Nature Photonics **9**, 641 (2015).

[55] S. L. Braunstein, C. A. Fuchs, and H. J. Kimble, "Criteria for continuous-variable quantum teleportation", Journal of Modern Optics **47**, 267 (2000).

[56] F. Grosshans and P. Grangier, "Quantum cloning and teleportation criteria for continuous quantum variables", Phys. Rev. A **64**, 010301 (2001).

[57] F. Grosshans and P. Grangier, "Continuous Variable Quantum Cryptography Using Coherent States", Phys. Rev. Lett. **88**, 057902 (2002).

[58] S. L. Braunstein, N. J. Cerf, S. Iblisdir, P. van Loock, and S. Massar, "Optimal Cloning of Coherent States with a Linear Amplifier and Beam Splitters", Phys. Rev. Lett. **86**, 4938 (2001).

[59] P. T. Cochrane, T. C. Ralph, and A. Dolińska, "Optimal cloning for finite distributions of coherent states", Phys. Rev. A **69**, 042313 (2004).

[60] N. J. Cerf, O. Krüger, P. Navez, R. F. Werner, and M. M. Wolf, "Non-Gaussian Cloning of Quantum Coherent States is Optimal", Phys. Rev. Lett. **95**, 070501 (2005).

[61] M. Renger, S. Pogorzalek, Q. Chen, Y. Nojiri, K. Inomata, Y. Nakamura, M. Partanen, A. Marx, R. Gross, F. Deppe, and K. G. Fedorov, "Beyond the standard quantum limit for parametric amplification of broadband signals", npj Quantum Information **7**, 160 (2021).

[62] S. Pogorzalek, "Remote State Preparation of Squeezed Microwave States", Ph.D. thesis, Technishce Universität München (2020).

[63] F. Pobell, *Matter and Methods at Low Temperatures* (Springer, Berlin, Heidelberg, 2007).

[64] A. Narla, S. Shankar, M. Hatridge, Z. Leghtas, K. M. Sliwa, E. Zalys-Geller, S. O. Mundhada, W. Pfaff, L. Frunzio, R. J. Schoelkopf, and M. H. Devoret, "Robust Concurrent Remote Entanglement Between Two Superconducting Qubits", Phys. Rev. X **6**, 031036 (2016).

[65] K. Inomata, Z. Lin, K. Koshino, W. D. Oliver, J.-S. Tsai, T. Yamamoto, and Y. Nakamura, "Single microwave-photon detector using an artificial Î-type three-level system", Nature Communications **7** (2016).

[66] U. Leonhardt, "Measuring the Quantum State of Light", American Journal of Physics **66**, 550 (1998).

[67] M. Mariantoni, E. P. Menzel, F. Deppe, M. A. Araque Caballero, A. Baust, T. Niemczyk, E. Hoffmann, E. Solano, A. Marx, and R. Gross, "Planck Spectroscopy and Quantum Noise of Microwave Beam Splitters", Phys. Rev. Lett. **105**, 133601 (2010).

[68] E. P. Menzel, "Propagating quantum microwaves: dual-path state reconstruction and path entanglement", Ph.D. thesis, Technishce Universität München (2013).

[69] E. P. Menzel, R. Di Candia, F. Deppe, P. Eder, L. Zhong, M. Ihmig, M. Haeberlein, A. Baust, E. Hoffmann, D. Ballester, K. Inomata, T. Yamamoto, Y. Nakamura, E. Solano, A. Marx, and R. Gross, "Path Entanglement of Continuous-Variable Quantum Microwaves", Phys. Rev. Lett. **109**, 250502 (2012).

[70] C. Eichler, Y. Salathe, J. Mlynek, S. Schmidt, and A. Wallraff, "Quantum-Limited Amplification and Entanglement in Coupled Nonlinear Resonators", Phys. Rev. Lett. **113**, 110502 (2014).

[71] L. Zhong, E. P. Menzel, R. D. Candia, P. Eder, M. Ihmig, A. Baust, M. Haeberlein, E. Hoffmann, K. Inomata, T. Yamamoto, Y. Nakamura, E. Solano, F. Deppe, A. Marx, and R. Gross, "Squeezing with a flux-driven Josephson parametric amplifier", New Journal of Physics **15**, 125013 (2013).

[72] A. Marx, J. Hoess, and K. Uhlig, "Dry Dilution Refrigerator for Experiments on Quantum Effects in the Microwave Regime", arXiv (2014).

[73] *Pulse Tube Cryocoolers*, Cryomech Inc. (2022).

[74] *Annual Report 2021*, Walther-Meißner-Institute (2021).

[75] *Triton*, Oxford Instruments (2018).

Acknowledgements

This thesis would not have been possible without the support, guidance, and assistance of many people whom I would like to thank in the following:

Prof. Dr. Rudolf Gross for giving me the opportunity to complete my master's thesis at the Walther-Meißner-Institute.

Dr. Kirill G. Fedorov for offering me this thesis topic and for introducing me to the field of propagating quantum microwaves. I especially want to thank you for your dedication in advising me throughout the thesis and teaching me the necessary skills of doing science.

Michael Renger for giving me day-to-day guidance during my thesis, including everything from basic lab techniques to writing down results scientifically. I especially want to thank you for your kindness and encouragement in our two years of working together.

Simon Gandorfer for sharing half of the thesis and for your friendliness as we work on building the experiments.

Dr. Achim Marx for your great help and experience when we reach hurdles while constructing the cryolink.

Dr. Robert Di Candia for your ideas and discussions about finite-energy codebooks.

The PhD students *Florian Fesquet*, *Kedar Honasoge*, *Fabian Kronowetter*, *Yuki Nojiri*, and *Daniil Bazulin* for your expert suggestions and for your assistance when we need extra hands in the lab.

My office colleagues *Alexander Jung*, *Lukas Niekamp*, *Michał Cherczyński*, *Tammo Sievers*, *Philipp Krüger* and *Yuhao Sun* for the general good vibes.

The WMI workshop for delivering the many custom-made cryolink components.

All members of WMI for creating a good working atmosphere.

My girlfriend *Hongmei Xia* for your emotional support and the time we had together.

My parents for your unconditional love and support, and for giving me the opportunity to pursue further studies. Thank you for everything!